NASA Technical Paper 2399

AVSCOM Technical Report 84-A-3

1984

Application of the ONERA Model of Dynamic Stall

K. W. McAlister
Aeromechanics Laboratory
USAAVSCOM Research and Technology Laboratories
Ames Research Center
Moffett Field, California

O. Lambert
Service Technique des Programmes Aeronautiques
Paris Armees, France

D. Petot
Office National D'Etudes et
de Recherches Aerospatiales
Châtillon, France

NASA
National Aeronautics
and Space Administration

Scientific and Technical Information Branch

TABLE OF CONTENTS

SYMBOLS

A_n load measurements in air, $n = 1, 2, 3$

a model coefficient to be determined empirically, $a = a(\alpha)$

C_d drag coefficient

C_l lift coefficient

C_m quarter-chord pitching-moment coefficient

c airfoil chord, m

e model coefficient to be determined empirically, $e = e(\alpha)$

F aerodynamic load coefficient, $F = F(\tau)$

F_1 component of F sufficient for linear range, $F_1 = F_1(\tau)$

F_2 supplement to F_1 required for nonlinear range, $F_2 = F_2(\tau)$

F_l linear extrapolation of the static load curve, $F_l = F_l(\alpha)$

F_s static load, $F_s = F_s(\alpha)$

$\bar{F}$ mean value in Taylor expansion for load, $\bar{F} = \bar{F}(\tau)$

$\tilde{F}$ modulus of first harmonic in Taylor expansion for load, $\tilde{F} = \tilde{F}(\tau)$

f_1 forcing function on F_1 defined by second member in equation (2)

f_2 forcing function on F_2 defined by second member in equation (3)

k reduced frequency of oscillation, $k = \omega c/2U_\infty$

Re Reynolds number, $U_\infty c/\nu$

r model coefficient to be determined empirically, $r = r(\alpha)$

s model coefficient to be determined empirically, $s = s(\alpha)$

t time, sec

U_∞ free-stream velocity, m/sec

W_n load measurements in water, $n = 1, 2, 3$

α airfoil incidence, deg

α_0 mean value of pitch oscillation, deg

α_1 amplitude of pitch oscillation, deg

Δ difference between linear and static load curves, $F_l - F_s$

ϵ unity-step function

λ model coefficient to be determined empirically, $\lambda = \lambda(\alpha)$

ν kinematic viscosity, m^2/sec

ξ_{mn} coefficients in mth cubic spline equation, $n = 1, 2, 3$

ρ density, kg/m^3

σ model coefficient to be determined empirically, $\sigma = \sigma(\alpha)$

τ reduced time, $\tau = \omega t/k$

ω frequency of oscillation in pitch, rad/sec

$(\dot{})$ derivative with respect to time, $\partial/\partial t$

$(\ddot{})$ second derivative with respect to time, $\partial^2/\partial t^2$

$\mathfrak{I}$ imaginary part of quantity

$\aleph$ total number of increments in one cycle

$\Re$ real part of quantity

APPLICATION OF THE ONERA MODEL OF DYNAMIC STALL

K. W. McAlister, O. Lambert,* and D. Petot†

Aeromechanics Laboratory, U.S. Army Research and Technology Laboratories, AVSCOM

SUMMARY

A semiempirical model, developed at the Office National D'Etudes et de Recherches Aerospatiales (ONERA), to predict the unsteady loads on an airfoil that is experiencing dynamic stall, is investigated. This study describes the math model from an engineering point of view, demonstrates the procedure for obtaining various empirical parameters, and compares the loads predicted by the model with those obtained in the experiment. The procedure is found to be straightforward, and the final calculations are observed to be in qualitative agreement with the experimental results. Comparisons between calculations and measurements also indicate that a decrease in accuracy results when the values of both the reduced frequency and the amplitude of oscillation are large. Potential quantitative improvements in the accuracy of the calculations are discussed in terms of accounting for both the hysteresis in the static data and the effects of stall delay in the governing equations.

INTRODUCTION

When a helicopter is in forward flight, the rotor blade must undergo a cyclic variation in incidence in order to balance the lift developed both over the advancing and retreating quadrants (to prevent roll), as well as over the forward and rearward quadrants (to prevent pitch). Increasing the flight speed of the helicopter increases the asymmetry in the local velocity distribution between the advancing and retreating sides. In order to eliminate the roll moment produced by this asymmetry, the incidence of the rotor blade must be decreased on the advancing side and increased on the retreating side. Clearly there is a limit to how much the incidence can be increased without causing the flow to separate from the blade. Nevertheless, conditions often exist when this separation boundary is briefly penetrated, giving rise to a phenomenon called dynamic stall.

The characteristics of dynamic stall are strongly influenced by the time-dependent nature of the viscous region surrounding the airfoil. Although flow reversal may have progressed over most of the upper surface of the airfoil during a rapid increase in incidence, the boundary layer will normally remain attached for angles of incidence well beyond the stall angle observed in a steady flow environment (refs. 1 and 2). The onset of stall is initiated by the growth and passage of a vortex over the airfoil. By the time the vortex has reached the trailing edge, the resulting unsteady flow values for the lift, drag, and pitching moment on the airfoil may have doubled their maximum steady flow values (ref. 3). As the vortex is swept into the wake of the airfoil, a sudden reversal in the lift and drag loads occurs, thereby creating a significant source of vibration on the helicopter. Another damaging aspect of dynamic stall is the rapid growth and decline of a nose-down pitching moment. This results from a rearward movement of the center of pressure which accompanies the passage of the vortex over the airfoil and into the wake. This impulsive character of the pitching moment acts as a strong forcing function on the aeroelastic stability of the rotor blade (ref. 4). A potentially dangerous situation may therefore develop if the interaction between the blade and the surrounding air results in oscillations that are negatively damped. Since rotor blades are typically both slender and flexible, this unstable condition, known as "stall flutter," can be especially threatening to the safety of the helicopter.

In order to calculate the performance boundaries of a potential rotor design, it is essential that the mathematical formulation adequately models the effects of dynamic stall. Unfortunately, a closed-form solution does not exist. In fact, all of the currently available methods employ some form of approximation or empiricism, and are also normally restricted to two-dimensional flows (ref. 5). Many of these prediction techniques are based directly on a recognition of the global attributes contained in the unsteady force and moment responses that are observed in the angle-of-attack domain. As a consequence, expressions have been devised by numerous investigators that describe explicitly the "time-delay" character of the various events embodying dynamic stall. A particularly noteworthy representative of this approach is presented in reference 6. Two time constants are featured in this model; one describes the time delay after

*Ingenieur de l'Armement, Service Technique des Programmes Aeronautiques, Paris Armees, France.

†Resistance des Structures, Office National D'Etudes et de Recherches Aerospatiales, Chatillon, France.

exceeding the static stall angle and before a vortex is shed from the leading edge of the airfoil, and the other describes the time required for this vortex to reach the trailing edge.

Generally speaking, most prediction techniques for dynamic stall have been successful only within the limits of the data from which they were fabricated. A model that is very much dependent on its data base is described in reference 7. However, a fairly extensive range of data was considered initially, and allowance was made for expansion. This method is based on a set of algebraic equations containing parameters that must be determined from the available synthesized experimental data. Published results show that the procedure accurately reconstructs the aerodynamic loads that occur during dynamic stall over a wide range of conditions. An important factor contributing to the success of this method lies in the particular set of dynamic parameters that were postulated. The accuracy of this approach is dependent on the correctness of three semi-empirical expressions that describe (a) the airfoil incidence when moment stall occurs, (b) the dimensionless time when the stall vortex reaches the trailing edge, and (c) the incidence when the flow reattaches to the surface of the airfoil.

In contrast to the methods that attempt to duplicate the effects of dynamic stall, a unique method was developed at ONERA that utilizes the characteristics of differential equations to directly simulate the aerodynamic responses in the time domain (ref. 8). Although other techniques may render more accurate predictions of rotor blade loading, the primary advantage of the ONERA model is that the governing system of equations can be readily linearized, therefore making it well suited for inclusion in analyses of rotor stability (refs. 9 and 10). Certain aspects of the model are continuing to undergo refinement; however, the fundamental concept appears to be well established (refs. 11 and 12), and will not be restated in detail here. Instead, the scope of this presentation will be to describe the model from an engineering point of view, to demonstrate the attainment of various empirical parameters, and to compare the loads predicted by the model with those obtained from an experiment.

DESCRIPTION OF THE MATH MODEL

General Equations

A fundamental assumption is made that the aerodynamic loads can be determined from a set of nonlinear transfer functions containing input variables that describe the motion of the airfoil. Considering the operational and structural environments that are typical for helicopter rotor blades, it is further assumed that all input and output variables are first-order small quantities and that the coupling can be neglected between the chord force and either the normal force or the pitching moment. Perhaps the most restrictive assumption to be imposed, in light of the model's applicability to separated flows, is that the instantaneous force and moment loads do not depart too greatly from their steady flow values. This condition is necessary so that the coefficients appearing in the governing equations reduce to functions of only velocity and angle of attack for a given airfoil. Additional simplifying assumptions are then made concerning a reduction in the order of the equations and the elimination of certain cross coupling coefficients. The validity of these assumptions could not be demonstrated analytically, and had to be confirmed by experiment. A significant outcome from this simplification is that the model can now be used to evaluate any given load, independent of the others.

Evaluating the model at different amplitudes and frequencies provided the necessary guidance in reaching the final form of the equations. Airfoil oscillations below stall indicated that the loads could be represented by a first-order equation, having a real negative pole; whereas oscillations beyond stall produced loads that required a second-order equation representation, having two complex conjugate poles. In view of these observations, the single-equation formulation for each load was abandoned. Instead, each load would be divided into two components, one governed by the first-order equation and the other by the second-order equation. Letting the function F denote the total aerodynamic load of interest, the governing equations become

$$F = F_1 + F_2 \tag{1}$$

$$\dot{F}_1 + \lambda F_1 = \lambda F_l + (\lambda s + \sigma)\dot{\alpha} + s\ddot{\alpha} \tag{2}$$

$$\ddot{F}_2 + a\dot{F}_2 + rF_2 = -(r\Delta + e\,\dot{\Delta}) \tag{3}$$

where the coefficients λ, s, σ, a, r, and e will be treated as functions of α only, the instantaneous incidence of the airfoil. Strictly speaking, these coefficients are also dependent on the free-stream velocity (or alternatively on the Mach number) and the profile of the airfoil. However, to illustrate the application of this technique, it is sufficient to consider an incompressible flow so that α becomes the only parameter. Since these coefficients actually represent time derivatives (no longer explicitly apparent), and must be determined experimentally, they can be obtained by performing small-amplitude oscillations around discrete values of α. The range of angles over which the coefficients must be specified is dictated by the large-amplitude cases to be calculated by the model. The variables F_l and Δ, also functions of α, are completely determined by the static behavior of the airfoil. F_l denotes a linear extrapolation of the static load curve and Δ is defined to be the difference between this extrapolation and the actual static curve. Using a hypothetical lift response as an example, the relation between various terms is illustrated in figure 1.

As the frequency of the airfoil oscillation diminishes in the limit, all time derivatives vanish and equations (1)-(3) reduce to

$$\lim_{\tau \to 0} F = F_l - \Delta = F_s$$

where F_s is the static load response. If the airfoil motion is unsteady, but remains entirely within the linear range, then $\Delta = 0$ and the load is completely determined by the solution of equation (2) for F_1.

Small-Amplitude Equations

To determine the relationships between the six coefficients and α, an experiment is required in which the airfoil is made to undergo pitching oscillations at different frequencies and mean angles, and for values above and below stall. Although the pitching motion can be random (ref. 11), only harmonic variations in incidence will be considered. Letting α_0 denote the mean angle, α_1 the amplitude, and k the reduced frequency of oscillation, the incidence can be generally expressed as

$$\alpha = \alpha_0 + \Re[\alpha_1 e^{ik\tau}] \tag{4}$$

and is not restricted to small-amplitude motion. However, if the amplitude of the oscillation is small, say $\alpha_1 < 1^\circ$, then the corresponding load can be approximated by

$$F = \bar{F} + \Re[\tilde{F} e^{ik\tau}] \tag{5}$$

where $\bar{F}$ represents the mean value of the load, not necessarily equal to F_s, and $\tilde{F}$ is a complex function representing the modulus of the first harmonic of the load. This is only an approximate expression for the load since the forcing function in equation (3), and the coefficients in both equations (2) and (3), are nonlinear functions of α. As such, equation (5) is more correctly written with higher order terms; however, experiments have shown that when the amplitude of the oscillation is sufficiently small, the load response is nearly elliptical so that the first-harmonic representation is acceptable.

Given the experimental observation that for small-amplitude oscillations a first-order input in α produces a first-order output in F, the governing equations (1)-(3) can be simplified to a system with locally constant coefficients and with forcing functions that are first-order harmonic relative to α. The forcing function in equation (2) already has a first-harmonic form since it is linear in α and its derivatives. The same is not generally true of the forcing function in equation (3) since the term Δ is normally quite nonlinear with α. However, given the restriction that the oscillations will be small in amplitude means that a piecewise-linear variation with α can be ascribed. In this case, the function $\Delta(\alpha)$ can be written as

$$\Delta|_\alpha = \Delta|_{\alpha_0} + (\alpha - \alpha_0) \left.\frac{d\Delta}{d\alpha}\right|_{\alpha_0} \tag{6}$$

Although the variation of F_l with α is simply a straight line, regardless of the amplitude of oscillation, it will nevertheless be expressed in the same form as for Δ; so that

$$F_l|_\alpha = F_l|_{\alpha_0} + (\alpha - \alpha_0) \left.\frac{dF_l}{d\alpha}\right|_{\alpha_0} \tag{7}$$

Reclaiming the imaginary parts of α and F in equations (4) and (5) above, the dependent and independent variables become

$$\alpha = \alpha_0 + \alpha_1 e^{ik\tau} \tag{8}$$

$$F_1 = \bar{F}_1 + \tilde{F}_1 e^{ik\tau} \tag{9}$$

$$F_2 = \bar{F}_2 + \tilde{F}_2 e^{ik\tau} \tag{10}$$

Substituting the quantities given in equations (6)-(10) into the governing equations (1)-(3) yields

$$F = \bar{F}_1 + \bar{F}_2 + (\tilde{F}_1 + \tilde{F}_2)e^{ik\tau} \tag{11}$$

$$\lambda\bar{F}_1 + (\lambda + ik)\tilde{F}_1 e^{ik\tau} = \lambda F_l|_{\alpha_0} + \left[\left.\lambda \frac{dF_l}{d\alpha}\right|_{\alpha_0} + ik(\lambda s + \sigma) - sk^2 \right] \alpha_1 e^{ik\tau} \tag{12}$$

$$r\bar{F}_2 + (r + iak - k^2)\tilde{F}_2 e^{ik\tau} = -r\,\Delta|_{\alpha_0} - (r + iek)\alpha_1 e^{ik\tau} \left.\frac{d\Delta}{d\alpha}\right|_{\alpha_0} \tag{13}$$

Equations (12) and (13) both state that two equalities must be satisfied; the terms of one equality are steady while those of the other are unsteady (identified by their product with the complex potential term). The equalities that are composed of steady terms are:

$$\bar{F}_1 = F_l|_{\alpha_0}$$

and

$$\bar{F}_2 = -\Delta|_{\alpha_0}$$

Summing the above two expressions to obtain the mean value for the load gives

$$\bar{F} = F_l|_{\alpha_0} - \Delta|_{\alpha_0} = F_s \tag{14}$$

and states that when the amplitude of the oscillation is small, the mean load will be the same as its static value. In actuality, the mean value will depart slightly from its static value as the frequency of oscillation is increased; however, the linearization of the equations prevents this behavior from being reproduced. Taking similar steps to arrive at the unsteady portion of the load results in

$$\frac{\tilde{F}}{\alpha_1} = \frac{\left[\lambda \left.\frac{dF_l}{d\alpha}\right|_{\alpha_0} + ik(\lambda s + \sigma) - sk^2\right]}{(\lambda + ik)} - \frac{(r + iek)\left.\frac{d\Delta}{d\alpha}\right|_{\alpha_0}}{(r + iak - k^2)} \tag{15}$$

This relation represents the transfer function of the oscillating portion of the load ($\tilde{F}$) relative to the input (α_1). Separating the real and imaginary components of equation (15) yields

$$\Re\left[\frac{\tilde{F}}{\alpha_1}\right] = \left.\frac{dF_l}{d\alpha}\right|_{\alpha_0} + \frac{k^2}{(\lambda^2 + k^2)}\left(\sigma - \left.\frac{dF_l}{d\alpha}\right|_{\alpha_0}\right) + \frac{k^2(r - ae) - r^2}{(k^2 - r)^2 + (ak)^2}\left.\frac{d\Delta}{d\alpha}\right|_{\alpha_0} \tag{16}$$

and

$$\Im\left[\frac{\tilde{F}}{\alpha_1}\right] = ks + \frac{k\lambda}{(\lambda^2 + k^2)}\left(\sigma - \left.\frac{dF_l}{d\alpha}\right|_{\alpha_0}\right) + \frac{ek(k^2 - r) + akr}{(k^2 - r)^2 + (ak)^2}\left.\frac{d\Delta}{d\alpha}\right|_{\alpha_0} \tag{17}$$

and for large values of k, assuming that $k \gg \lambda$, equation (16) shows that σ is the asymptotic value of the real part of the load; similarly, equation (17) shows that s is the asymptotic value of the rate of change of the imaginary part of the load with respect to the reduced frequency. In other words,

$$\lim_{k\to\infty} \frac{\tilde{F}}{\alpha_1} = \sigma + iks \tag{18}$$

The small-amplitude equations are now in a convenient form to evaluate the six coefficients, and they can be applied over the entire incidence range, both above and below stall. To evaluate these coefficients, an experiment must be performed to obtain the load measurements during small-amplitude oscillations. The measurements are then Fourier analyzed to determine the real and imaginary components of the first harmonic. The coefficients, which are taken to be constant during the oscillation around any given mean angle, must assume values as required to satisfy the equality between the real and imaginary load measurements and those described by equations (16) and (17). After obtaining these coefficients, and knowing the static behavior of the airfoil, the governing equations (1)-(3) can be solved to obtain the load. This entire sequence is diagrammed in figure 2.

DESCRIPTION OF THE EXPERIMENT

The experiment was conducted in the 4000-liter, closed-circuit facility at the Aeromechanics Laboratory Water Tunnel, Ames Research Center (fig. 3). The test section is 21 cm wide, 31 cm high, and extends horizontally a distance of 86 cm. The airfoil selected for this study was a Boeing-Vertol VR-7, having a two-dimensional planform with a chord of 10 cm. The airfoil was positioned so that it spanned the width of the test section to within 0.015 cm of either side. In order to minimize the moment of inertia about its pitch axis, the airfoil was cast from a lightweight epoxy resin around a metal spar. The pitch axis was placed at the quarter-chord location. When installed, the spar of the airfoil extended through the test-section windows and was supported by lift and drag transducers on both sides (fig. 4). One end of the spar was adjoined to an instrumented drive shaft through a torsionally stiff coupling so that airfoil incidence and pitching moment could be measured. Frictional moments imparted by the support bearings and seals were also measured and later treated as dynamic-load tares.

Electrical instrumentation consisted of transducers for the measurement of airfoil incidence, lift (both sides), drag (both sides), total pitching moment, and the bearing and seal moments (both sides). After amplification, these signals were either appropriately summed (i.e., total pitching moment minus both frictional moments) and displayed on local monitors; or they were transmitted to a remote data acquisition system where they were digitized, averaged, and stored for later processing. Digitizing and ensemble averaging was based on two additional signals: a 360/rev pulse train that was synchronous with ωt, and a 1/rev pulse that was synchronous with the beginning of each cycle of airfoil oscillation. On-line monitoring for smoothness of the ensemble average of a particular load provided the basis to terminate the data acquisition; and the number of cycles used in generating the average, therefore, was dependent on the extent of the nonperiodic content of the signal. It is estimated that the incidence of the airfoil could be measured to an accuracy of 0.2°. Lift and drag measurements are considered to be accurate to 0.01 N and the pitching moments to 0.002 N·m.

With the airfoil set at zero incidence, the speed of the water was adjusted to produce a dynamic pressure of 689 N/m^2 (0.10 lbf/in.^{2}). This pressure corresponds to a Reynolds number of Re = 120,000 based on the chord of the airfoil. The tunnel was then operated at a fixed drive speed for the duration of the experiment. Some reduction in tunnel speed is thought to have occurred when the airfoil was stalled; however, no attempt was made to either measure or account for this degradation.

In order to obtain the asymptotic character of the real and imaginary components of the load at high frequency, say at k = 1.2, an oscillation frequency of around 4.5 Hz would be required. Inertial loads might, therefore, become a problem. The inertial loads are potentially less serious in water than in air because of the relatively low density ratio $\rho_{model}/\rho_{water}$ compared with ρ_{model}/ρ_{air}. However, at the beginning of this test it was not known whether the inertial effects on the hydrodynamic load responses could be neglected. Furthermore, there was also concern about gravitational effects (buoyancy) and the possibility of variable support loads (due to misalignments) during angle changes. The contribution of all such loads to the balance measurements is summarized schematically in figure 5.

To obtain the desired hydrodynamic load, the gravitational, support, and inertial loads must be removed from the unsteady load measurements. This can be accomplished during the data reduction phase, provided that the appropriate quantities are measured at the time of the experiment. The inertial effects can be accounted for by lowering the water in the test section and performing the same unsteady load measurements in air. The gravitational and support loads can be accounted for by performing quasi-static measurements in water (at zero flow) as well as in air. Having recorded these different results, the final hydrodynamic load can be calculated by following the procedure outlined in figure 6.

DISCUSSION OF RESULTS

Load Measurements

The variables $F_l(\alpha)$ and $\Delta(\alpha)$ are both essential elements in the math model, and they can easily be determined from the static behavior of the airfoil. Their variation with α must be established over the entire incidence range for which large-amplitude responses are to be calculated. Static measurements of lift, drag, and pitching moment are shown in figure 7. In order to evaluate the capability of the model for calculating loads under dynamic stall conditions, measurements were also made with the airfoil undergoing large-amplitude oscillations over a range of reduced frequencies (figs. 8-14).

To determine the six coefficients of the math model, small-amplitude oscillations in pitch are required around a selection of mean angles in the linear and nonlinear range. For some airfoils, the static stall angle marks the division between these two ranges; however, as can be seen from figure 7, the nonlinear range in the present case begins well below the stall angle. Within the linear range, three of the coefficients become inconsequential because Δ = 0; while among the remaining three coefficients to be evaluated, two are usually found to be constant (ref. 12). As a result of this reduction in complexity, data are needed for only a few mean angles in the linear range. In the present case the linear range appears to be so brief that little advantage can be realized in the number of mean angles to be required.

In keeping with the assumptions under which equations (16) and (17) were derived, the amplitude of oscillation was restricted to α_1 = 0.5°. Measurements were made at 13 mean angles (α_0 = 0°, 1.5°, 3°, 5°, 7°, 9°, 11°, 13°, 15°, 17°, 19°, 21°, and 23°) and 11 reduced frequencies (k = 0.025, 0.05, 0.10, 0.15, 0.2, 0.3, 0.4, 0.5, 0.7, 0.9, and 1.2). Excluding the lowest-frequency case, these small-amplitude results are presented in figures 15(a)-15(m) for the lift, drag, and pitching moment. Also included are the first-harmonic equivalents of these data (shown as dashed lines). The high frequency component of the lift and pitching-moment signals, especially apparent for values of incidence below 1.5°, is due to Karman-vortex shedding from the airfoil. The frequency of this vortex shedding appears to be around 47 Hz. The first-harmonic curves appear to compare well with the actual data, and therefore will be accepted in the following analysis as an accurate replacement for the small-amplitude measurements. Examining these first-harmonic curves in more detail, the real and imaginary components of each load modulus are separated and shown in figure 16. For any given load, these components correspond to $\Re[\tilde{F}]$ and $\Im[\tilde{F}]$ in equations (16) and (17), and as such provide the basis on which the six coefficients can be determined.

Coefficient Evaluation

The most important step in finalizing the governing differential equations for the loads on a given airfoil is the determination of the equation parameters. Specification of the parameters $F_l(\alpha)$ and $\Delta(\alpha)$ evolves directly from the static load measurements, which are shown in figures 17 and 18. To smooth out any irregularities in the experimental data, and to provide a more well-behaved variation with incidence so that reasonably bounded derivatives could be calculated, the static curves have been fitted with piecewise-cubic splines. Both Δ and $d\Delta/d\alpha$ are derived using these curve fits.

Evaluation of the six coefficients is less straightforward. Generally speaking, coefficients cannot be found which

precisely satisfy equations (16) and (17) over the frequency range desired, and at the same time culminate in a smooth dependence on incidence. Instead, solutions must be sought at each mean angle which satisfy the equations for $\Re[\tilde{F}]$ and $\Im[\tilde{F}]$ in a least-squares sense. Furthermore, experience has shown that a particular order should be followed in establishing the set of coefficients. Since the primary intent of this presentation is to provide an example of the application of the ONERA model, the following discussion will be limited to the *lift* coefficient so that the method can be discussed in more detail and with greater clarity.

Before evoking this procedure, it is useful to identify those coefficients that, from experience, have been found to be independent of incidence and whose values are essentially declarable by inspection. Considering the linear range, equation (16) states that

$$\Re\left[\frac{\tilde{F}}{\alpha_1}\right] = \frac{\lambda^2 \left.\dfrac{dF_l}{d\alpha}\right|_{\alpha_0} + \sigma k^2}{\lambda^2 + k^2} \tag{19}$$

This expression can be used to examine the bounds on $\Re[\tilde{F}/\alpha_1]$ as k is varied. On one extreme, $k = 0$ requires that $\Re[\tilde{F}/\alpha_1] = (dF_l/d\alpha)_{\alpha_0}$. On the other extreme, letting $k \rightarrow$ *large* suggests that $\Re[\tilde{F}/\alpha_1] \rightarrow \sigma$. Although σ is in general a function of α, its value can be readily approximated in the linear range. It can also be shown that the average value for $\Re[\tilde{F}/\alpha_1]$ over this extreme range of reduced frequencies is $[(dF_l/d\alpha)_{\alpha_0} + \sigma]/2$, and that this value is obtained when $k = \lambda$. Accordingly, a second coefficient can be approximated in the linear range. Experience also indicates that the magnitude of λ has an effect on the manner in which the real and imaginary asymptotes are approached in the linear range; small values accelerate the approach and large values cause the approach to be more gradual (ref. 13). Additionally, some observations have been made about λ in the nonlinear range. Experience has also shown that for low and medium reduced frequencies, $\tilde{F}_2$ is dominant over $\tilde{F}_1$. Recalling from equation (15) that the first term of the second member represents $\tilde{F}_1$ and that the second term represents $\tilde{F}_2$, it is evident from the composition of these two quantities that the value of λ is of no consequence in this case. Furthermore, an examination of equation (18), which is valid at high reduced frequencies, shows that λ is completely absent from the expression for $\tilde{F}$ (which equals the sum of $\tilde{F}_1$ and $\tilde{F}_2$). This implies that the value of λ has a negligible effect on the math model for all frequencies in the nonlinear range, and that its value in the linear range can simply be extrapolated over the entire incidence range. As a result, it has been the practice at ONERA to simply accept a constant value for λ. In keeping with this attitude, λ can be approximated from the data for the real component of the lift at $\alpha_0 = 0°$ shown in figure 16(a):

$$\lambda = 0.25\ (\forall\alpha) \tag{20}$$

Another coefficient that appears to vary little with incidence is s. Representing the asymptotic slope of the imaginary part of the load at high reduced frequencies, the experimental data presented in figure 16 confirm that s can indeed be approximated by a constant over nearly the entire incidence range. For those cases in the nonlinear range where the asymptotic value has not yet been reached at the highest reduced frequency under consideration (i.e., at $\alpha_0 = 23°$), it is common practice to accept the extrapolated value for s from the linear range. Taking an average of these measurements yields

$$s = 0.12\ (\forall\alpha) \tag{21}$$

Determination of the remaining four coefficients is more laborious since they must be considered simultaneously, they typically all vary with incidence in some nonlinear fashion, and yet nowhere do they satisfy the governing equations precisely. The optimizing algorithm selected for this task is based on a numerical scheme that finds solutions to equations (16) and (17) so as to produce the *least* accumulated disagreement with the measured load responses. Considering that these coefficients will vary mostly in the nonlinear range, and since Δ is a more direct measure of the departure from the linear curve than is α, all four coefficients will be considered as explicit functions of Δ instead of α. This implies that their values in the linear range (where α may vary greatly) will be invariant and equal to their values at $\Delta = 0$.

Exercising the optimization routine with all four coefficients initially unknown yields an expected dispersion of solutions (fig. 19). The customary step at this point in most parameter-identification procedures is to recognize which feature or characteristic of the data is most prominent, and on which coefficient is this feature most dependent. Sensitivity tests have shown that the location of the peak values of both the real and imaginary responses is such a feature, and that it is strongly (but not solely) dependent on r. The optimization for r will therefore be examined first, and a curve defined that best describes this coefficient's variation with Δ. Although a simple parabolic relationship might have sufficed in this case, the distribution of points for the other three coefficients indicated that a more flexible curve fit would be necessary. To be consistent, a piecewise-cubic spline was chosen for all curve fits. A curve is first faired through the data and then a set of manufactured data points is defined along this curve. On any given interval between these manufactured points, the curve is described by:

$$\sqrt{r} = \xi_{m0} + \xi_{m1}(\Delta_m - \alpha) + \xi_{m2}(\Delta_m - \alpha)^2 + \xi_{m3}(\Delta_m - \alpha)^3 \tag{22}$$

where m represents the interval for which $\alpha_m < \alpha < \alpha_{m+1}$. Obviously, this curve fit is not unique, and a great deal of subjectivity can influence the weighting of various data points. In such cases, experience can become an important factor in the shaping of curves through the data. In any case, it may still be necessary to make certain adjustments to the coefficients after reviewing how the model calculates a large-amplitude case. For example, assume that several calculations are performed for an airfoil undergoing large-amplitude oscillations through stall. Furthermore, assume that the airfoil then returns to attached flow conditions with suspiciously little change in the hysteresis, in each case, as the reduced frequency is increased. This may suggest that the values of a and r in the linear range (hence their value at $\Delta = 0$) need to be modified to allow less damping and more response in the equation for $\tilde{F}_2$. This behavior could not have been foreseen from small-amplitude tests, and perhaps not even from large-amplitude tests where the reduced frequency is small. However, for large-amplitude oscillations at moderate reduced frequencies, the time-history effects become sufficiently significant and can influence the loads even though the forcing function in the equation for $\tilde{F}_2$ may be locally small or zero.

Although the curve for r can be regarded as provisional, and eventually may be modified, it will be considered as fixed for the present. With λ, s, and r specified, the optimization process is repeated; but now only σ, a, and e are considered to be unknown. As can be observed in figure 20, the dispersion of points for the remaining three coefficients is considerably reduced, thereby the plotting of succeeding curve fits can be done with greater confidence. Representing the asymptotic value of the real part of the load, the data for σ will be considered as the most reliable even though the maximum reduced frequency at each α_0 generally appeared to be too low to reveal the actual asymptote. A simple curve fit through the data for σ would be especially infeasible in this case. For the special case when $\Delta = 0$, the value for σ used to evaluate λ (recall when $\alpha = 0°$) also applies. For values of Δ near zero, σ is perhaps more dependent on α (explicitly) than on Δ; whereas for larger values of Δ, a very demonstrative dependence on Δ is observed. In fairing a curve through the data for σ, those points for which $\Delta \approx 0$ (and which may eventually require some explicit dependence on α) were ignored and an expression similar to (22) was established for $\sigma(\Delta)$.

With only two unknowns remaining, a and e, the optimization procedure yields a set of new values for each coefficient with even less dispersion (fig. 21). Like σ, both a and e exhibit a behavior around $\Delta \approx 0$ that may require an explicit dependence on α if strict adherence is to be retained. However, in keeping with the decision made for σ, those points will be ignored for the present. Instead, the value of each coefficient at $\Delta = 0$ will be that obtained by extending the curve from higher values of Δ. The coefficient a affects both the amplitude and width of the mid-frequency wave that is characteristic of the real and imaginary responses in the nonlinear range ($\alpha_0 > 9°$). The data in this range appear to be reasonably well behaved so that a curve similar to the one described by (22) can be established for $a(\Delta)$. This curve, when extrapolated back to $\Delta = 0$, yields a value for a that is substantially higher than what the optimizations (as well as the experimental observations) require. During a calculation for an airfoil at low incidence recovering from stall, this region will contribute significantly to the damping in the equation for $\tilde{F}_2$. Therefore, some modification to the curve for a as $\Delta \to 0$ can be anticipated.

The optimization process can now be narrowed down to the evaluation of a single unknown, e, and the resulting distribution of computed values for this coefficient is shown in figure 22. Although the variation of e with Δ is quite different after stall ($\Delta > 0.9$) compared with its behavior over the remainder of the nonlinear range, the fitting of a piecewise-cubic spline to the data is straightforward. As can be seen from the governing equations (1)-(3), the coefficient e contributes only to the forcing function for $\tilde{F}_2$. Aside from its impact on the time history of the solution as $\Delta \to 0$, the fact that e appears as a product of $\dot{\Delta}$ means that its value in the linear range is not important. The unknown e affects the amplitude of both the real and imaginary parts of the response in the nonlinear range as well as the phase of the response relative to the motion of the airfoil. Negative values of e cause a phase lag with respect to α; and as the magnitude of e increases, the phase lag tends toward 90°. The opposite trend occurs for positive values of e.

To conclude the optimization process, the expressions obtained for the six coefficients will be coupled with equations (16) and (17) to examine the real and imaginary components presently represented by the model. The focus of the examination will be on how well the model reproduces the real and imaginary components of the lift coefficient obtained in the experiment. Figures 23 and 24 show the comparison between the experimental values (discrete symbols) and the calculated values (solid curves) at the mean angles for which data exist. Excellent agreement is obtained through $\alpha_0 = 15°$; however, the calculations resemble only the trend of the experiment for mean angles between $17° \leqslant \alpha_0 < 23°$. That such good agreement exists between the calculations and the experiment for low values of α_0 (in spite of a disregard for many of the computed optimizations in the range $\Delta \approx 0$) suggests that the small amplitude tests provide little information about the coefficients r, σ, a, and e in this domain. The less satisfactory agreement between the calculations and the experiment for the higher values of α_0 ($\Delta > 0.2$) may be either due to an inadequacy in the model's equations to account for a fully separated flow or due to the optimization process which assigned equal weighting to each of the experimental observations. In any case, a judgment on the consequence of this shortcoming will have to await the calculation of a large-amplitude case. The topographies of the real and imaginary components over the k-α_0 plane are

shown in figure 25 for the experimental data and in figure 26 for the math model using the coefficient optimizations (recall fig. 22).

Large-Amplitude Calculations

Using the expressions for the six coefficients obtained above, the unsteady load for a prescribed airfoil motion can be calculated from equations (1)-(3). First, the governing system must be reduced to a set of first-order equations in order to use a standard differential-equation solver. The governing equations are readily transformed to the following:

$$\left.\begin{aligned} F &= F_1 + F_2 \\ \dot{F}_1 &= -\lambda F_1 + \lambda F_l + (\lambda s + o)\dot{\alpha} + s\ddot{\alpha} \\ \dot{F}_2 &= F_3 \\ \dot{F}_3 &= -aF_3 - rF_2 - (r\Delta + e\,\dot{\Delta}) \end{aligned}\right\} \qquad (23)$$

Given a set of initial conditions, say $F_i(\tau = 0) = 0.0$ ($i = 1, 2, 3$), a time marching solution can be generated with dimensionless time τ, the independent variable, expressed as

$$\tau = \frac{\omega t}{k} = \left(\frac{2\pi}{k}\right)\frac{n}{\aleph}\ , \quad (n = 1,2,3,\ldots) \qquad (24)$$

where $\aleph$ denotes the total number of increments in one cycle. The number of time steps required to reach a steady-state solution depends on the magnitude of the unsteady airfoil motion. Therefore, the higher the reduced frequency, k, the greater the number of time steps required.

By requiring that $\tau = 0$ when $\alpha = 0°$, the sinusoidal motion of the airfoil can be described by

$$\alpha = \alpha_0 - \alpha_1 \cos \tau k \qquad (25)$$

The calculations are based on a mean angle and amplitude of oscillation of $\alpha_0 = \alpha_1 = 10°$ and a range of reduced frequencies from $0.002 \leqslant k \leqslant 0.25$. These conditions were chosen because they challenge the math model to accurately predict the dynamic loads occurring during deep stall and with varying degrees of overshoot (values above static C_l-*max*) and hysteresis. The results for the lift coefficient are shown in figures 27(a)-27(g), and a steady-state solution was reached during the first cycle of oscillation for all of the cases calculated.

Each figure is subdivided into three subplots. The right-hand subplot displays the calculated components of the lift coefficient, F_1 and F_2, as well as the measured static behavior of the airfoil (dashed line). The lower-left subplot shows the forcing functions f_1 and f_2 that appear in the computation of equations (2) and (3), respectively. The upper-left subplot shows the calculated value for the lift coefficient, $F_1 + F_2$, along with the actual measured response (dashed line). The results given in these figures indicate that the math model does reproduce qualitatively the increases in both overshoot and hysteresis as the reduced frequency is increased. Even the slight surge in the lift response just prior to stall (as well as just prior to reattachment) is correctly predicted by the math model (i.e., see fig. 27(c)). This characteristic is believed to be attributable to the term $\dot{\Delta}$ that appears in the forcing function for F_2, and reflects the abrupt static stall that was actually measured in the experiment (recall figs. 17 and 18). However, the extent of both the overshoot and the hysteresis appears to be quantitatively incorrect. In addition, the calculated lift coefficient during the deep-stall phase of the motion ($\dot{\alpha} < 0$) is generally too low, and becomes even more so as the reduced frequency is increased. It appears that a decrease in accuracy results when the values of both the reduced frequency and the amplitude of oscillation are large.

To overcome the quantitative disagreement in the lift overshoot between the calculations and the measurements, it appears that the math model must be amended to better account for the effects of stall delay. This eventuality was envisaged early on by the architects of this model (ref. 8). Consequently, an allowance for the observed delay in stall was provided for through the product of a unity-step function, ϵ, with the forcing function on F_2 in equation (3). The intent of this procedure is to disable the forcing function on F_2 during a certain period of time, $\delta\tau$, beginning when the static stall angle is exceeded. This dimensionless-time interval is defined by

$$\delta\tau = \left(\frac{2U_\infty}{c}\right)\delta t \qquad (26)$$

and typically has been set at about $\delta\tau \approx 10$ in recent applications of the model (ref. 12). After satisfying this delay in time, the forcing function then assumes its current value. The time-delay concept (a prominent feature in ref. 6) is physically based on the overshoot caused by the stall vortex. This vortex induces additional lift on the airfoil when passing over the airfoil.

Since vortex shedding just prior to reattachment is generally not obvious from available experimental data, it is unlikely that a similar time-delay factor applies to the stall recovery phase of the cycle. However, since a hysteresis clearly exists in the static response, it does seem appropriate to distinguish between $\dot{\alpha} > 0$ and $\dot{\alpha} < 0$ in terms of the definitions for Δ (and therefore $\dot{\Delta}$). Doing so would automatically establish a persistence in the forcing function on F_2 and cause an extension of the hysteresis. A proper accounting for the stall-delay effect during $\dot{\alpha} > 0$, as well as the recognition of a separate Δ during $\dot{\alpha} < 0$, both have a potential for

improving substantially the quantitative accuracy of the math model. As such, these considerations need to be evaluated before proceeding to the modeling of the drag and moment responses.

CONCLUSIONS

A semiempirical model, developed at the Office National D'Etudes et de Recherches Aerospatiales (ONERA) to predict the unsteady loads on an airfoil that is experiencing dynamic stall, has been described. Calculations were performed for comparing with results from an experiment in the Aeromechanics Laboratory Water Tunnel. The static and dynamic data obtained were for a Boeing-Vertol VR-7 airfoil at a Reynolds number of Re = 120,000. Although lift, drag, and moment responses (both small and large amplitude) have been included in this study, the comparisons that have been discussed, including the following conclusions, are confined to the lift coefficient.

1. The procedure, established at ONERA to identify the six coefficients in the math model, was found to be straightforward and the trends consistent with earlier investigations when used with small-amplitude experimental data.

2. Coefficient optimizations were found that produced excellent agreement between calculated and measured small-amplitude responses, as long as the mean angles were within $0° \leqslant \alpha_0 \leqslant 15°$. For the higher mean angles that correspond to deep stall, $17° \leqslant \alpha_0 \leqslant 23°$, the calculated small-amplitude responses based on optimized coefficients in this range were not in good agreement with measured values.

3. The shape of the static-lift curve in the present experiment differs from the idealized version (as well as from measurements on other airfoils at higher Reynolds numbers) around which the math model was originally formulated. In the present case, the static curve becomes nonlinear prior to stall and deviates greatly from the classic tangent to the data near $\alpha = 0°$. Furthermore, when stall does occur, it is quite abrupt. The extent to which this behavior affects the applicability of the model has not yet been resolved.

4. A comparison between calculations and measurements for large-amplitude cases at various reduced frequencies shows that the math model does reproduce qualitatively the increases in both dynamic-lift overshoot (values above static $C_{l\text{-}max}$) and hysteresis as the frequencies are increased. Even the slight surge in the lift response just prior to stall (as well as just prior to reattachment) is correctly predicted by the math model. However, the extent of both the overshoot and the hysteresis appears to be quantitatively incorrect. In addition, the calculated lift coefficient during the deep-stall phase of the motion is generally too low, and becomes even more so as the reduced frequency is increased. It appears that a decrease in accuracy results when the values of both the reduced frequency and the amplitude of oscillation are large.

5. It is believed that the quantitative accuracy of the math model can be substantially improved by incorporating a time-delay factor to account for the delay in stall during the $\dot{\alpha} > 0$ portion of the cycle. Also, based on the observed static hysteresis, an improvement in the extent of the dynamic hysteresis may be realized by allowing for a separate Δ function during the $\dot{\alpha} < 0$ portion of the cycle. It is recommended that consideration be given to both of these potential improvements to the model before examining the drag and moment responses.

Ames Research Center
National Aeronautics and Space Administration
Moffett Field, California 94035, June 18, 1984

REFERENCES

1. Carr, L. W.; McAlister, K. W.; and McCroskey, W. J.: Analysis of the Development of Dynamic Stall Based on Oscillating Airfoil Experiments. NASA TN D-8382, 1977.
2. McAlister, K. W.; and Carr, L. W.: Water Tunnel Visualizations of Dynamic Stall. Trans. ASME, J. Fluids Eng., vol. 101, 1979, pp. 376-380.
3. McAlister, K. W.; Carr, L. W.; and McCroskey, W. J.: Dynamic Stall Experiments on the NACA 0012 Airfoil. NASA TP-1100, 1978.
4. Prouty, R. W.: Practical Helicopter Aerodynamics. PJS Publications, Inc., Peoria, Illinois, 1982.
5. McCroskey, W. J.: The Phenomenon of Dynamic Stall. NASA TM-81264, 1981.
6. Beddoes, T. S.: Representation of Airfoil Behaviour. Vertica, vol. 7, no. 2, 1983, pp. 183-197.
7. Gangwani, Santu T.: Synthesized Airfoil Data Method for Prediction of Dynamic Stall and Unsteady Airloads. Presented at the 39th Annual Forum of the American Helicopter Society, St. Louis, Missouri, May 1983, pp. 15-33.
8. Dat, R.; Tran, C. T.; and Petot, D.: Modele Phenomenologique de Decrochage Dynamique sur Profil de Pale d'Helicoptere. ONERA TP, no. 1979-149, 1979.
9. Rogers, J. P.: Application of an Analytic Stall Model to Dynamic Analysis of Rotor Blades. Proc. Eighth European Rotorcraft Forum, Aix-en-Provence, France, Aug.-Sept. 1982.
10. Rudy, D. J.: Three Interpretations of the ONERA Dynamic-Stall Model with Applications to Rotor Blade Flapping Response. M.S. Thesis, Washington Univ., Sever Institute of Technology, St. Louis, Missouri, 1983.
11. Tran, C. T.; and Petot, D.: Semi-Empirical Model for the Dynamic Stall of Airfoils in View of the Application to the Calculation of Responses of a Helicopter Blade in Forward Flight. Vertica, vol. 5, no. 1, 1981, pp. 35-53. (Also published in ONERA TP, no. 1980-103, 1980.)
12. Petot, D.: Progress in the Semi-Empirical Prediction of the Aerodynamic Forces due to Large Amplitude Oscillations of an Airfoil in Attached or Separated Flow. ONERA TP 1983-111, 1983.
13. Petot, D.; and Loiseau, H.: Algorithme de lissages successifs pour la recherche du modele semi-empirique de prevision des forces aerodynamiques instationnaires developpe a l'ONERA. ONERA RT 12/1841 RY, 1981. (Translation published as NASA TM-76681, 1982.)

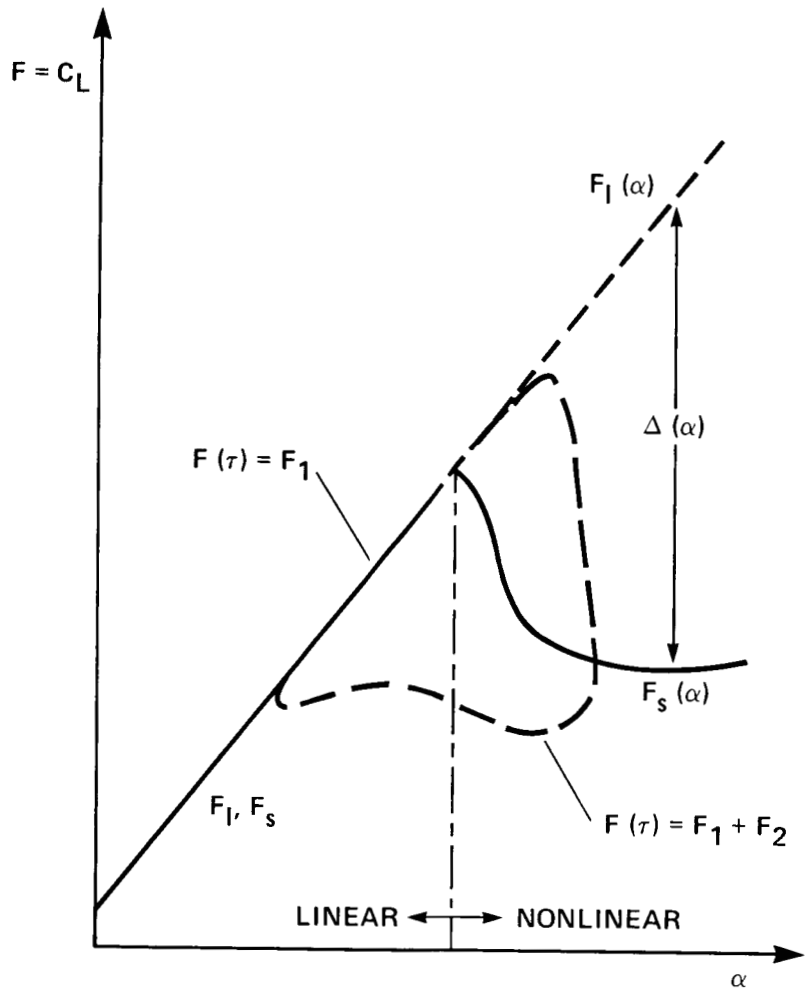

Figure 1.– Relation between variables used in the math model.

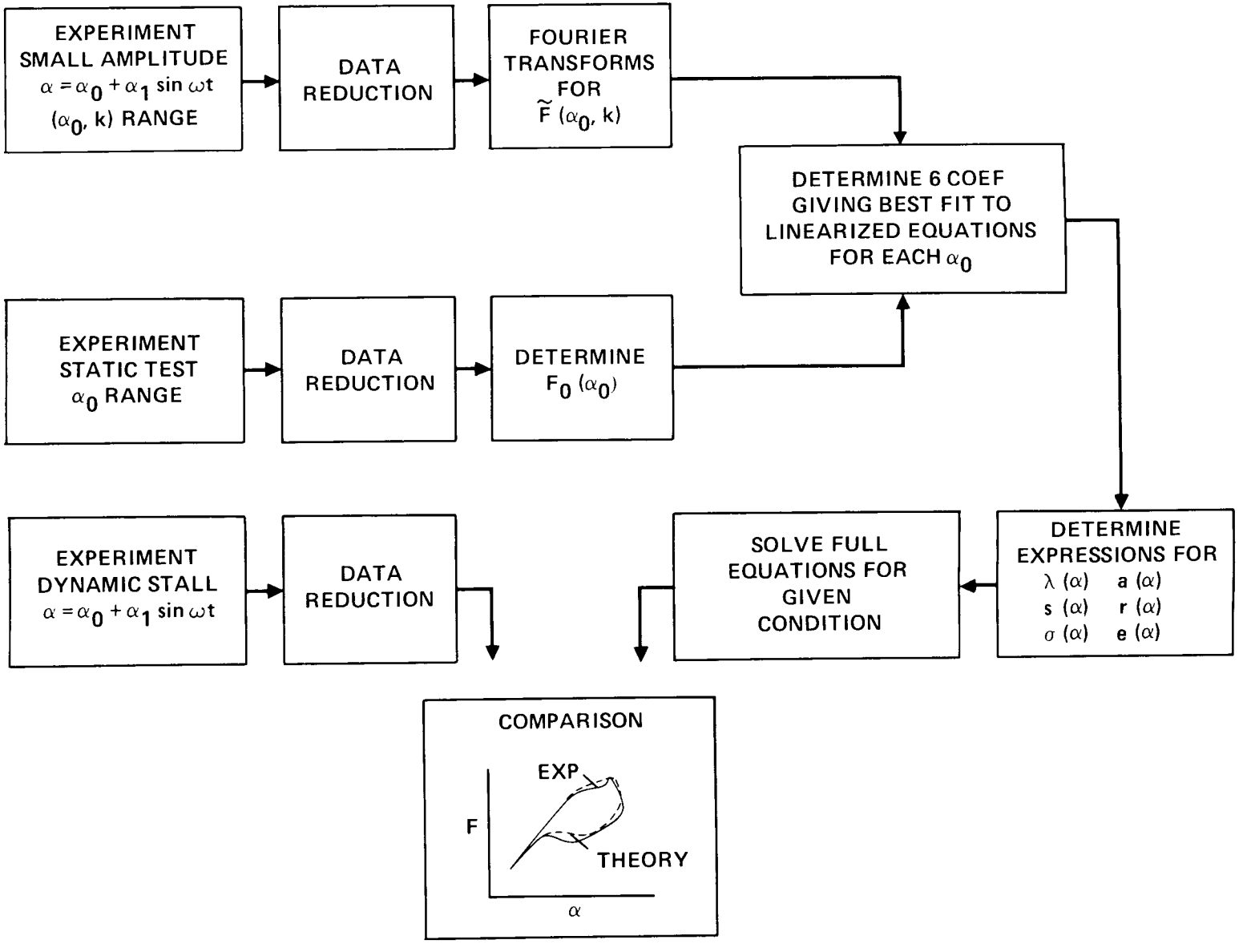

Figure 2.– Evaluation of coefficients and comparison with large-amplitude data.

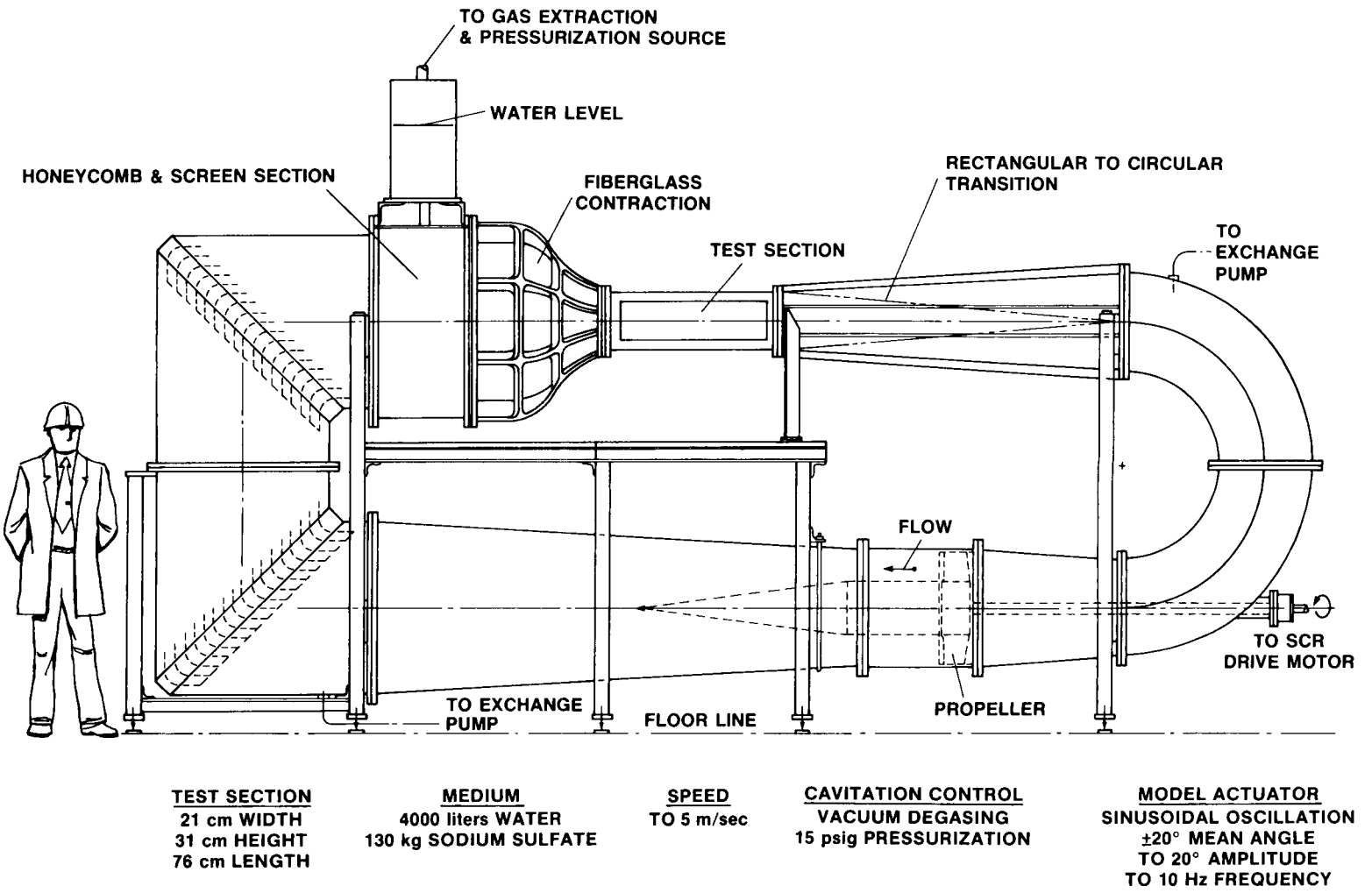

Figure 3.– Aeromechanics Laboratory 21- by 31-Centimeter Water Tunnel.

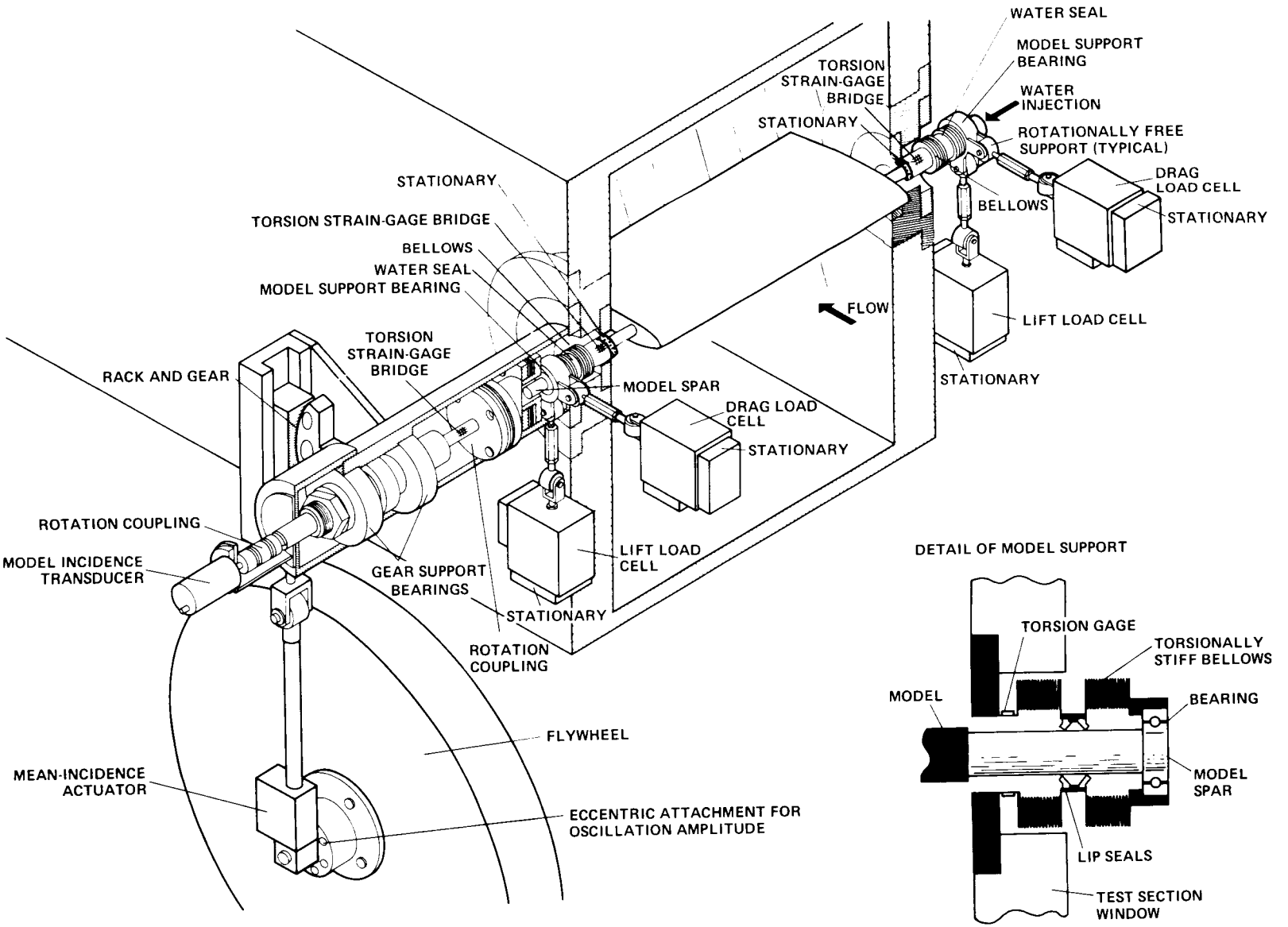

Figure 4.– Model installation and balance system for force and moment.

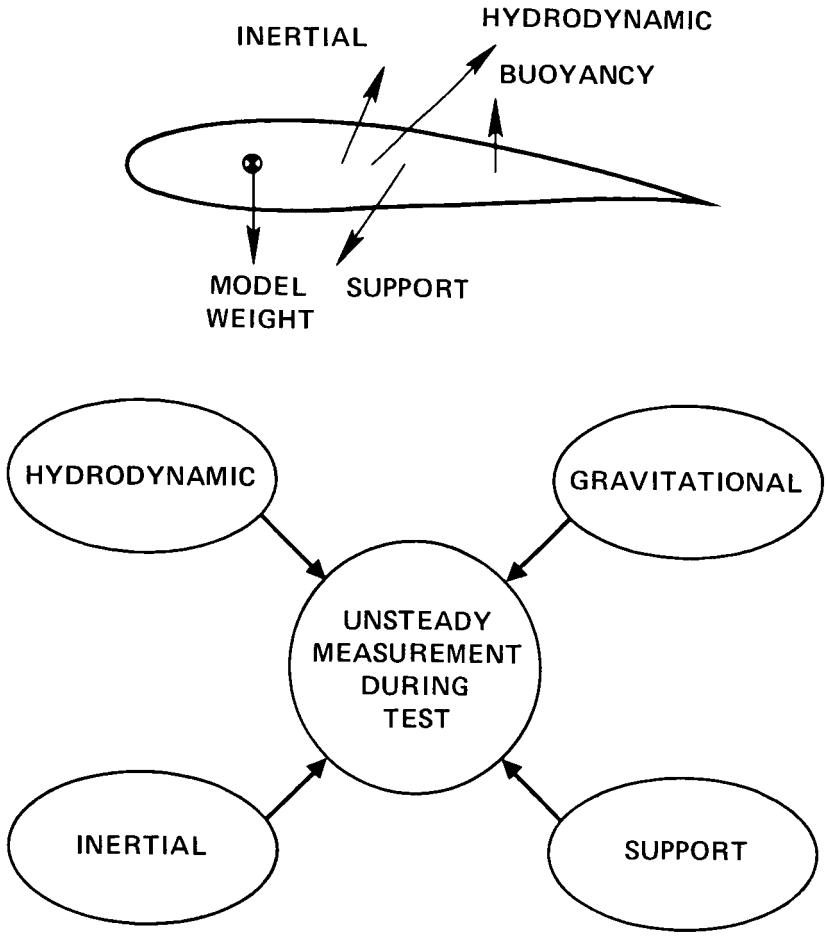

Figure 5.– Load contributions to balance measurements.

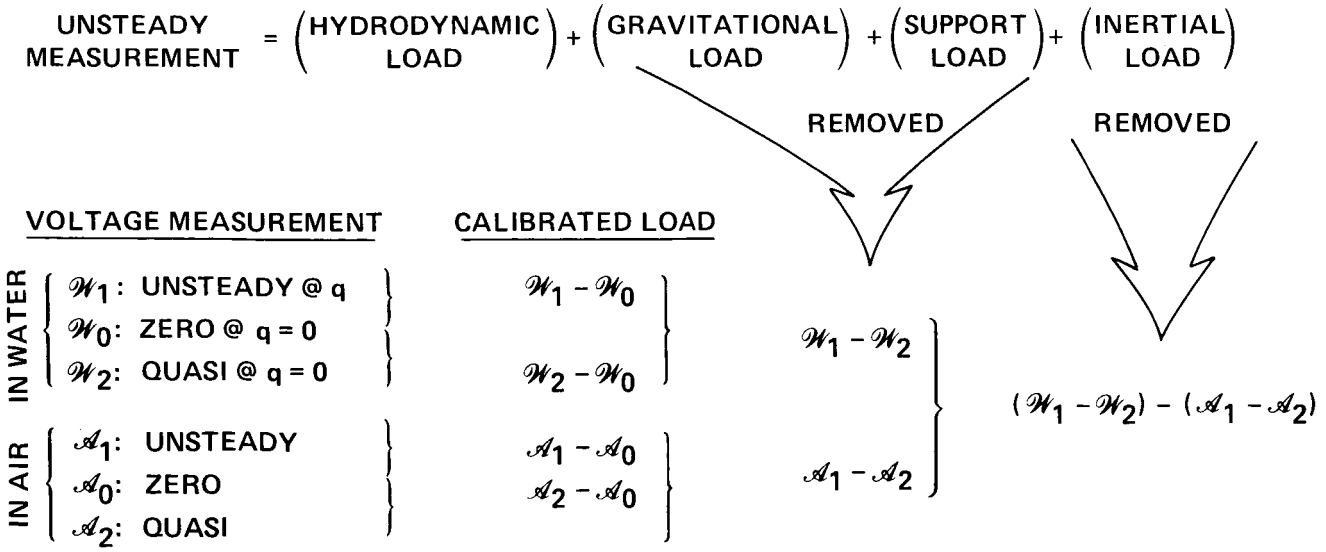

Figure 6.– Procedure for eliminating tares from unsteady load measurements.

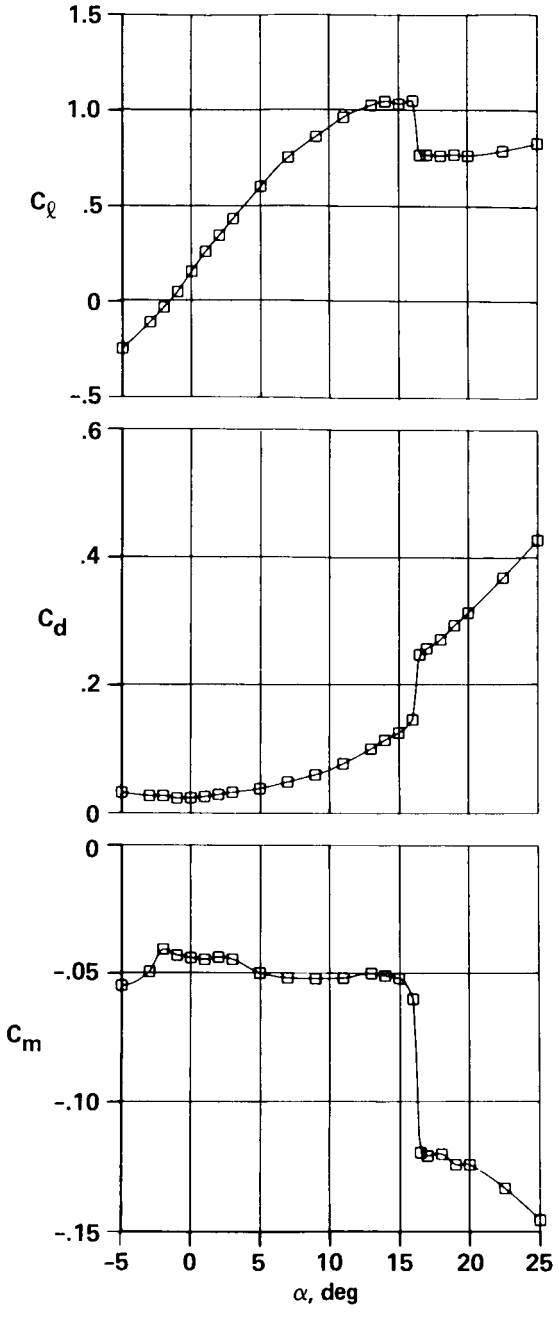

Figure 7.– Variation of static-load coefficients with incidence.

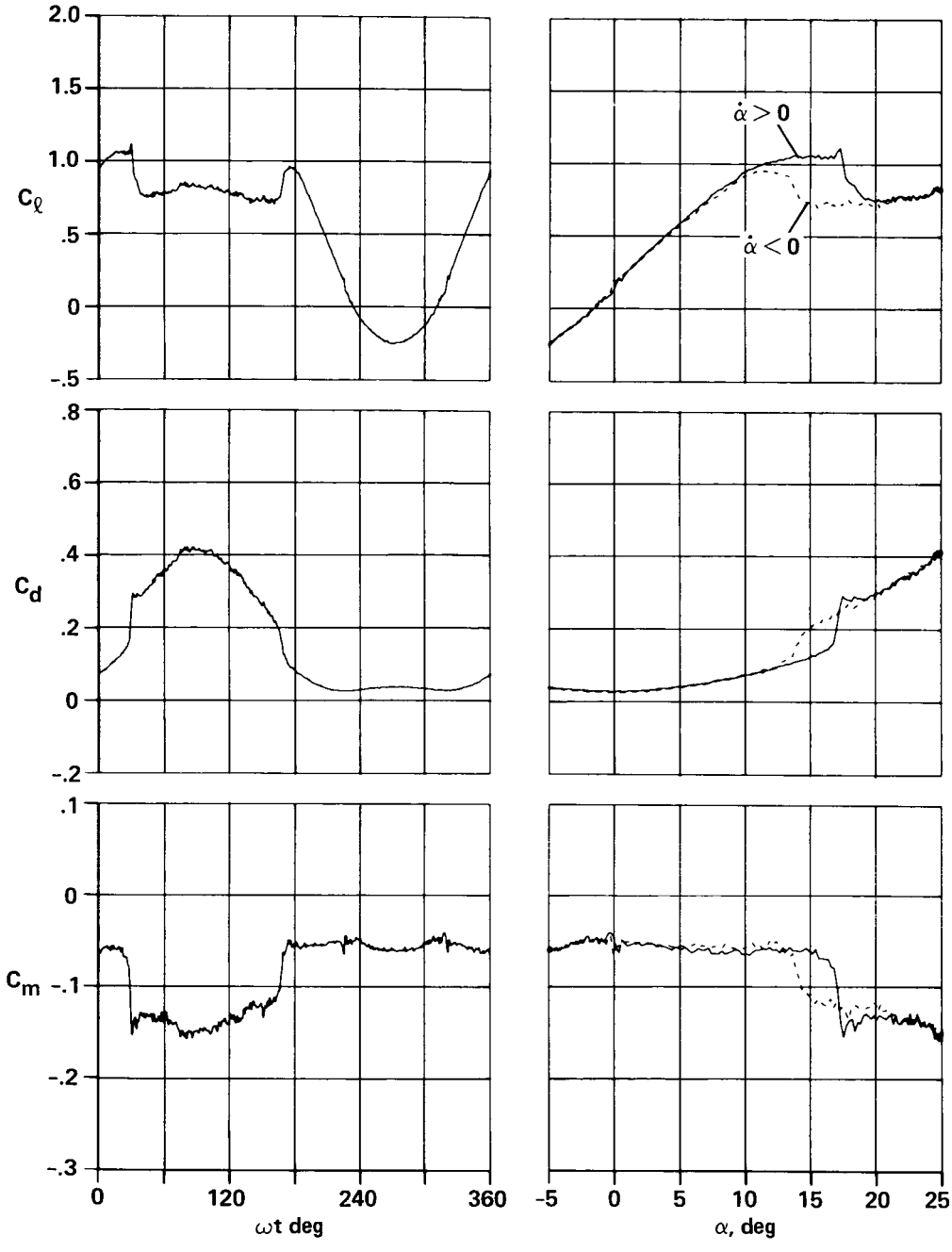

Figure 8.– Load measurements for $\alpha = 10° + 15° \sin \omega t$ at $k = 0.002$.

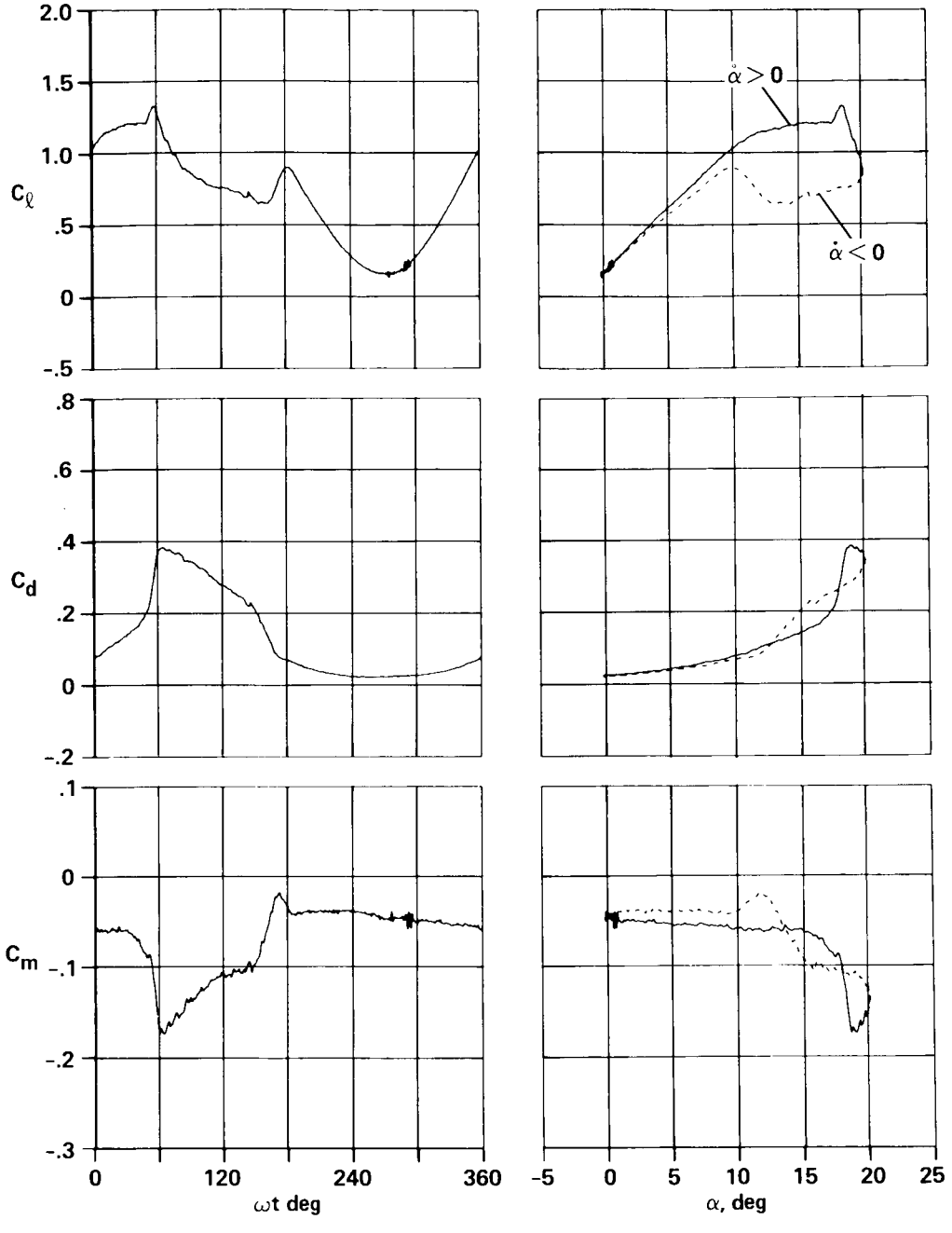

Figure 9.– Load measurements for $\alpha = 10^\circ + 10^\circ \sin \omega t$ at $k = 0.02$.

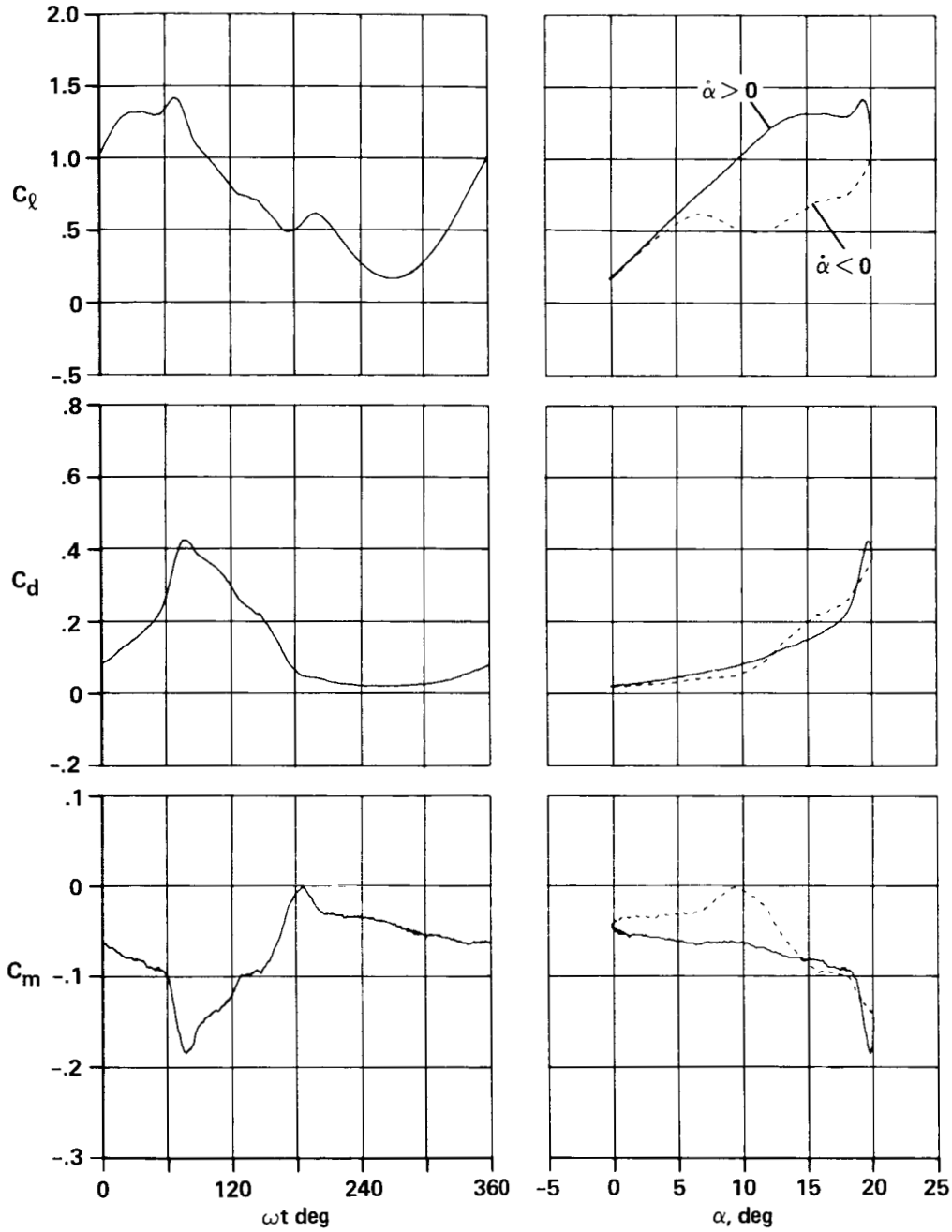

Figure 10.– Load measurements for $\alpha = 10^\circ + 10^\circ \sin \omega t$ at $k = 0.05$.

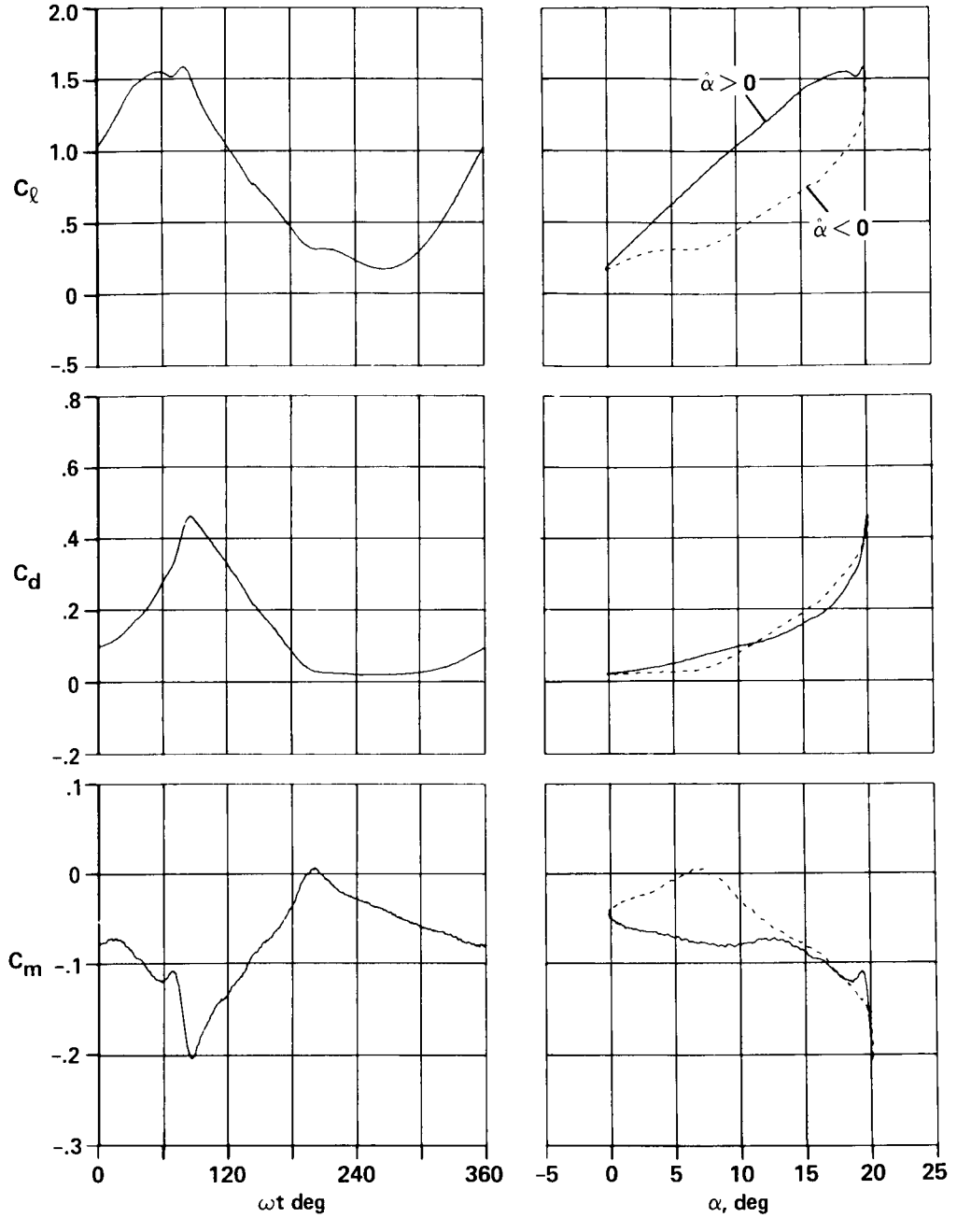

Figure 11.– Load measurements for $\alpha = 10^\circ + 10^\circ \sin \omega t$ at $k = 0.10$.

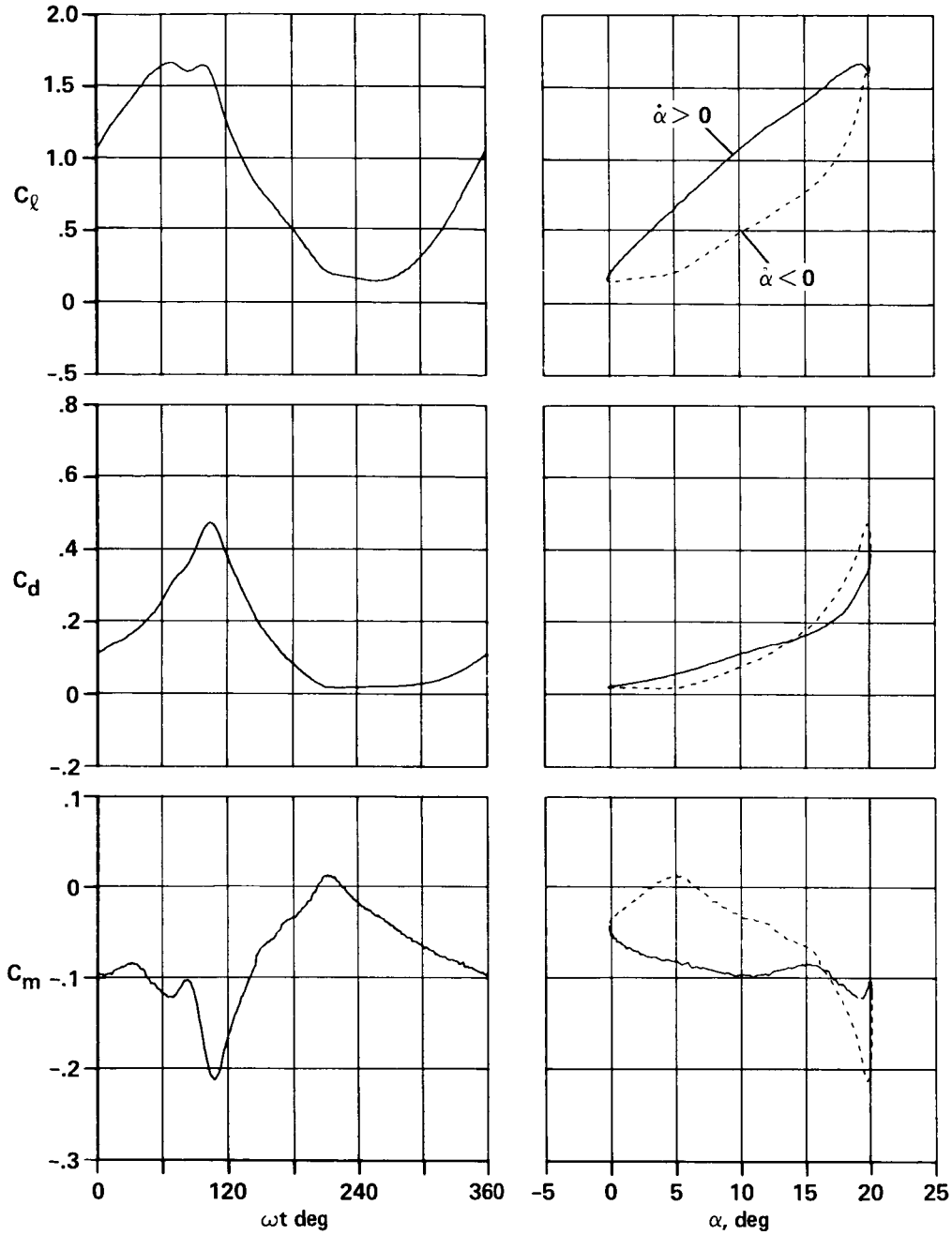

Figure 12.– Load measurements for $\alpha = 10° + 10° \sin \omega t$ at $k = 0.15$.

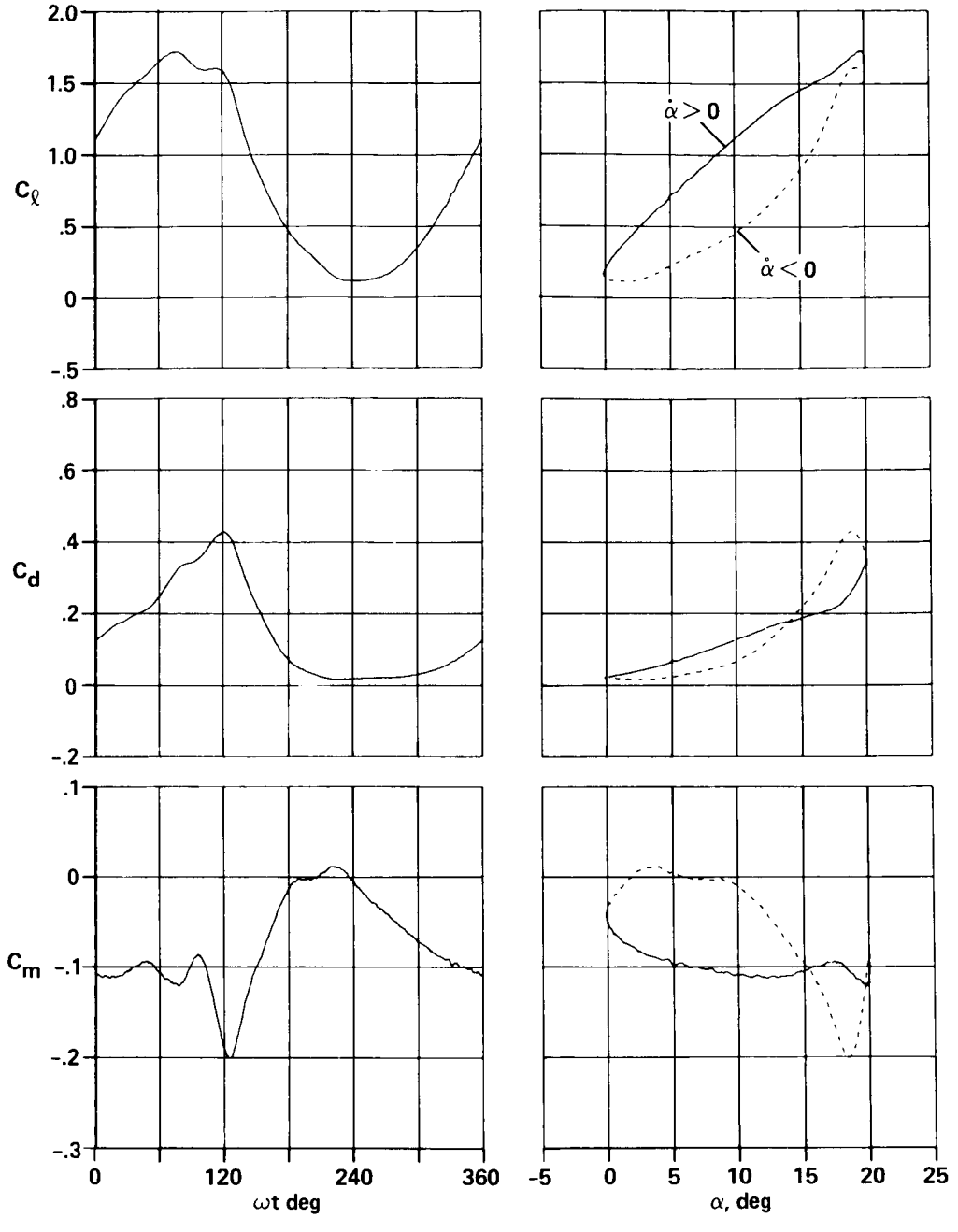

Figure 13.– Load measurements for $\alpha = 10^\circ + 10^\circ \sin \omega t$ at $k = 0.20$.

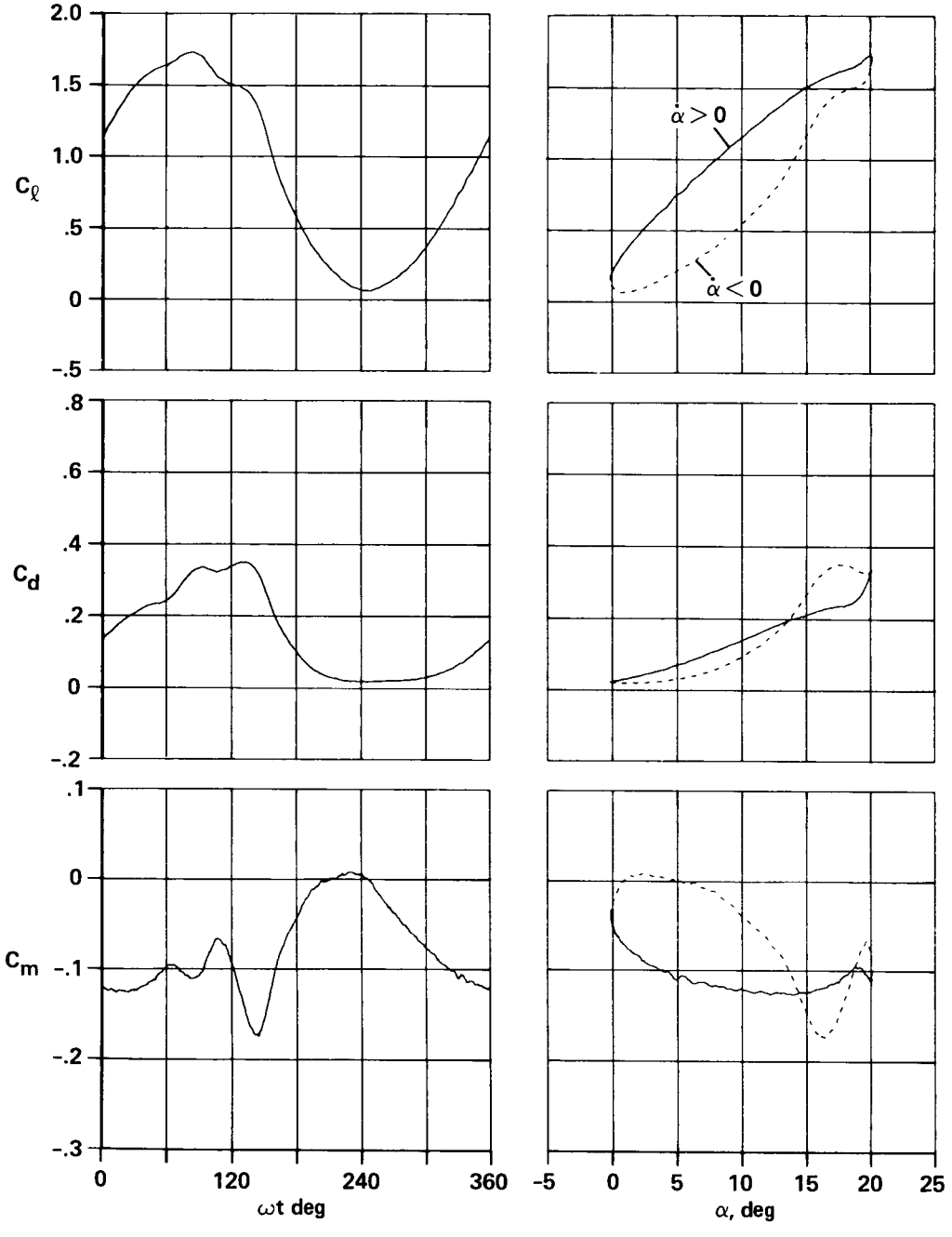

Figure 14.– Load measurements for $\alpha = 10° + 10° \sin \omega t$ at $k = 0.25$.

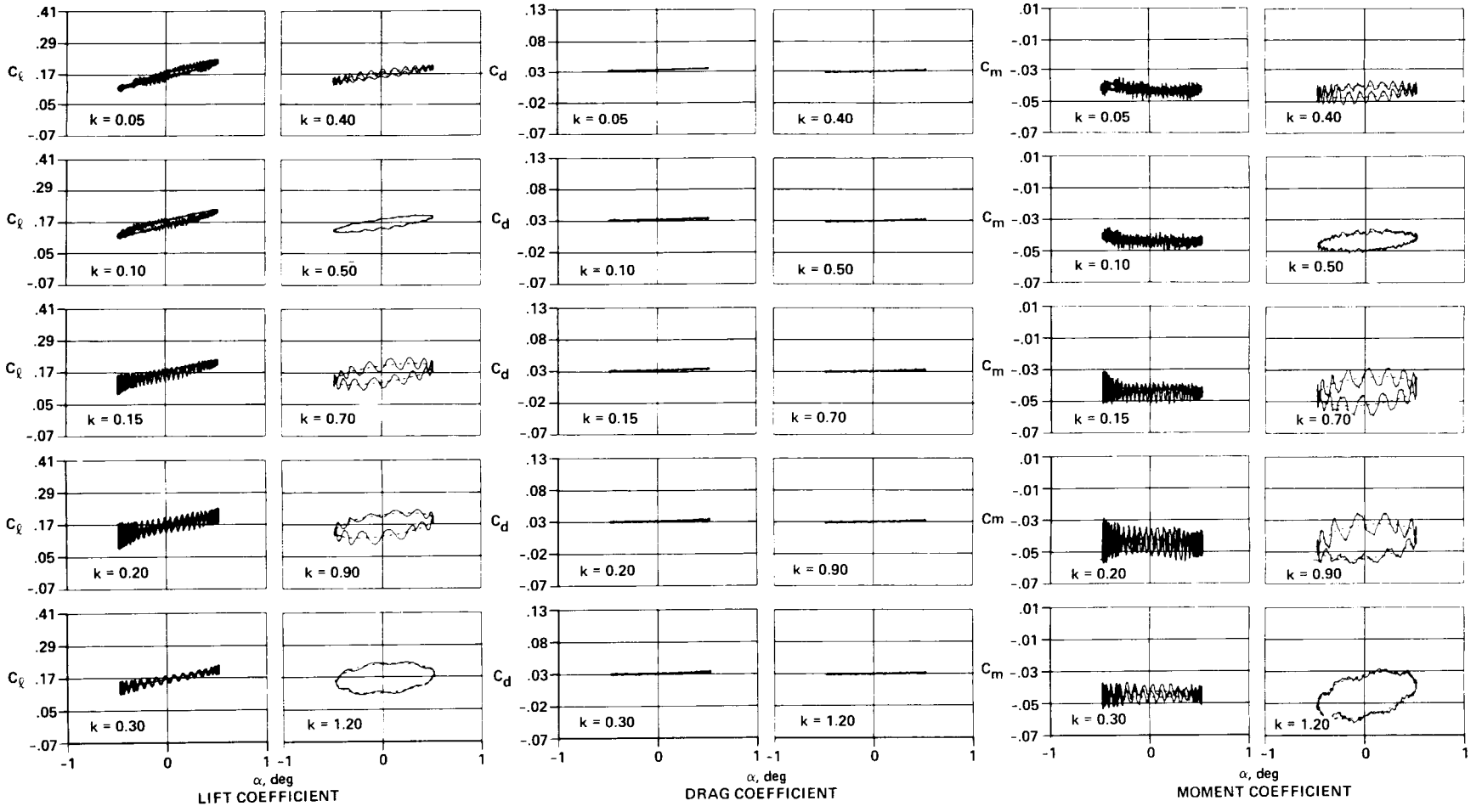

(a) $\alpha_0 = 0.0°$.

Figure 15.– Comparison between small-amplitude results from experiment (solid line) and first-harmonic equivalents (dashed line).

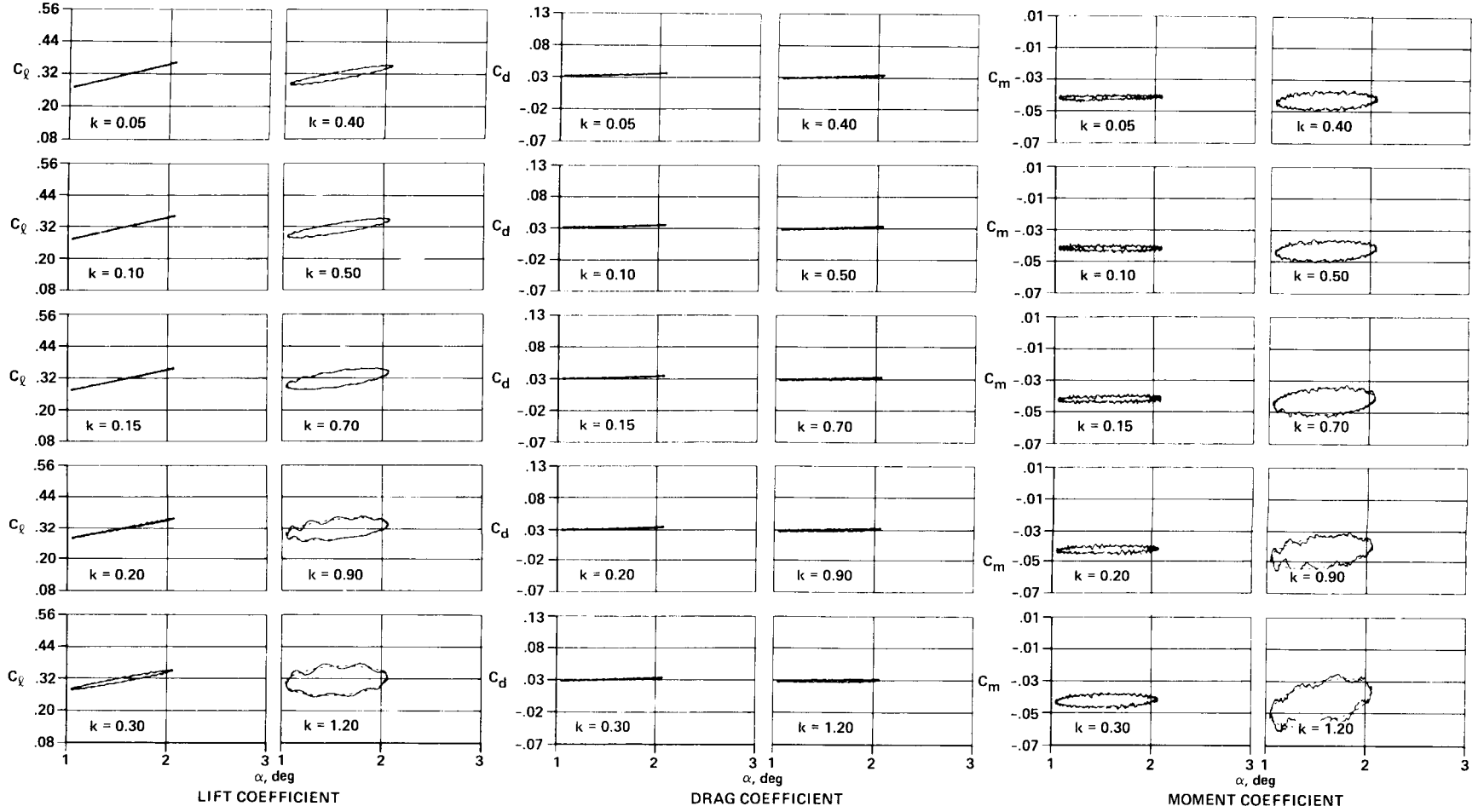

(b) $\alpha_0 = 1.5°$.

Figure 15.– Continued.

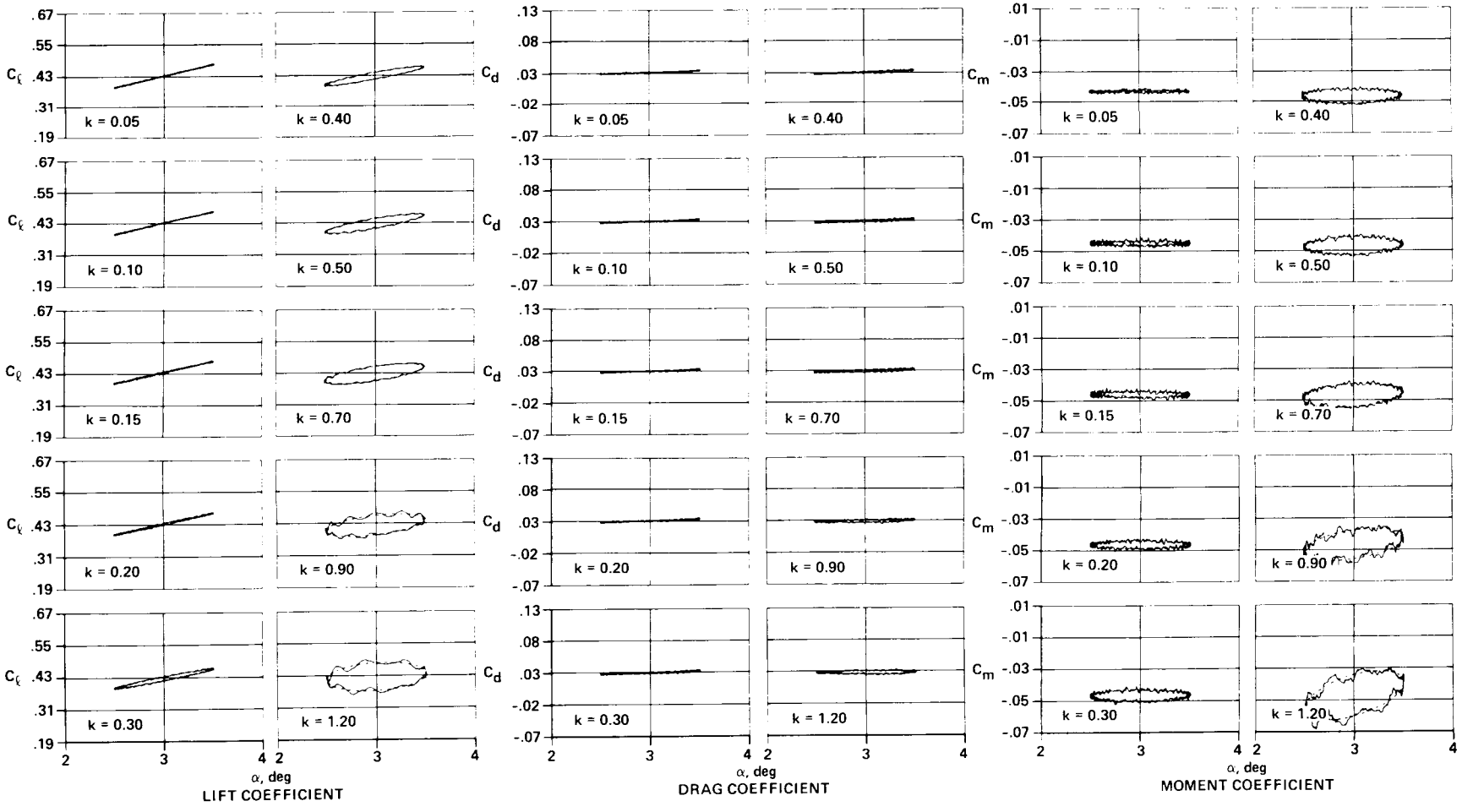

(c) $\alpha_0 = 3.0°$.

Figure 15.-- Continued.

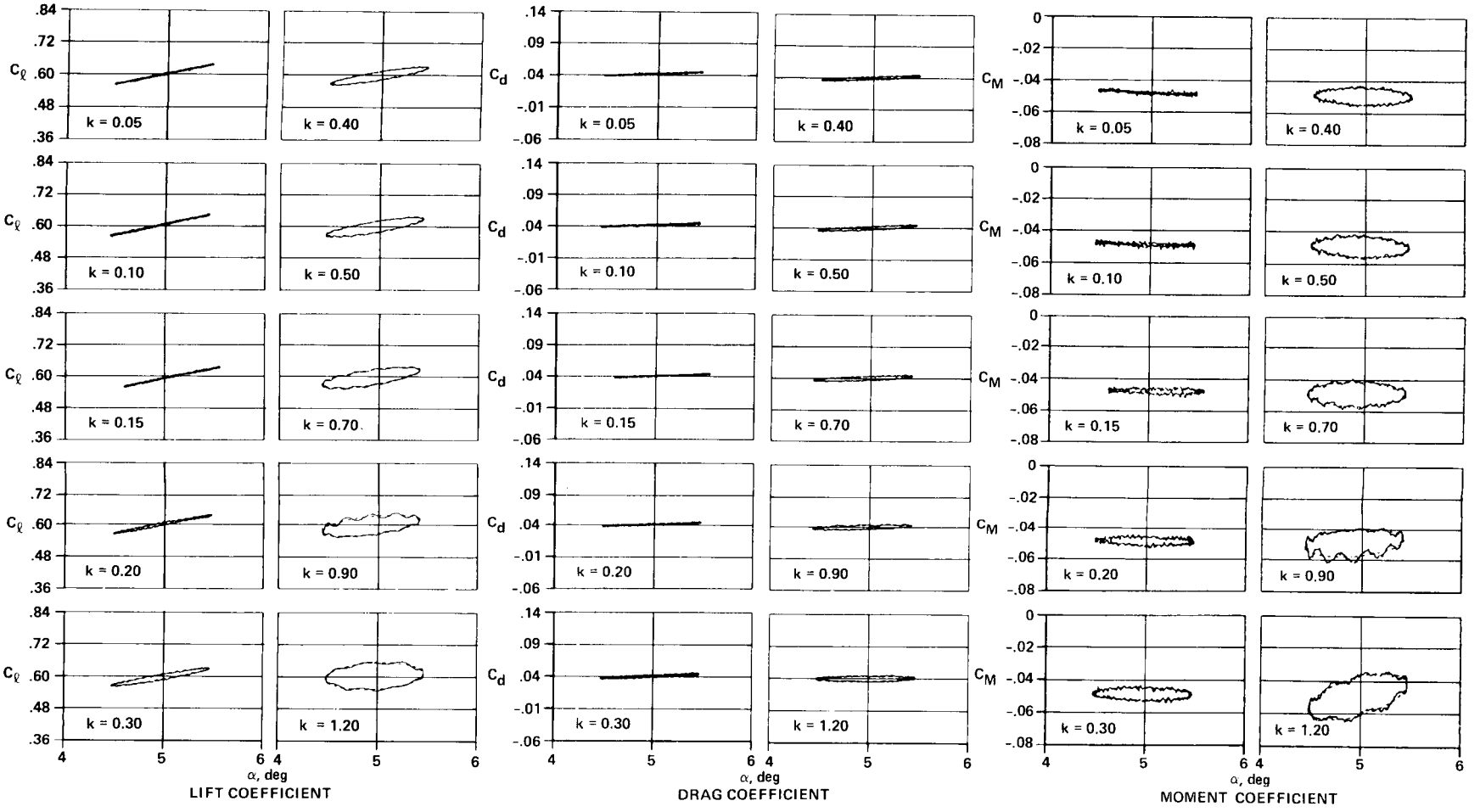

(d) $\alpha_0 = 5.0°$.

Figure 15.– Continued.

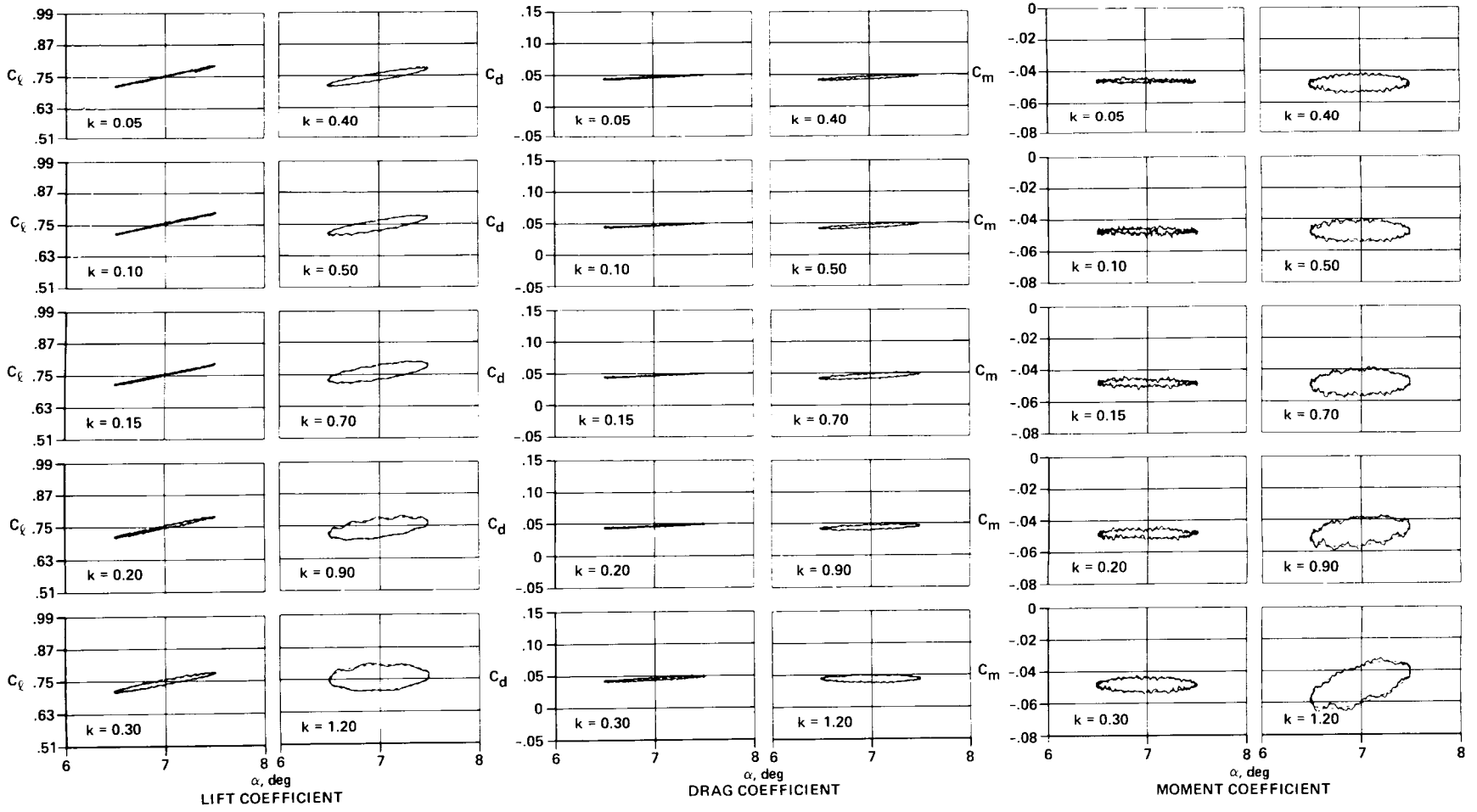

(e) $\alpha_0 = 7.0°$.

Figure 15.– Continued.

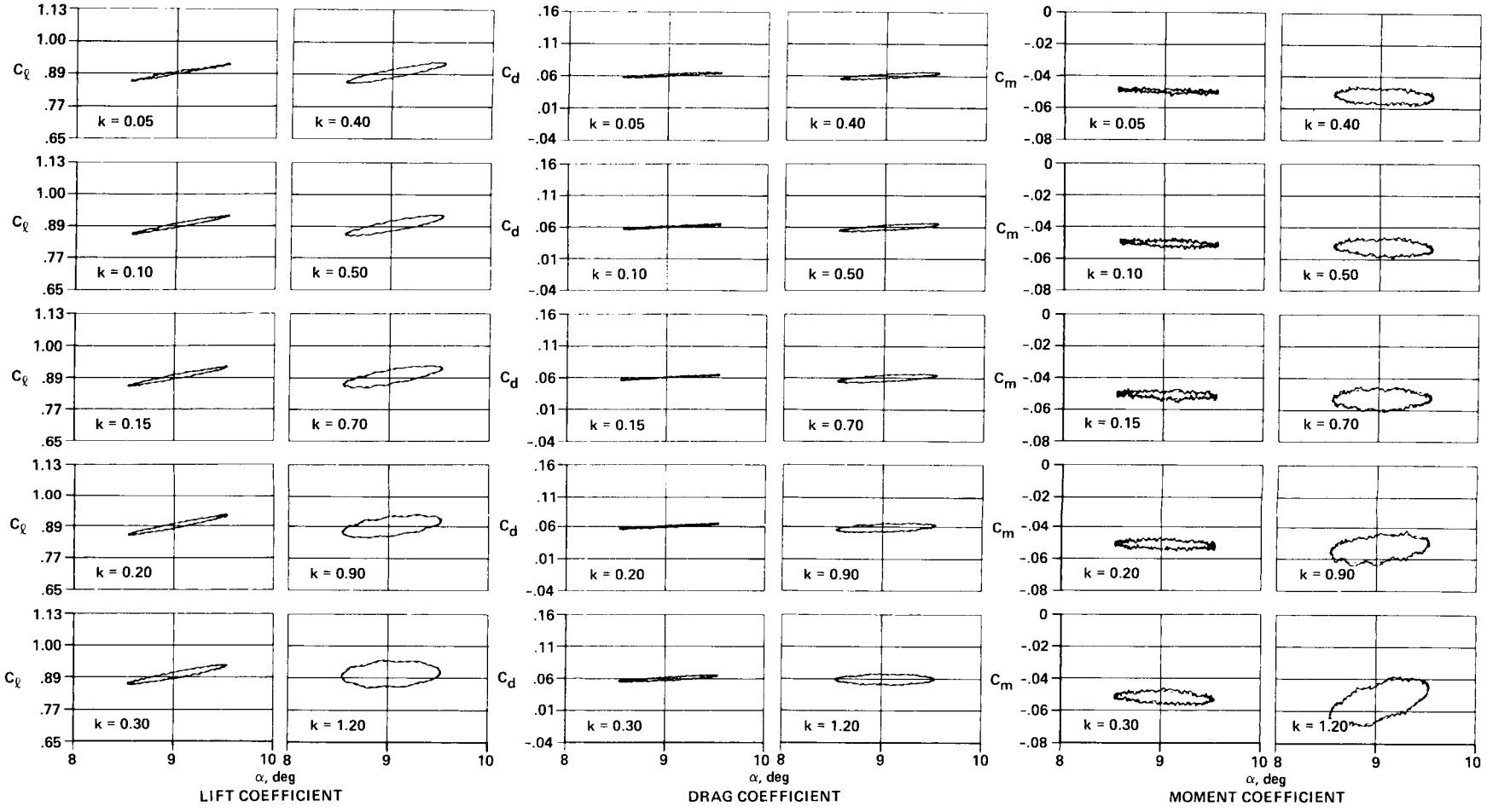

(f) $\alpha_0 = 9.0°$.

Figure 15.– Continued.

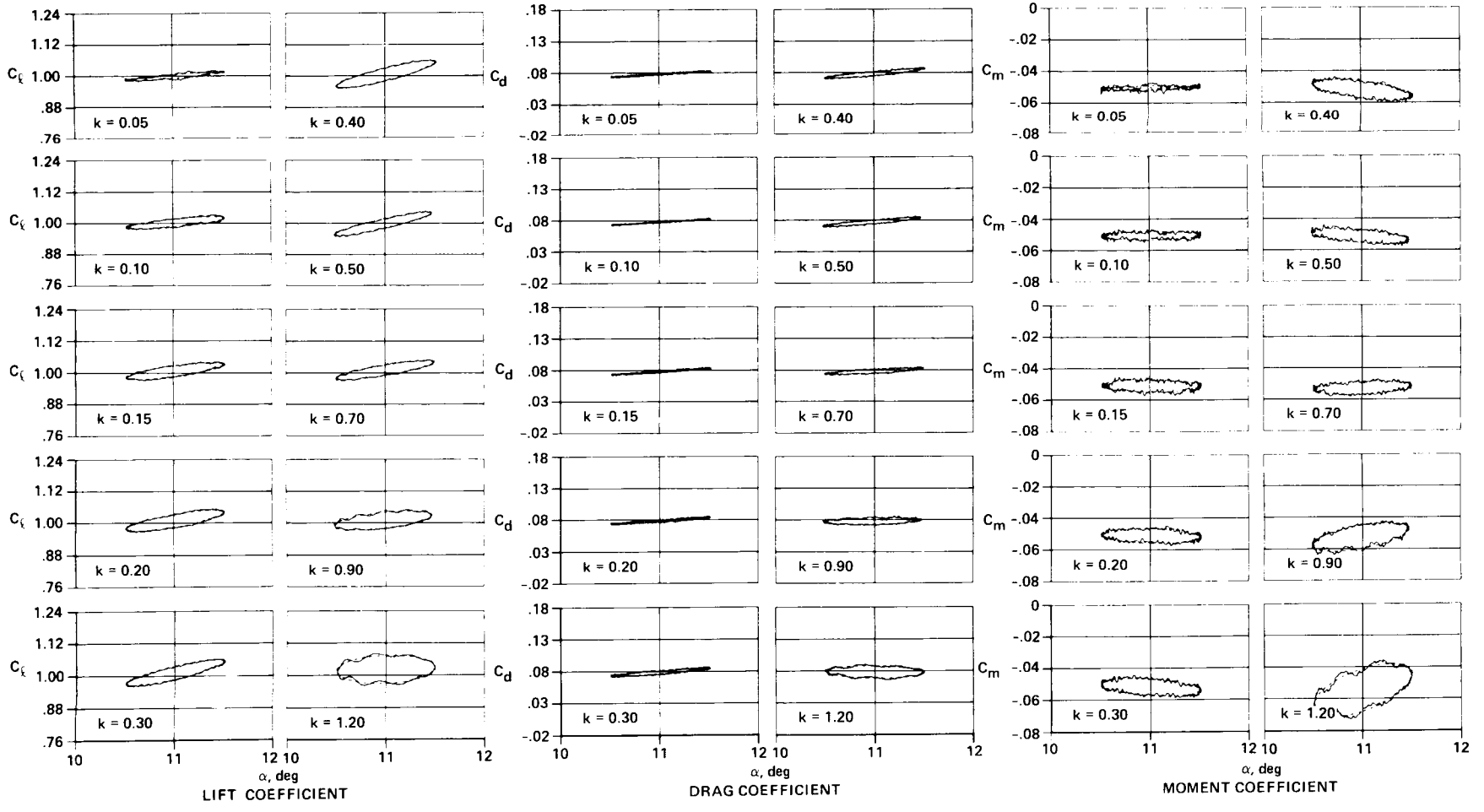

(g) $\alpha_0 = 11.0°$.

Figure 15.– Continued.

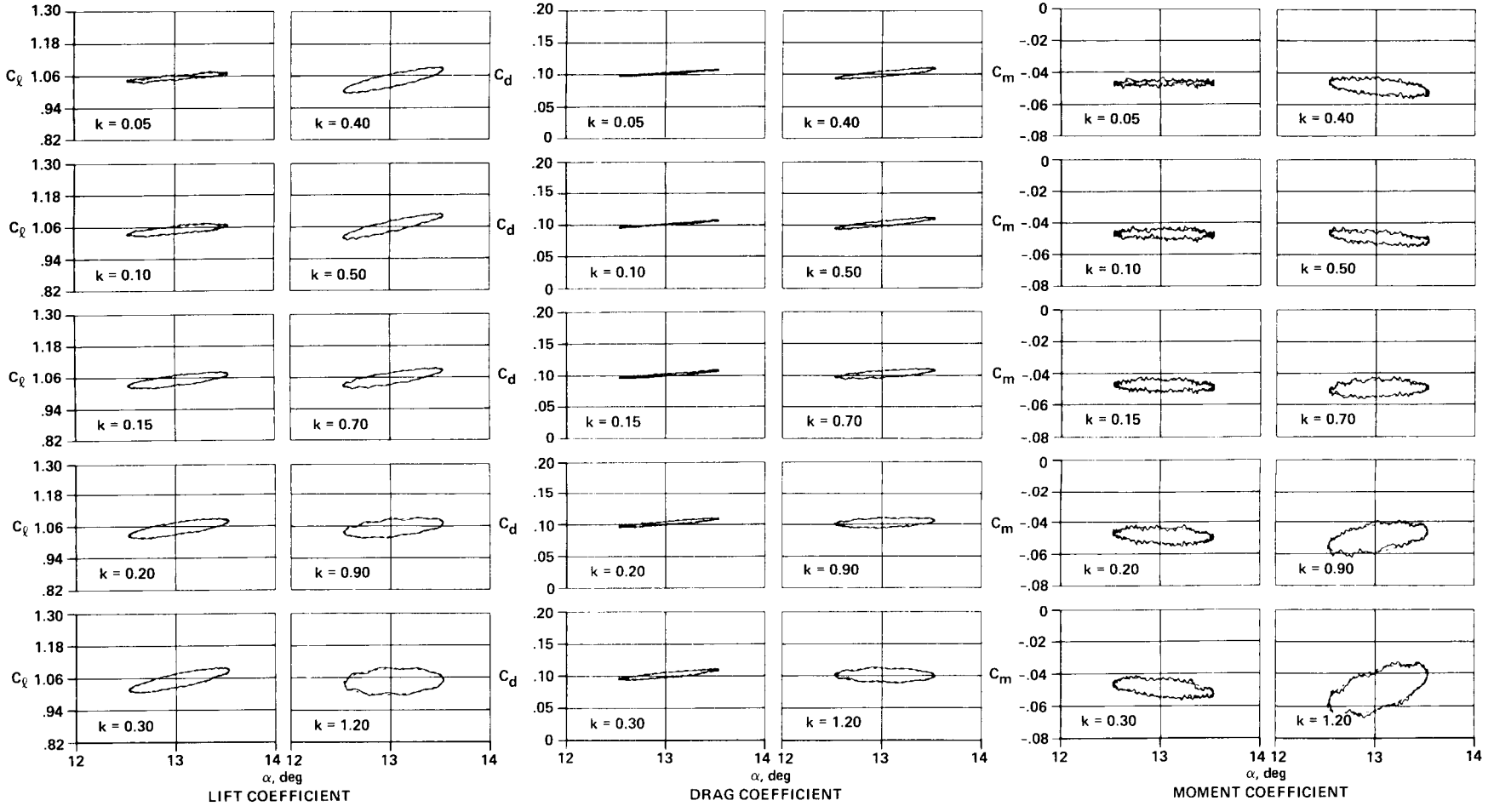

(h) $\alpha_0 = 13.0°$.

Figure 15.– Continued.

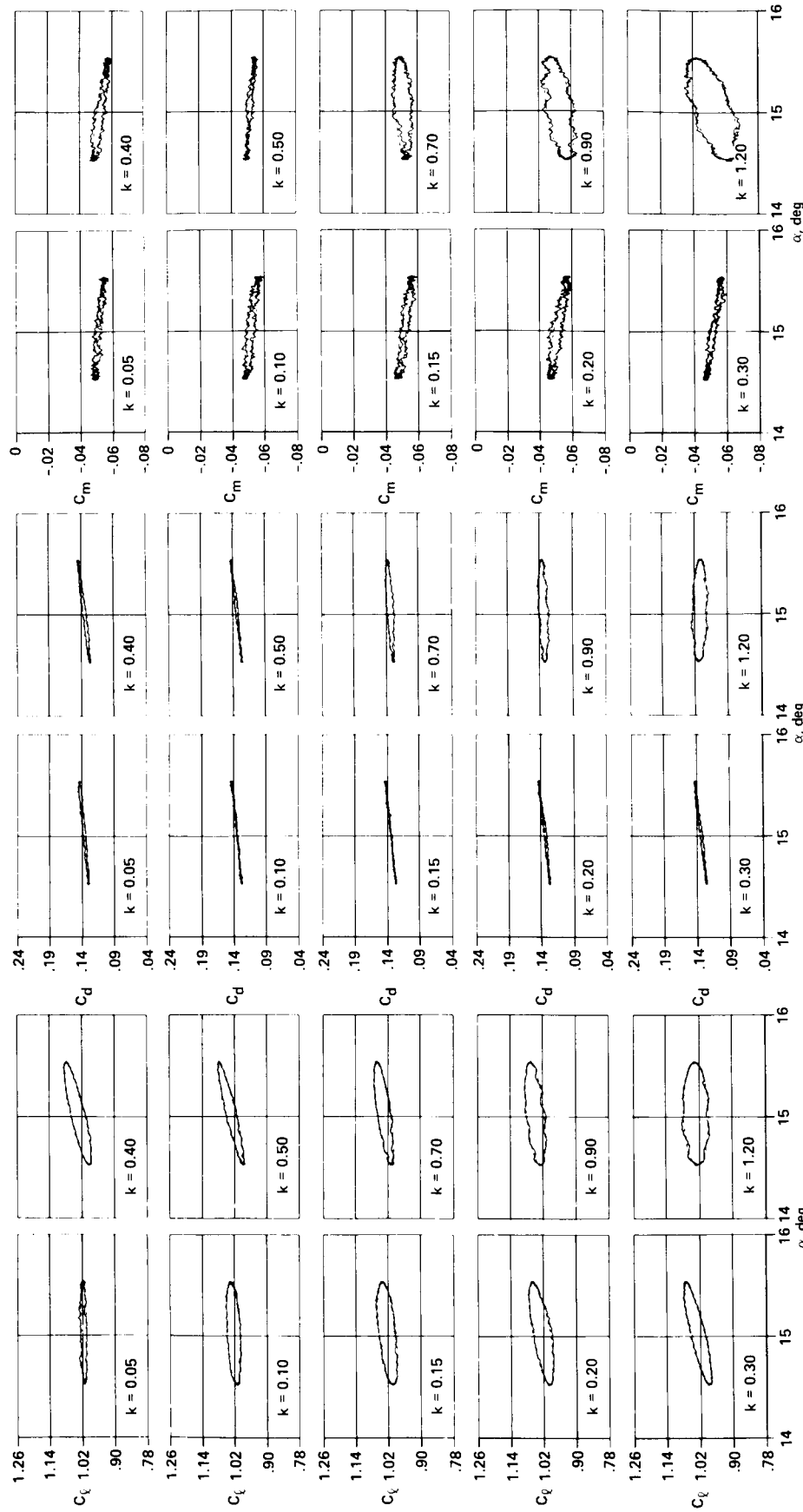

(i) $\alpha_0 = 15.0°$

Figure 15.– Continued.

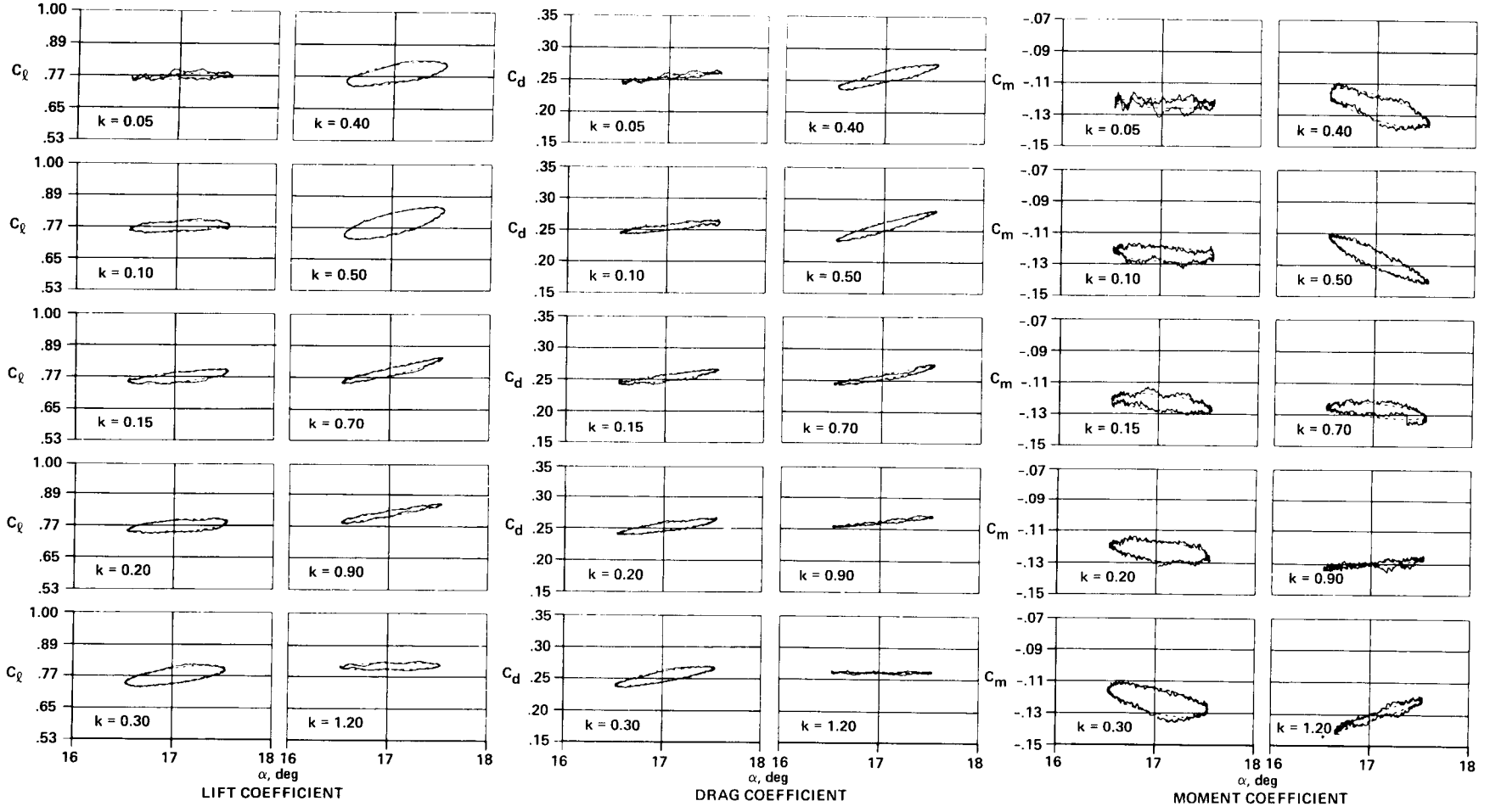

(j) $\alpha_0 = 17.0°$.

Figure 15.– Continued.

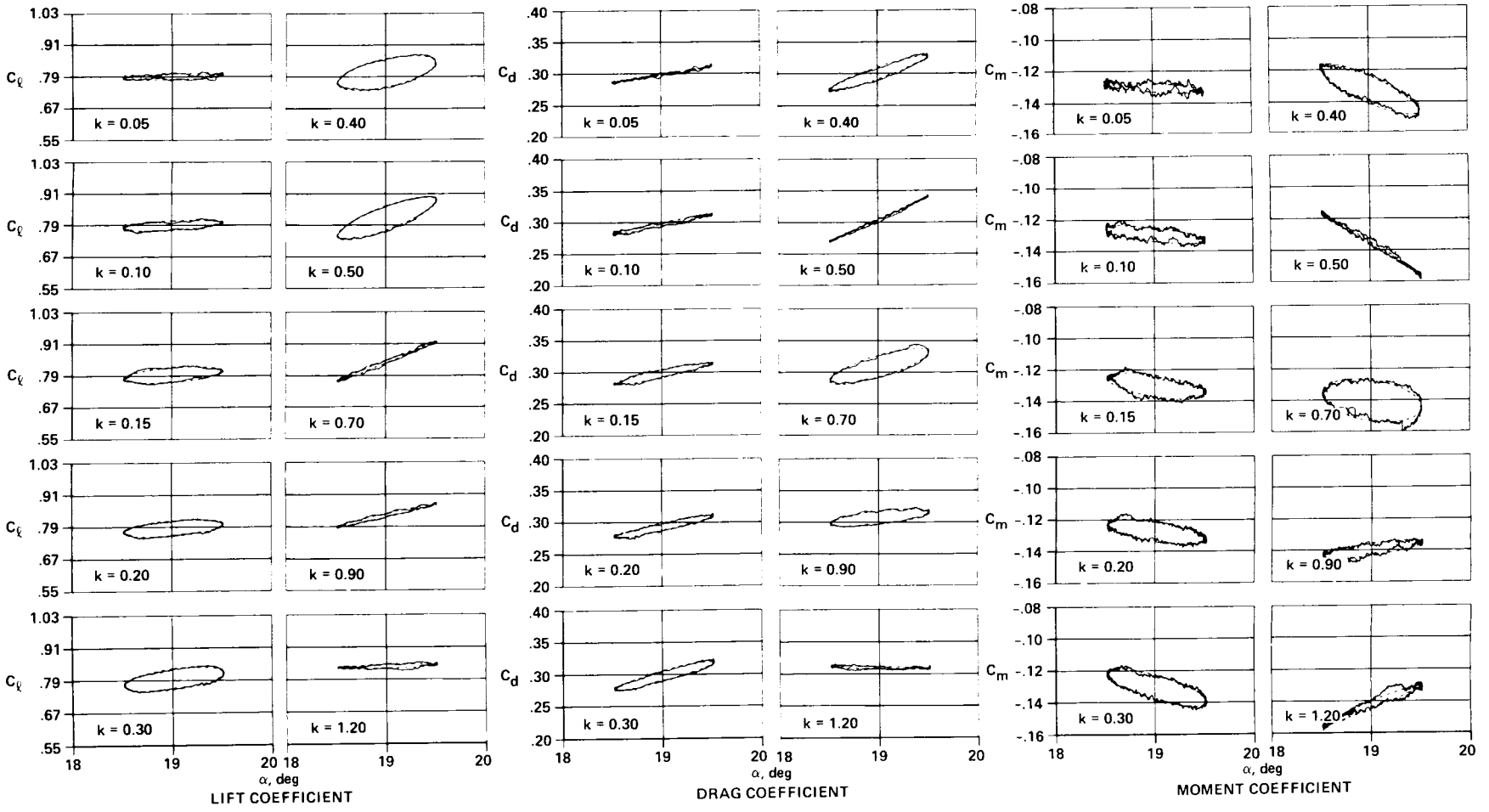

(k) $\alpha_0 = 19.0°$.

Figure 15.– Continued.

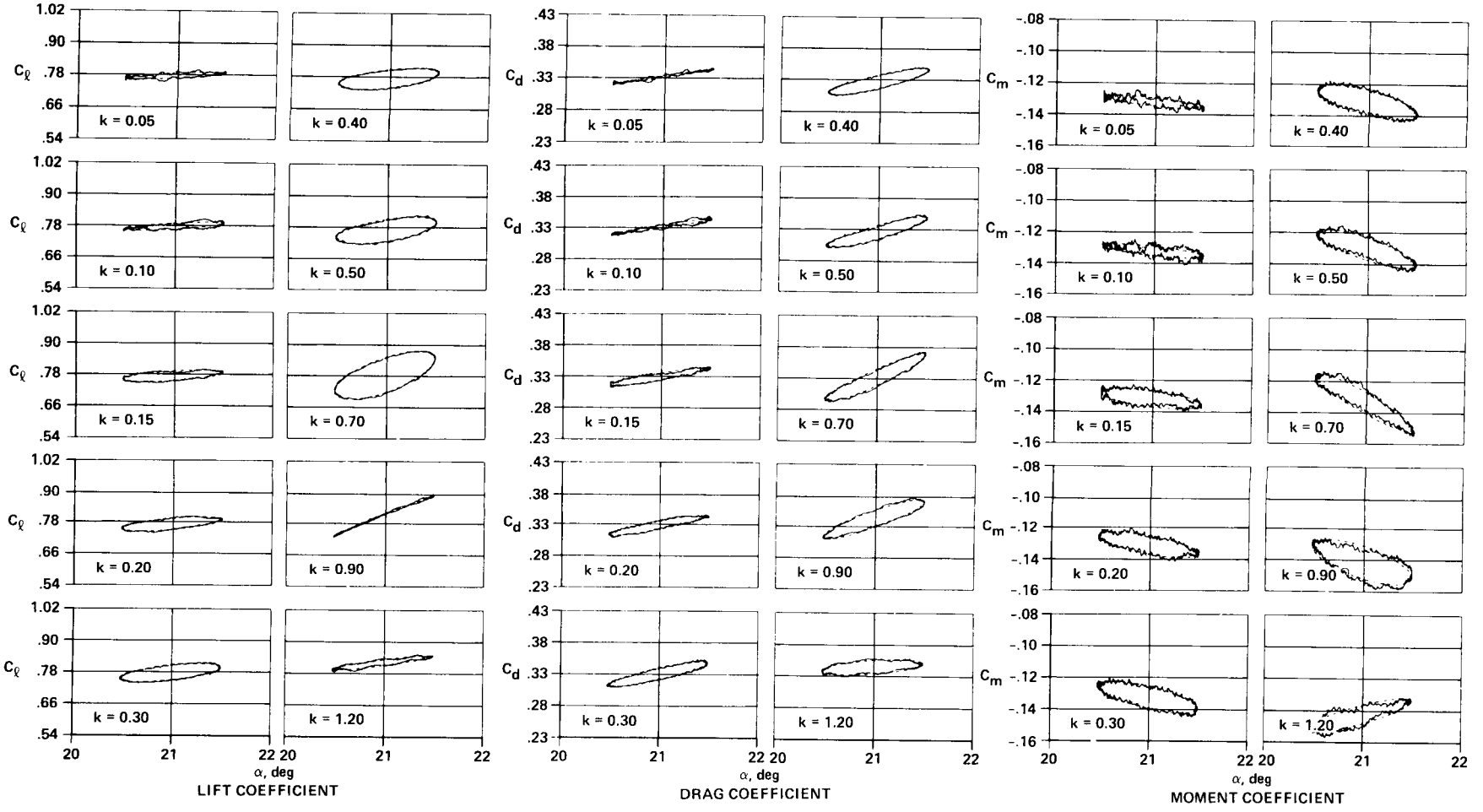

(l) $\alpha_0 = 21.0°$.

Figure 15.– Continued.

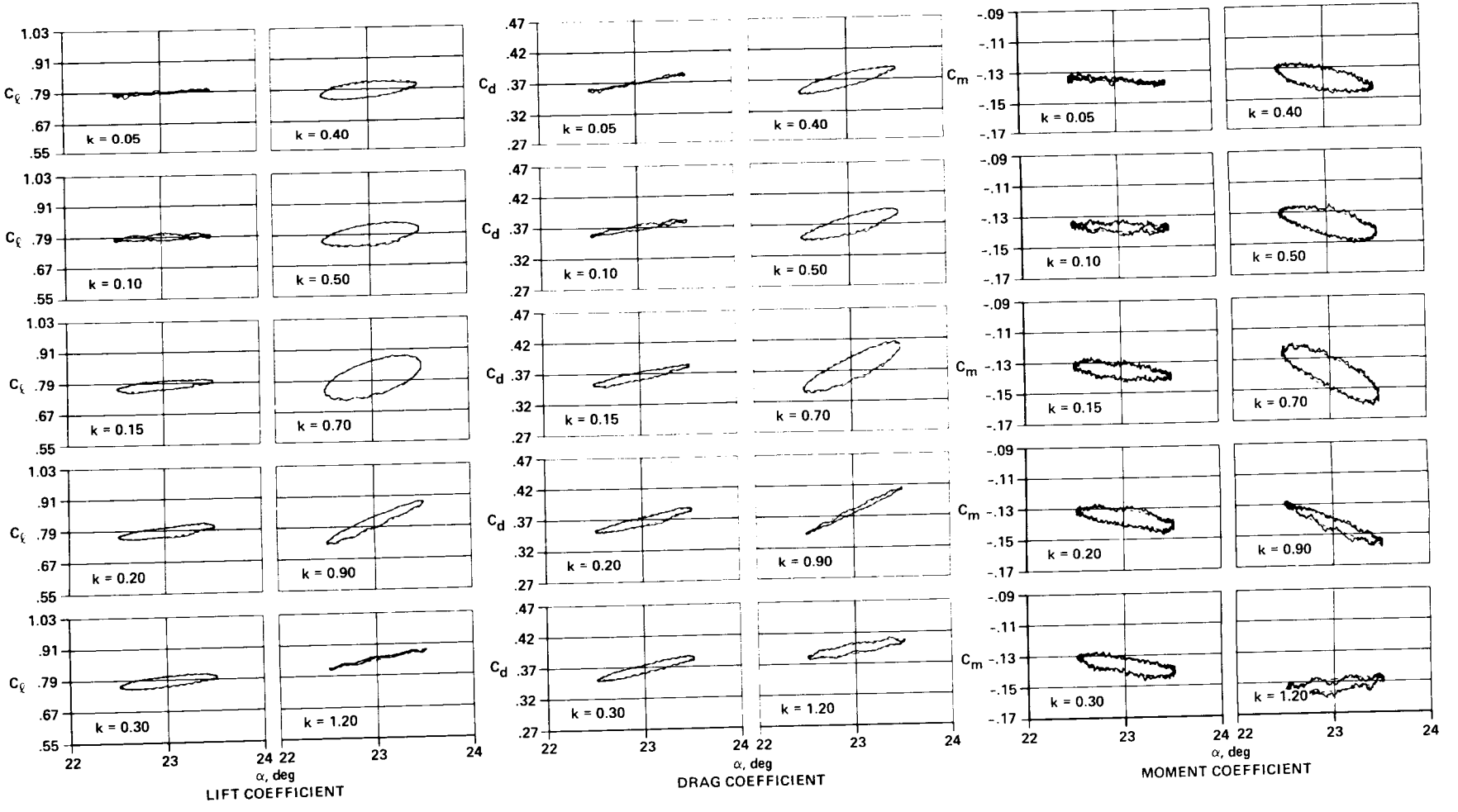

(m) $\alpha_0 = 23.0°$.

Figure 15.– Concluded.

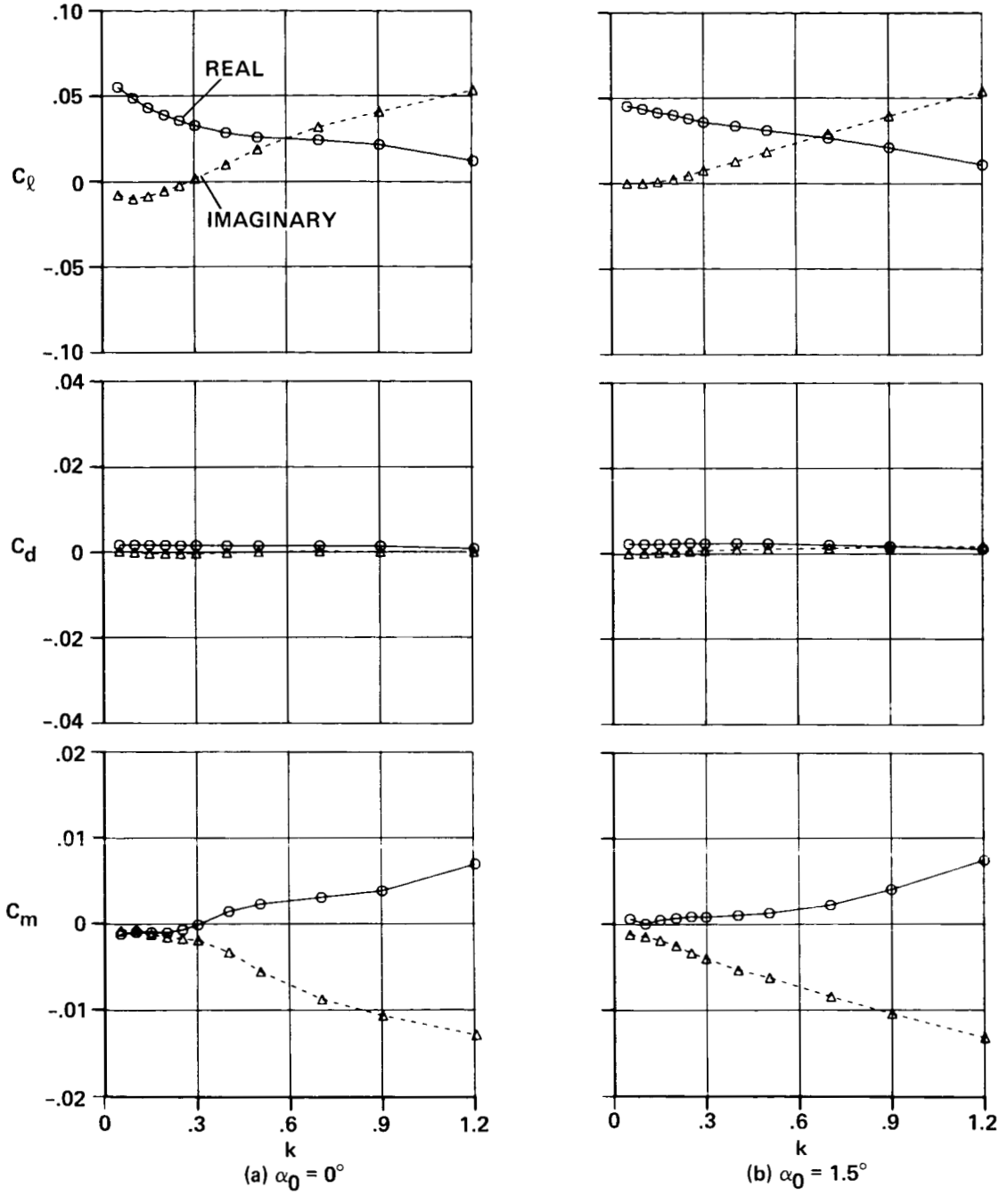

Figure 16.– Variation of the real and imaginary load components with mean angle and reduced frequency.

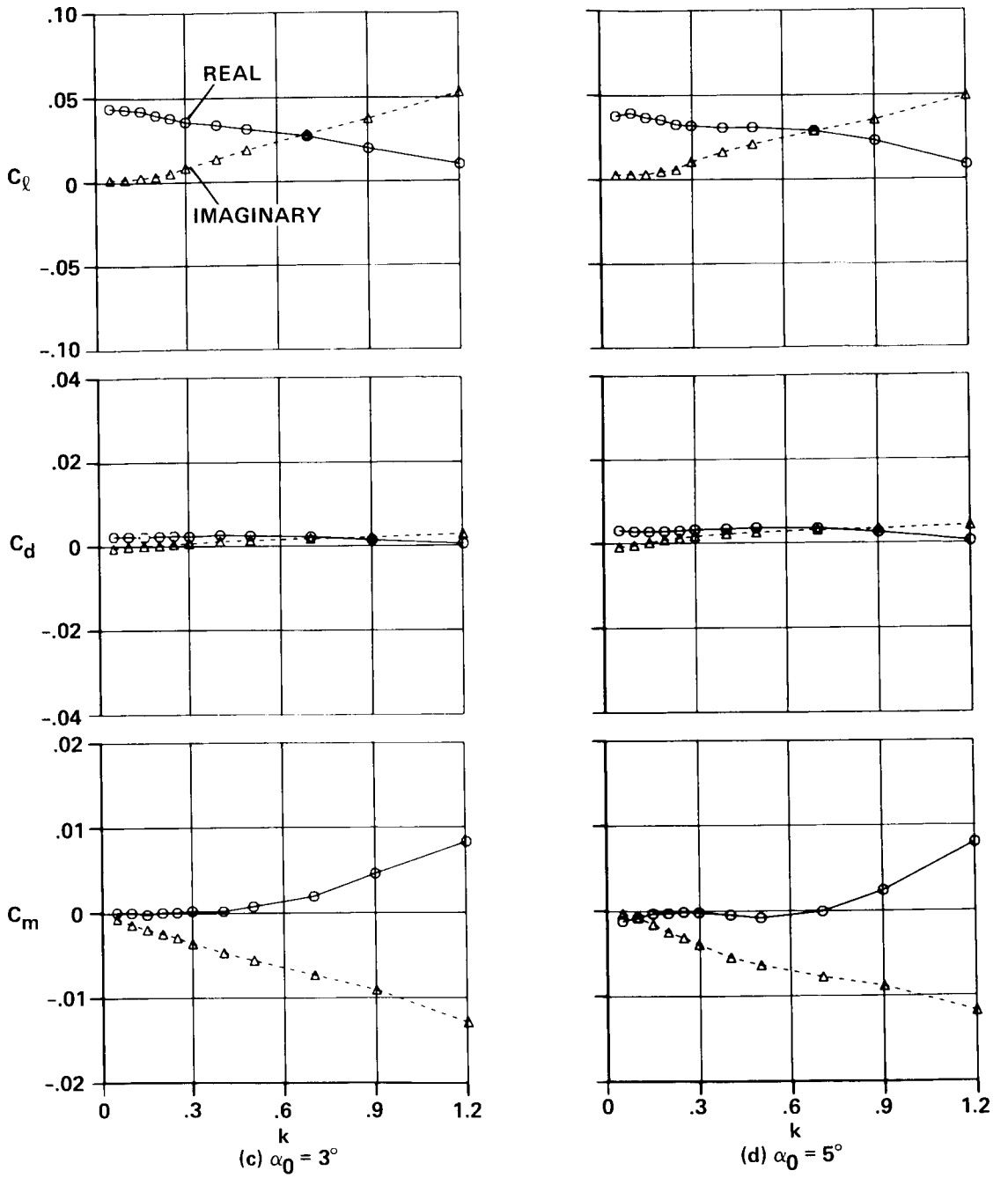

Figure 16.– Continued.

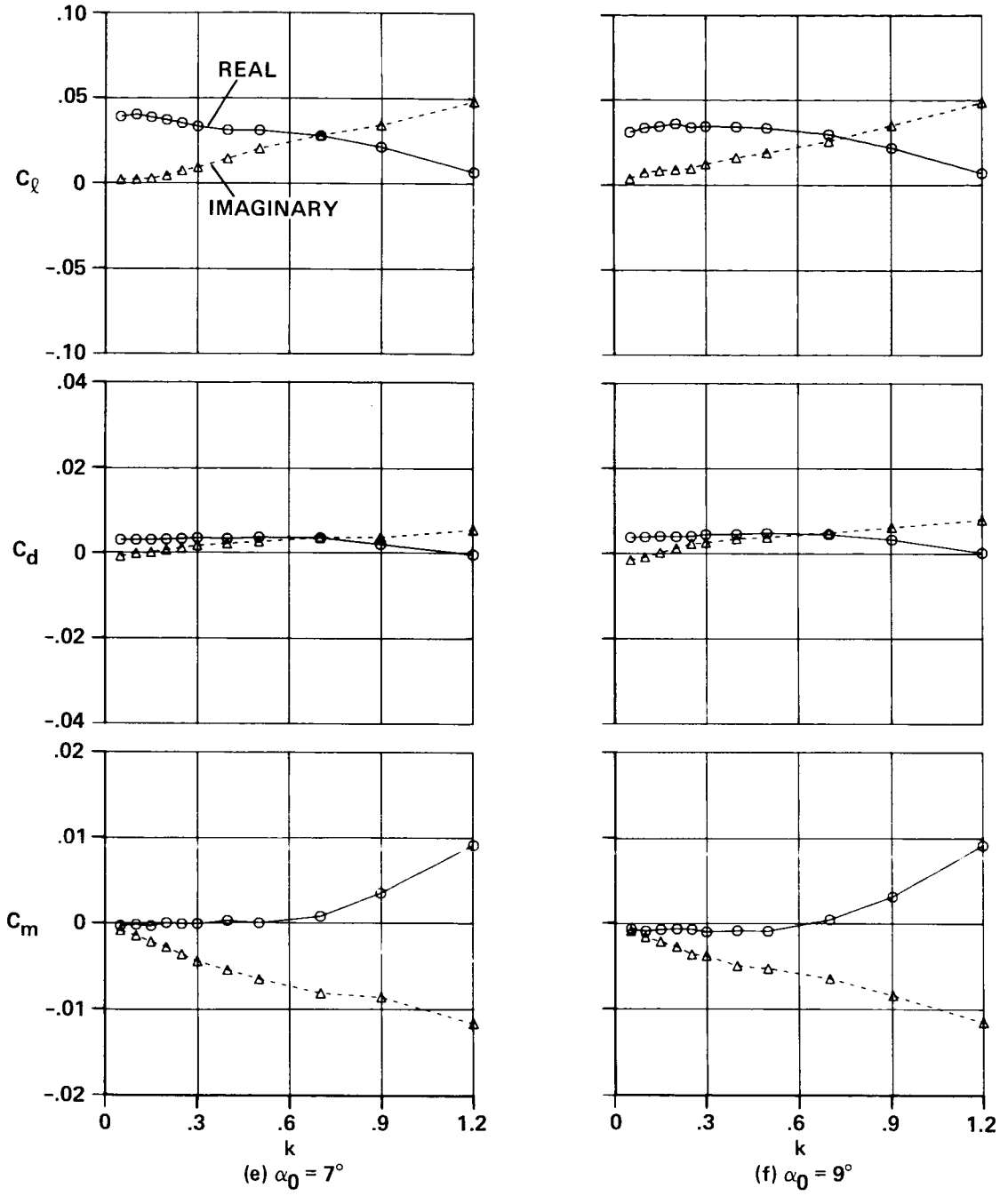

Figure 16.– Continued.

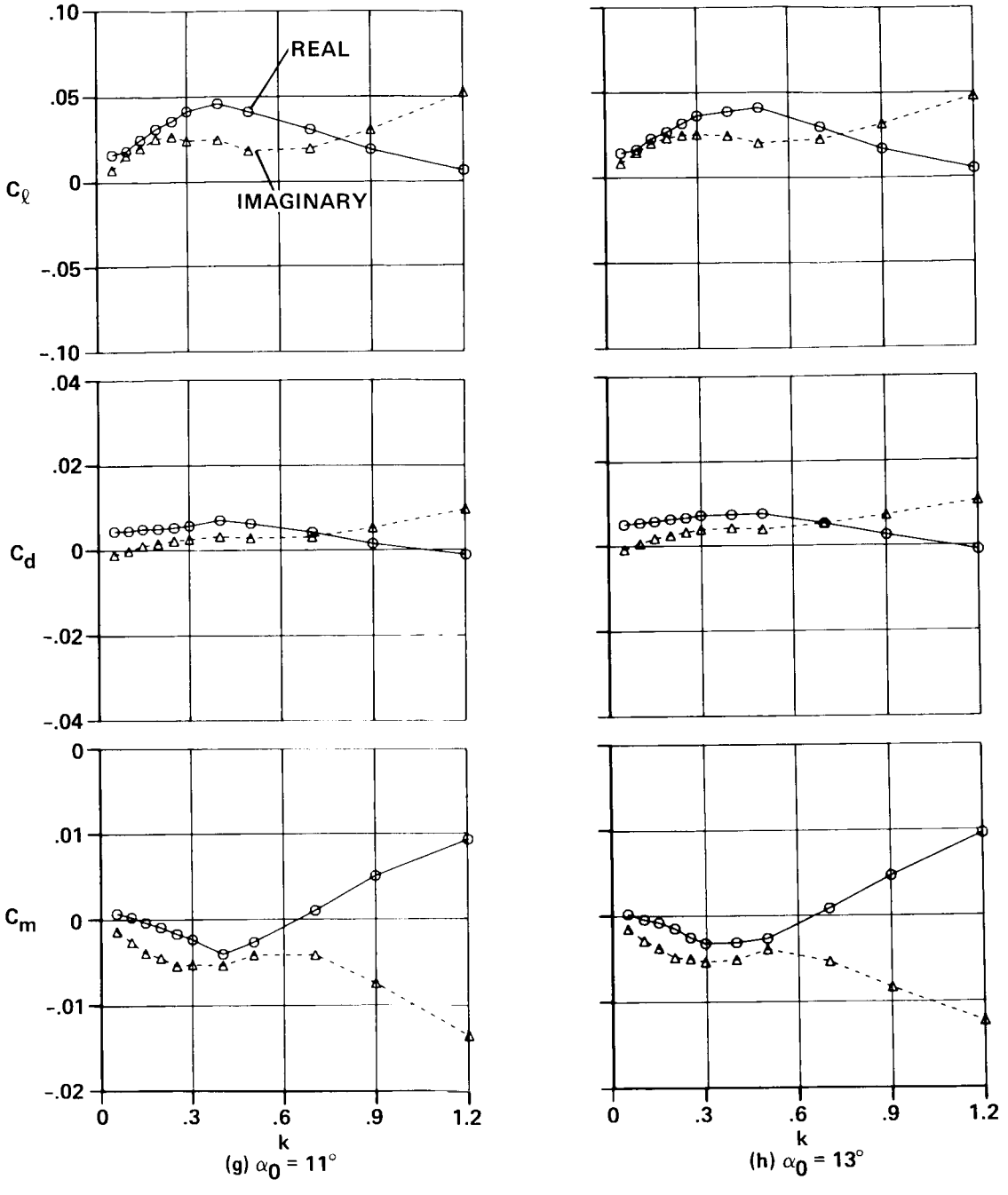

Figure 16.– Continued.

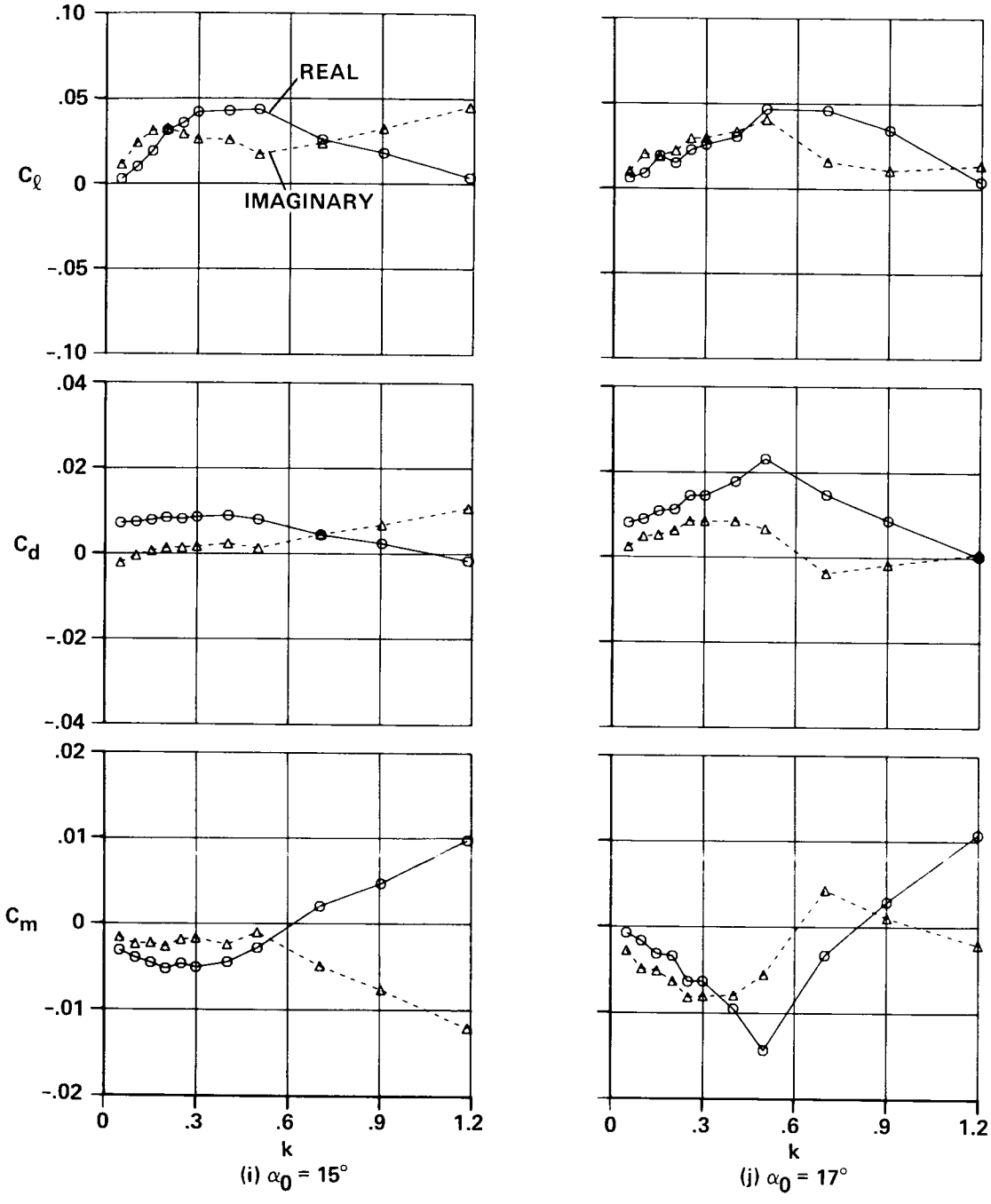

Figure 16.– Continued.

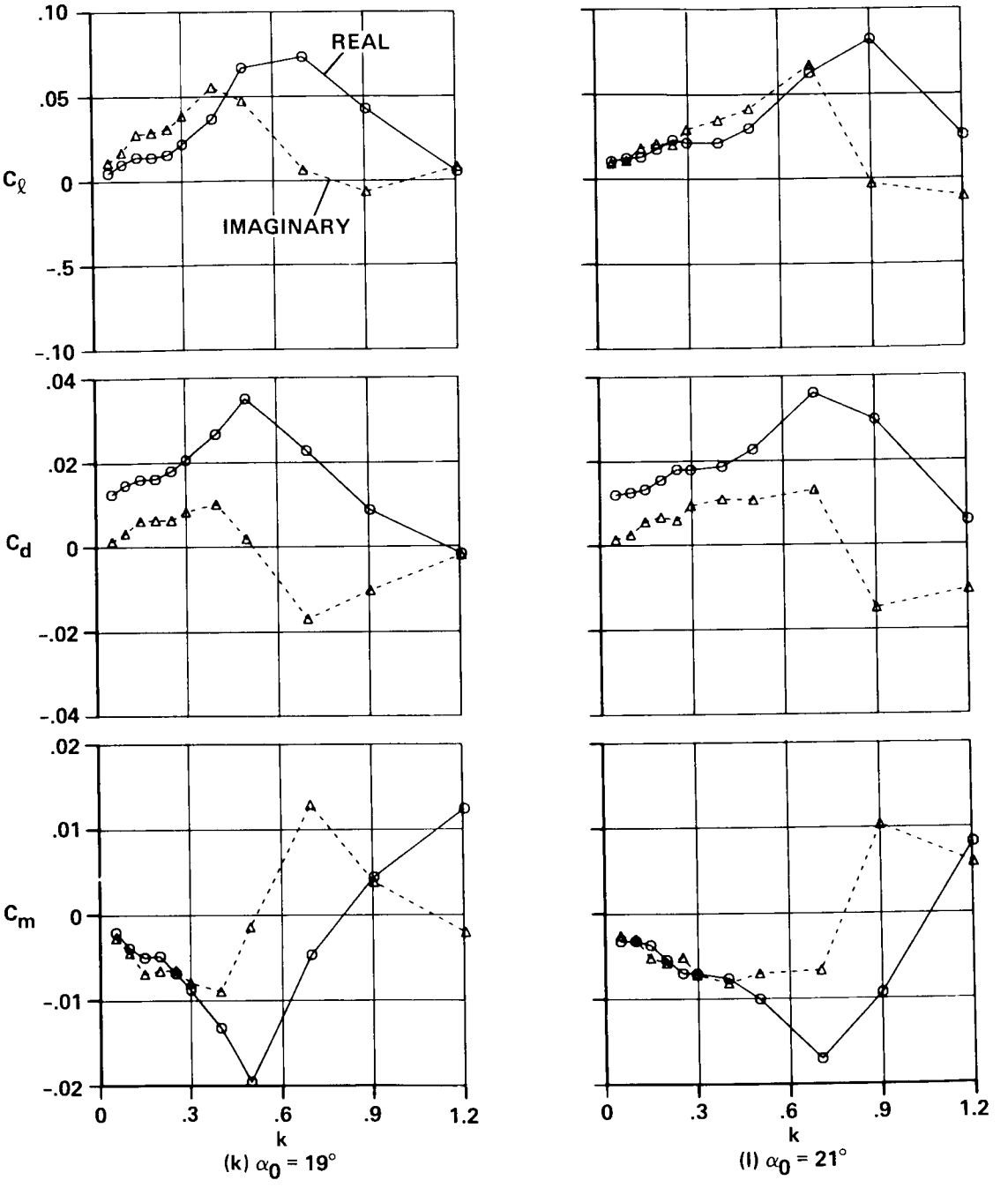

Figure 16.– Continued.

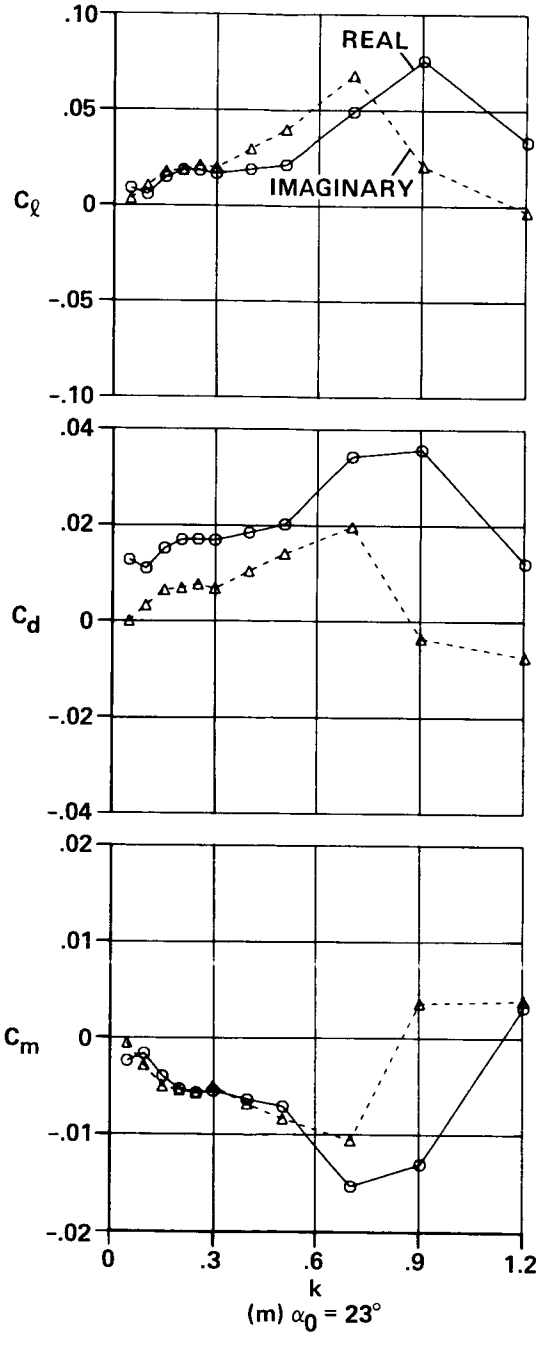

Figure 16.– Concluded.

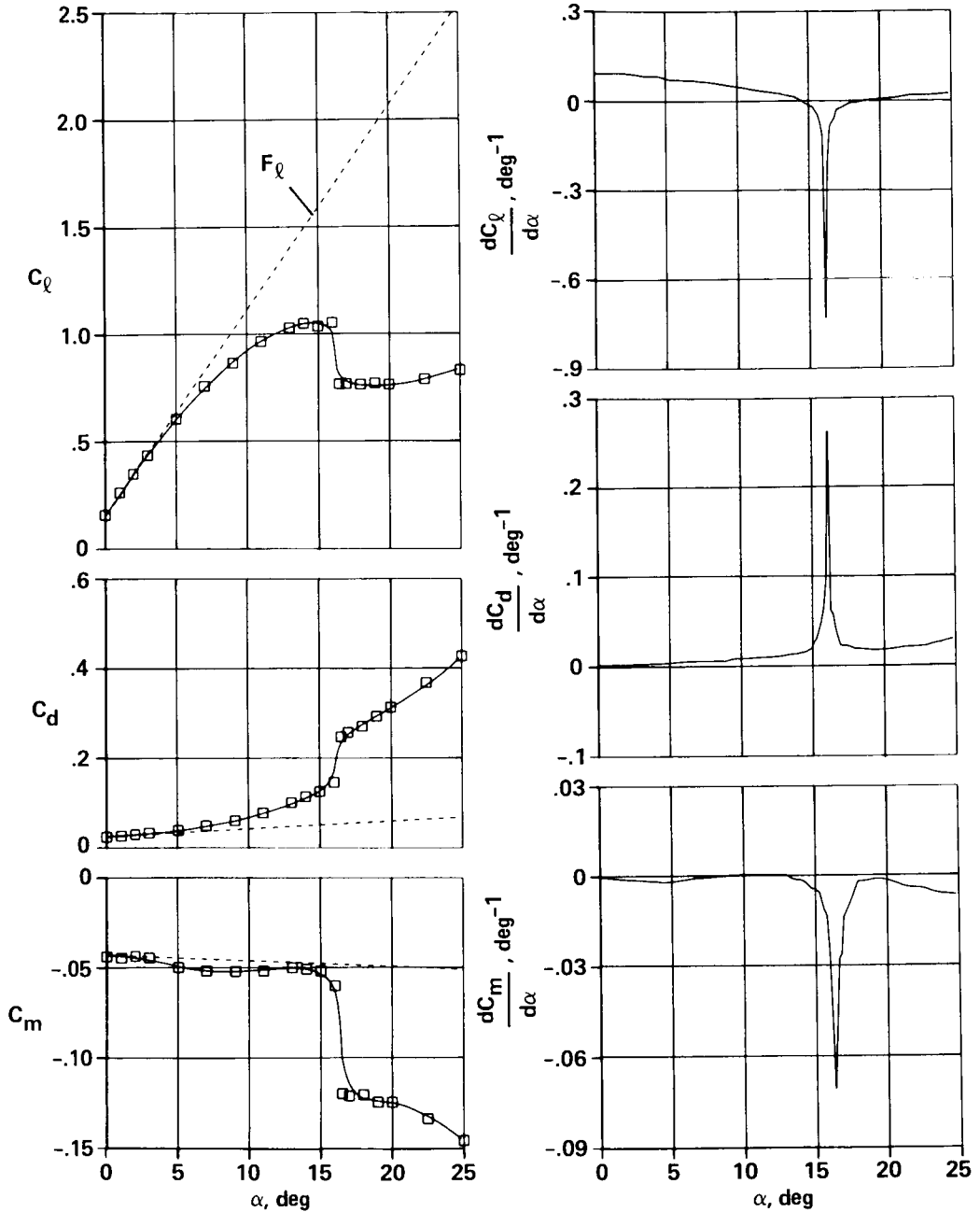

Figure 17.– Static load variation with incidence.

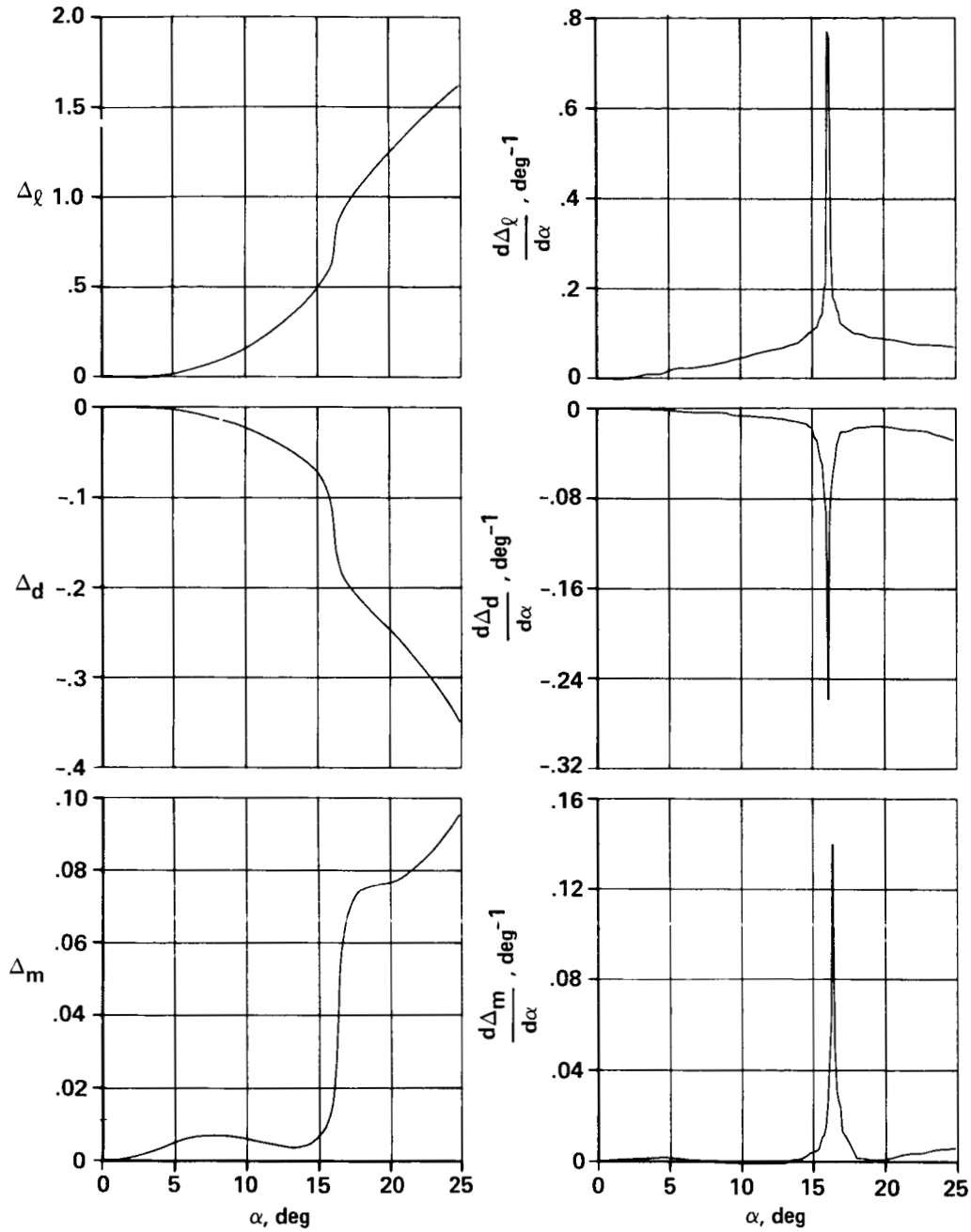

Figure 18.– Deviation between the linear and static curves.

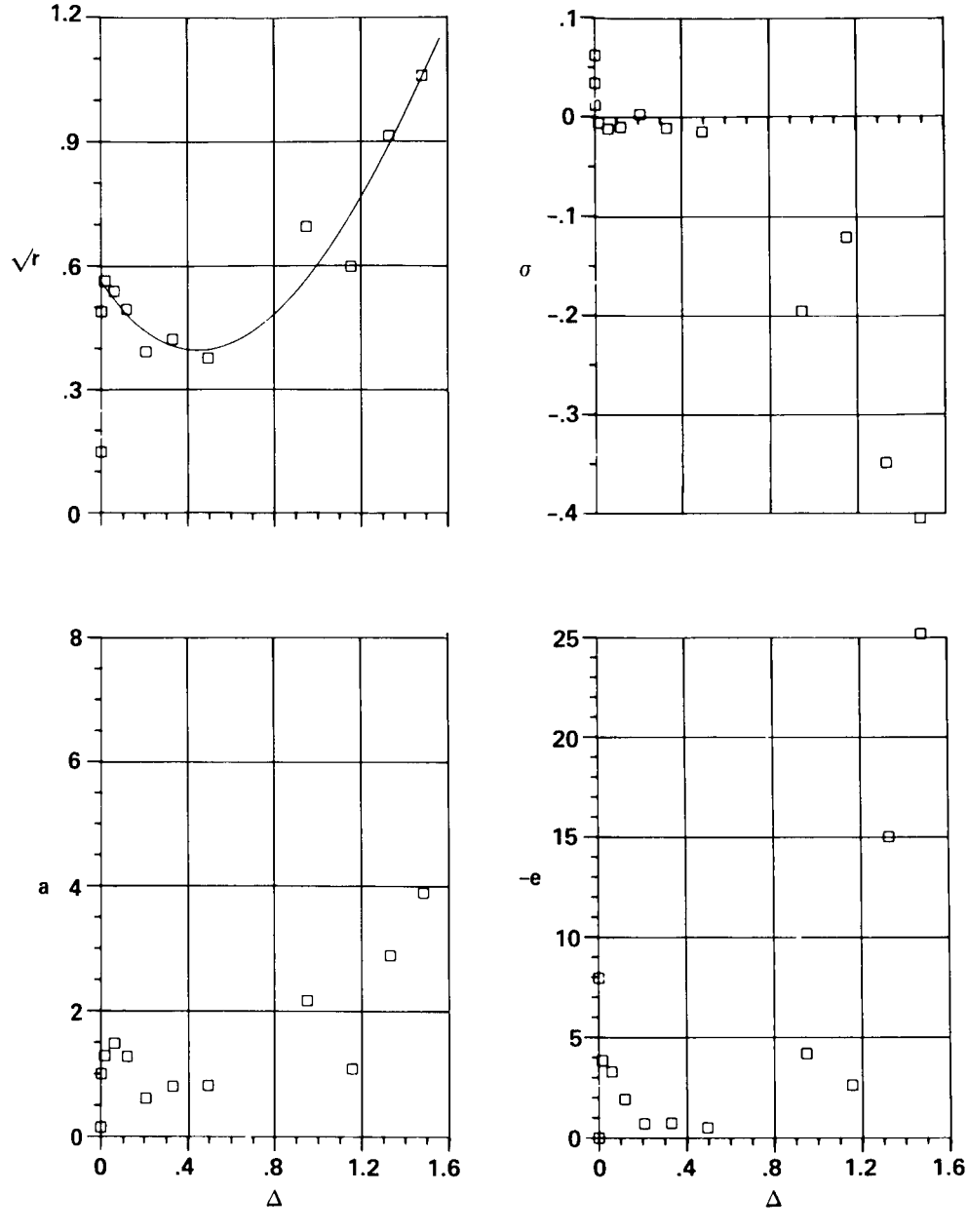

Figure 19.– Optimization of real and imaginary lift responses with four unknown coefficients.

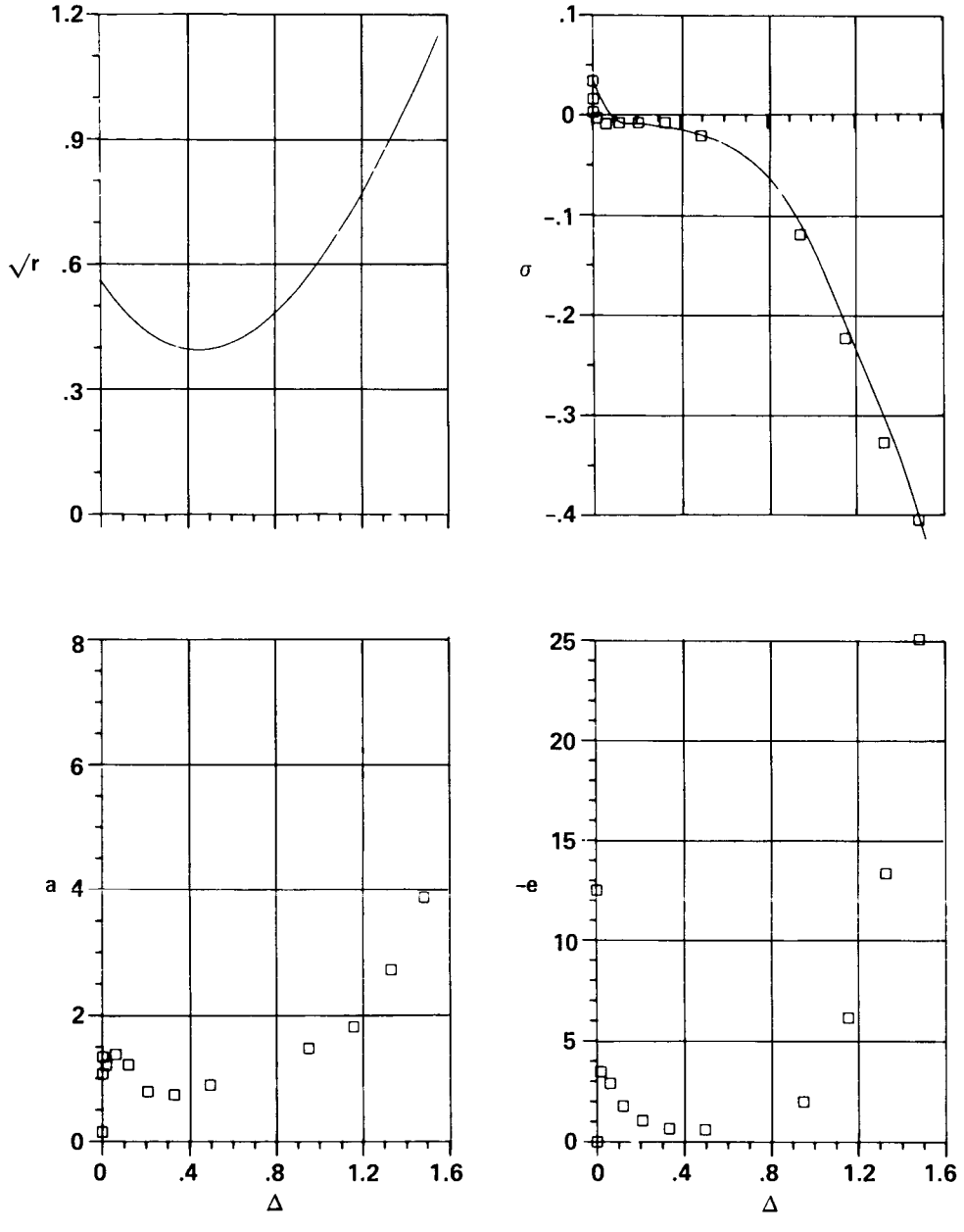

Figure 20.– Optimization of real and imaginary lift responses with three unknown coefficients.

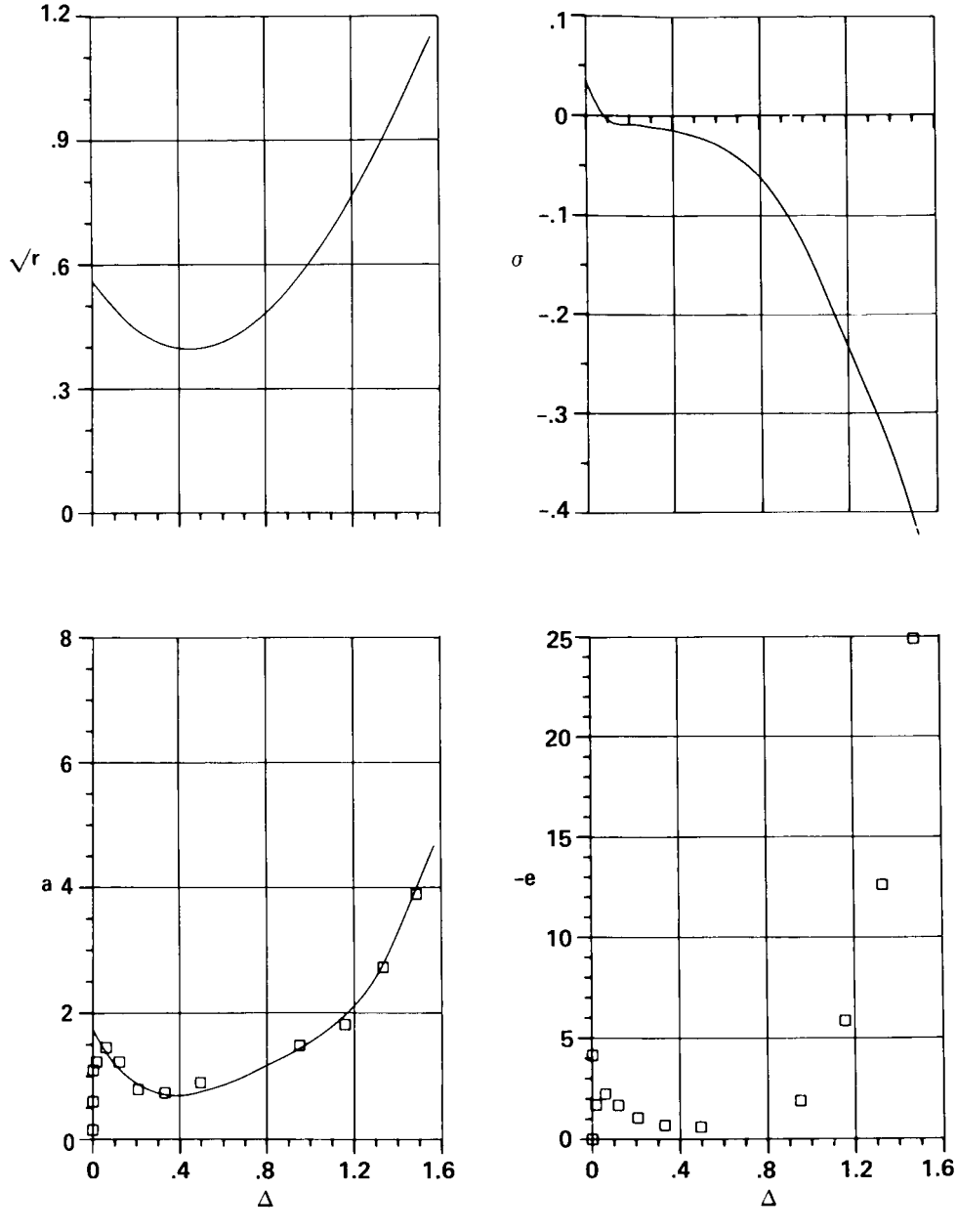

Figure 21.– Optimization of real and imaginary lift responses with two unknown coefficients.

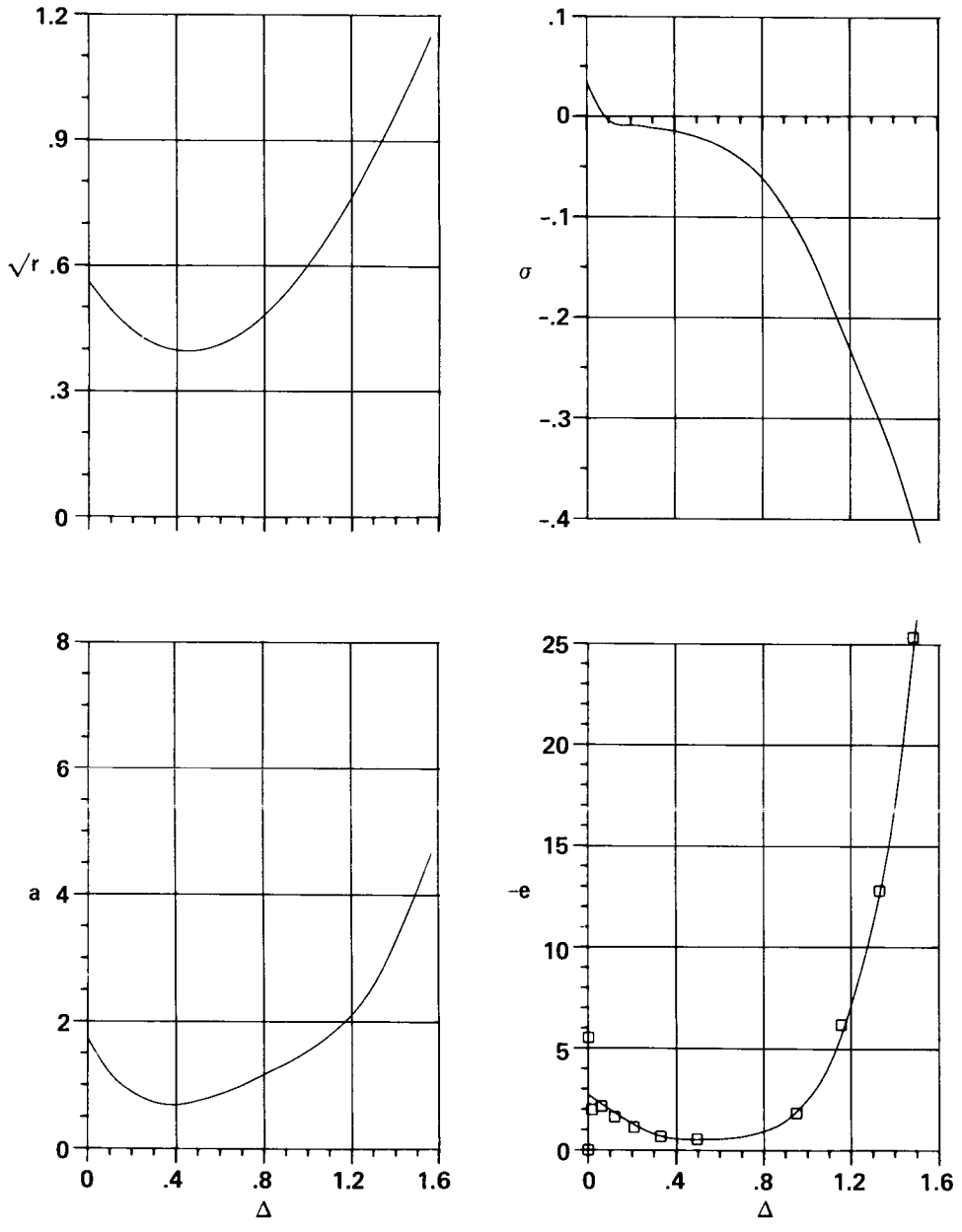

Figure 22.– Optimization of real and imaginary lift responses with one unknown coefficient.

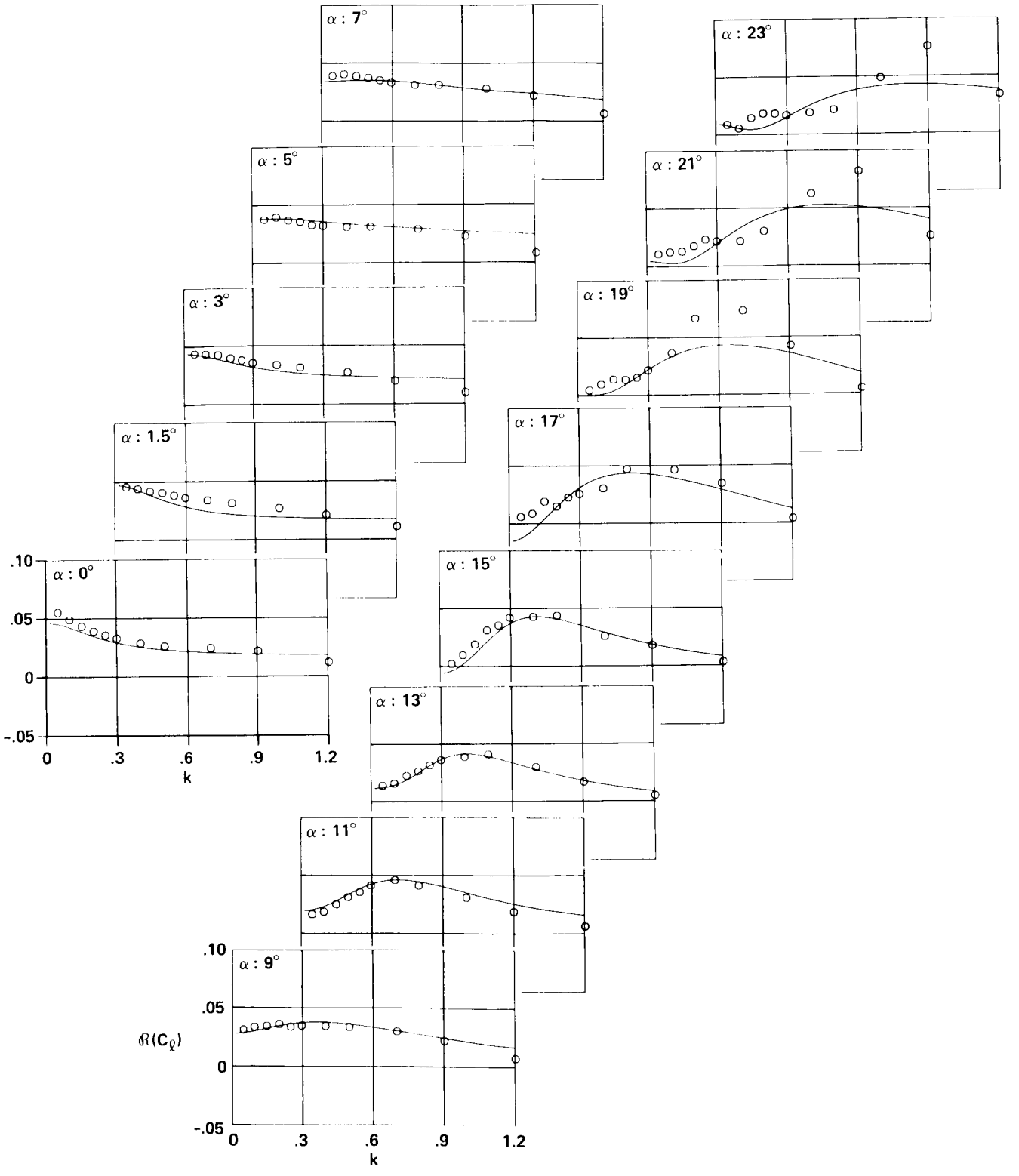

Figure 23.– Calculated and measured values for the real part of the lift coefficient.

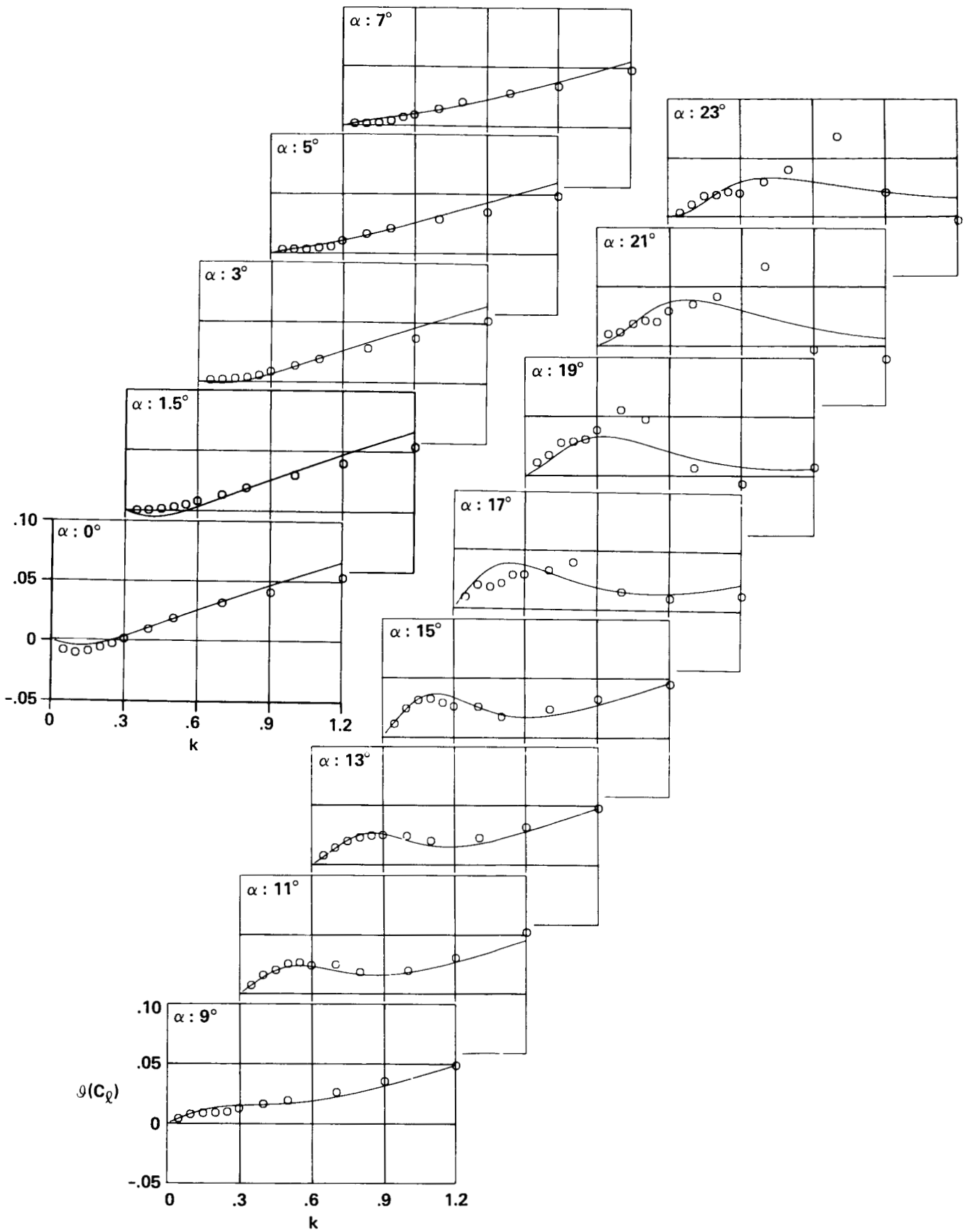

Figure 24.– Calculated and measured values for the imaginary part of the lift coefficient.

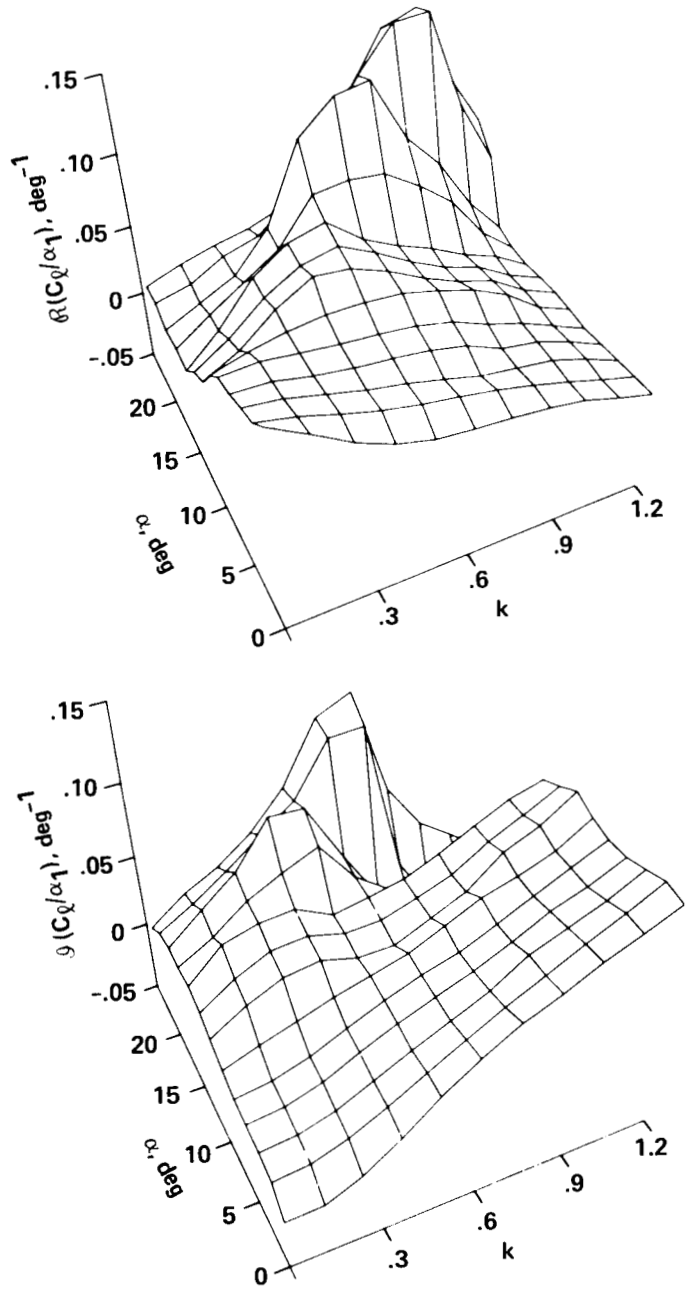

Figure 25.– Measured values of the real and imaginary parts of the lift coefficient.

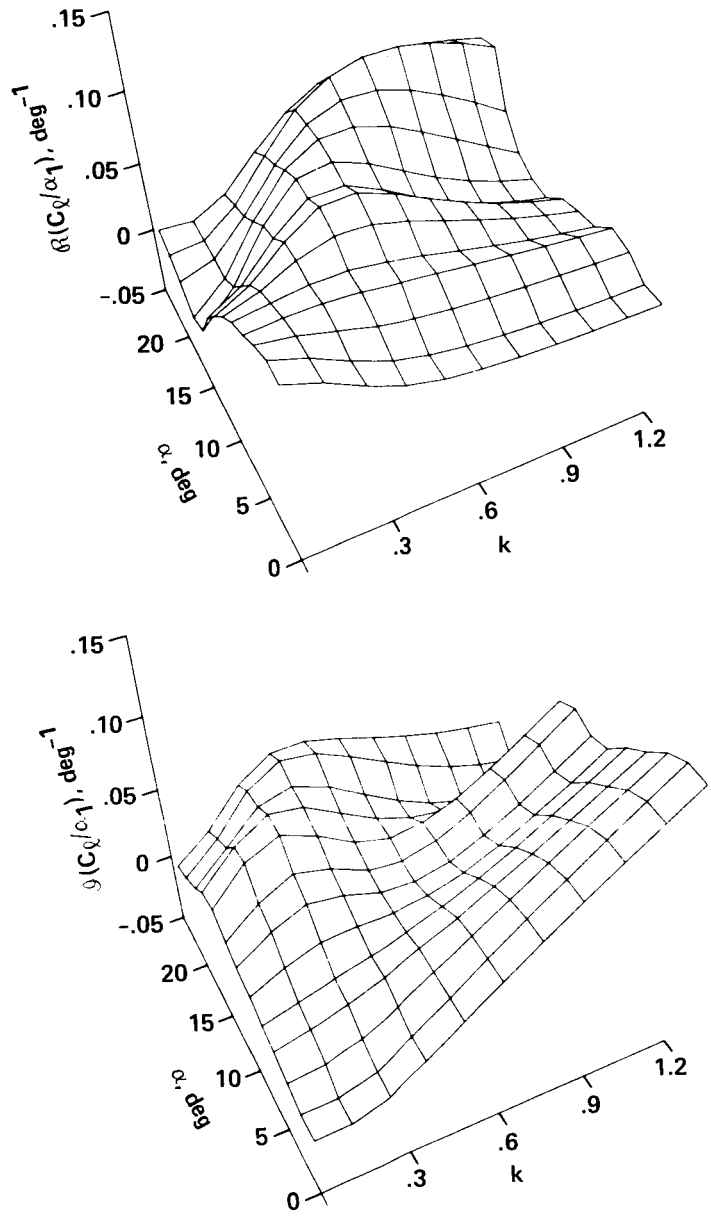

Figure 26.– Calculated values of the real and imaginary parts of the lift coefficient.

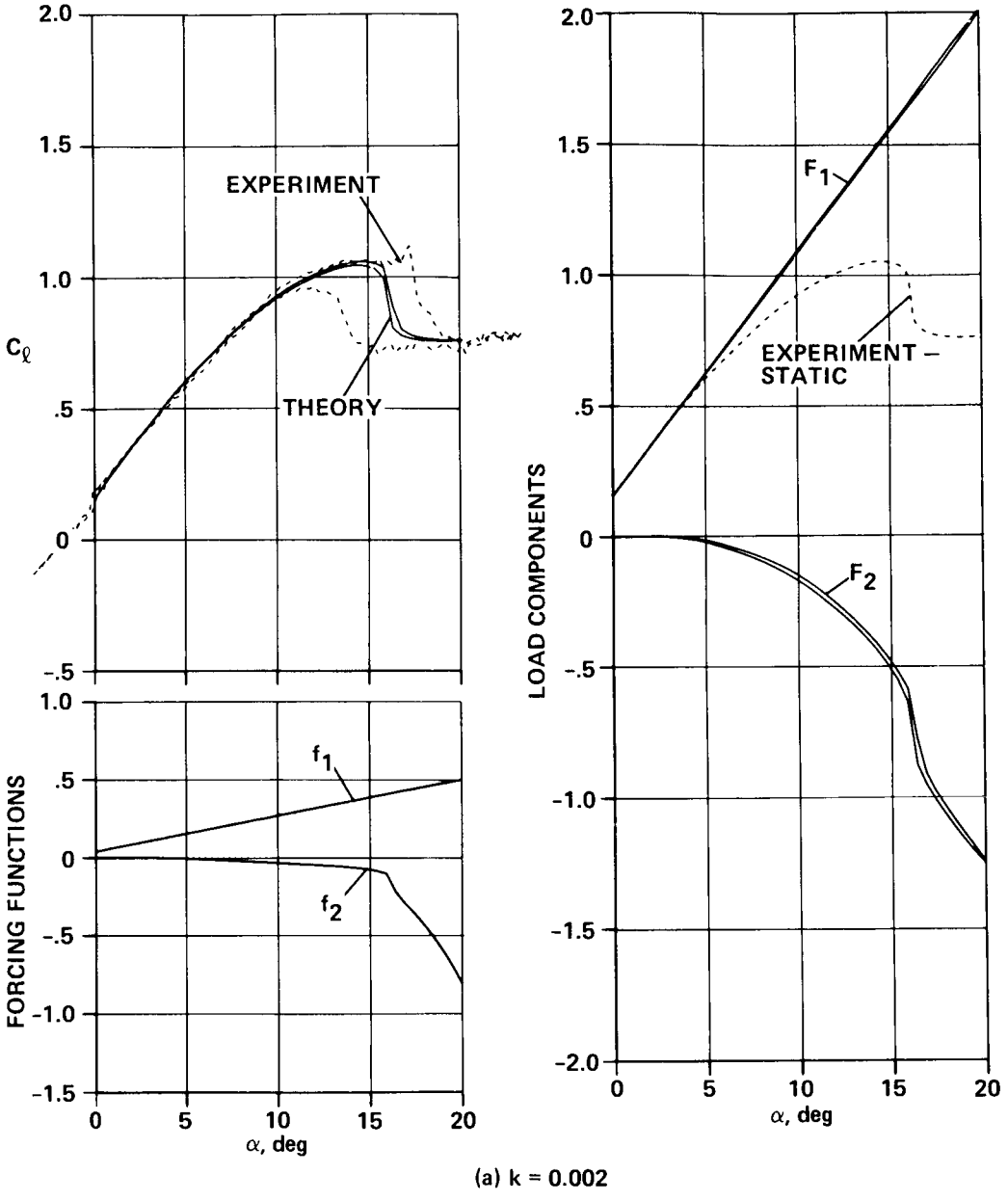

(a) k = 0.002

Figure 27.– Comparison between measured and calculated lift coefficient.

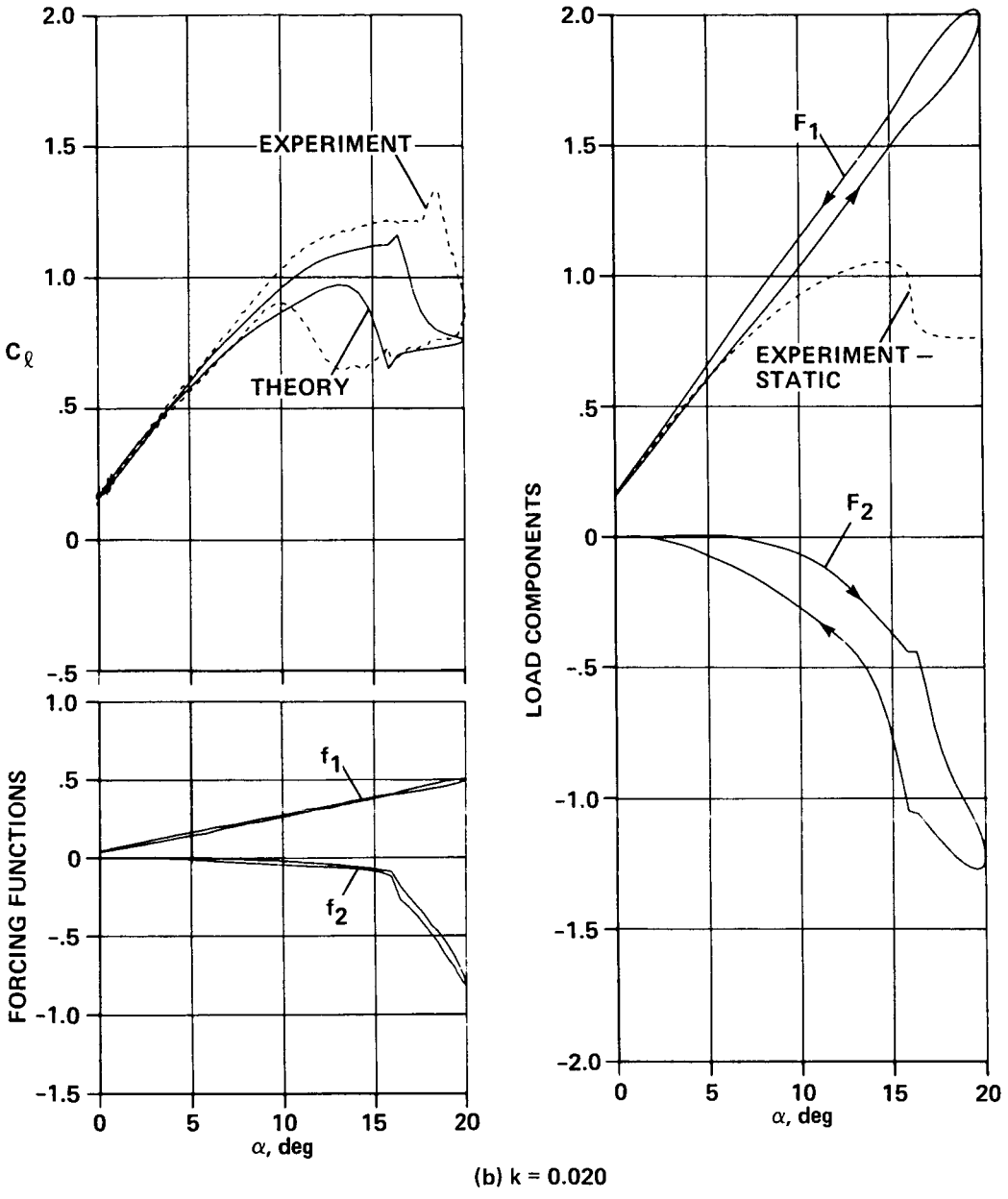

(b) k = 0.020

Figure 27.– Continued.

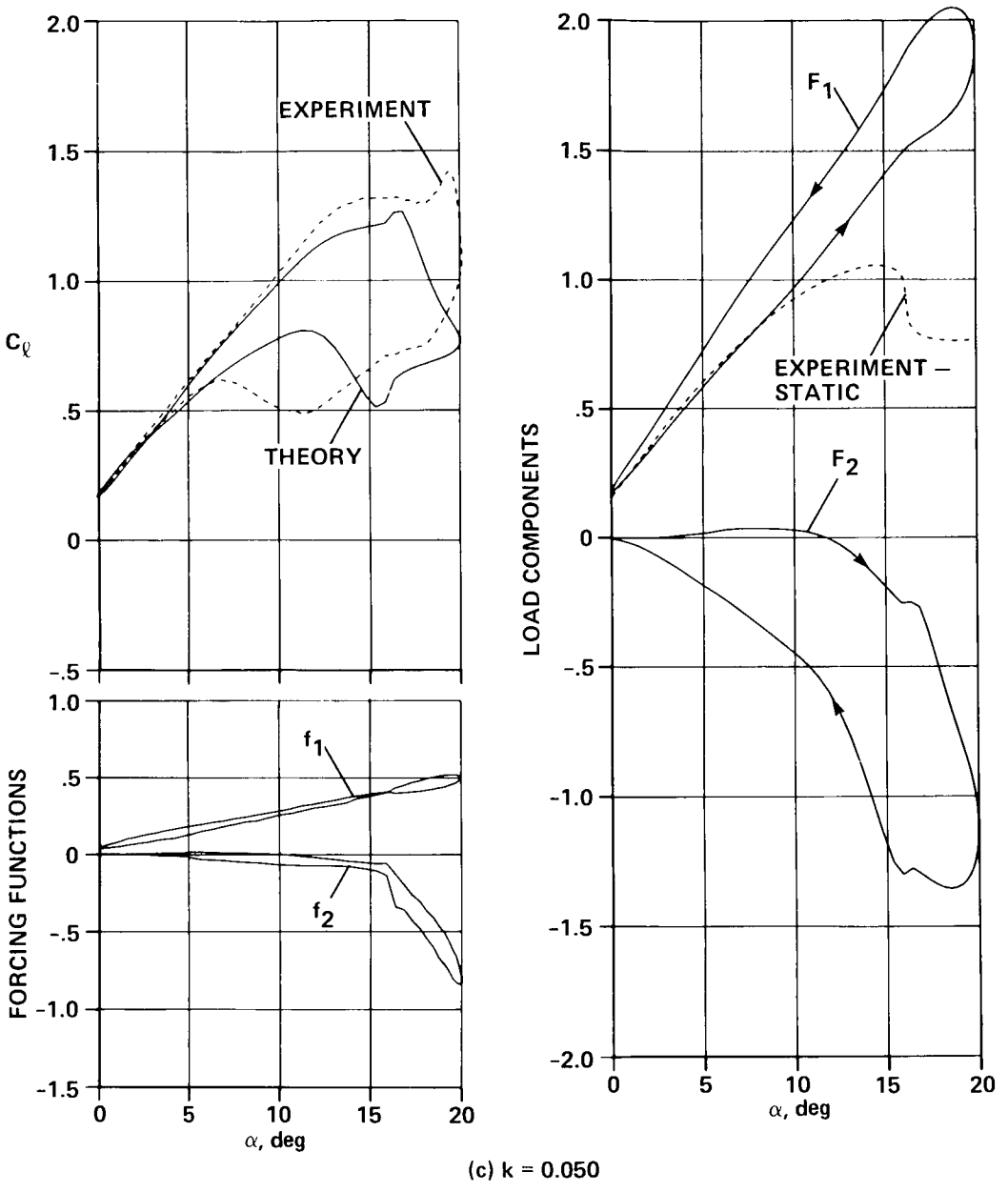

(c) k = 0.050

Figure 27.– Continued.

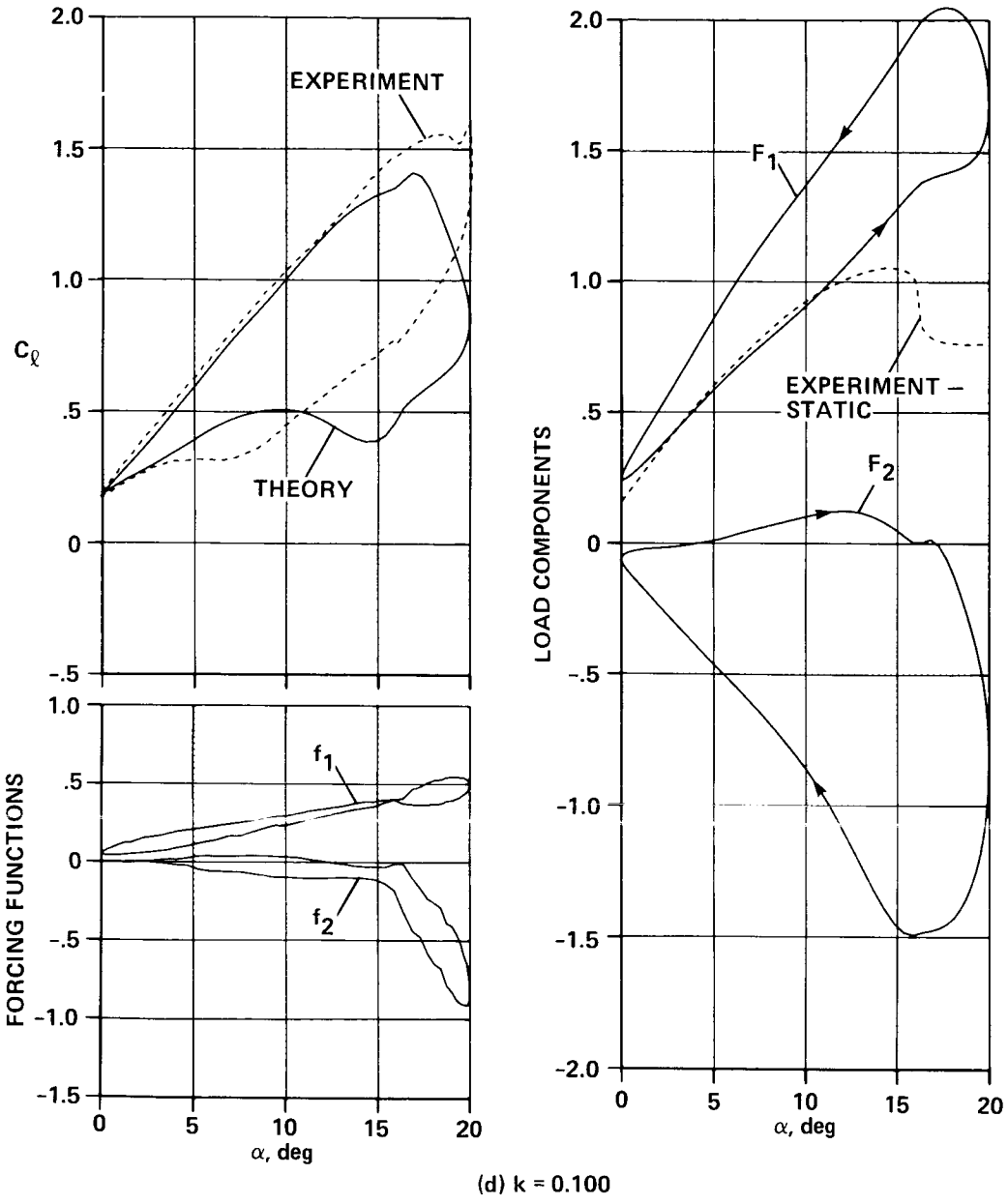

(d) k = 0.100

Figure 27.– Continued.

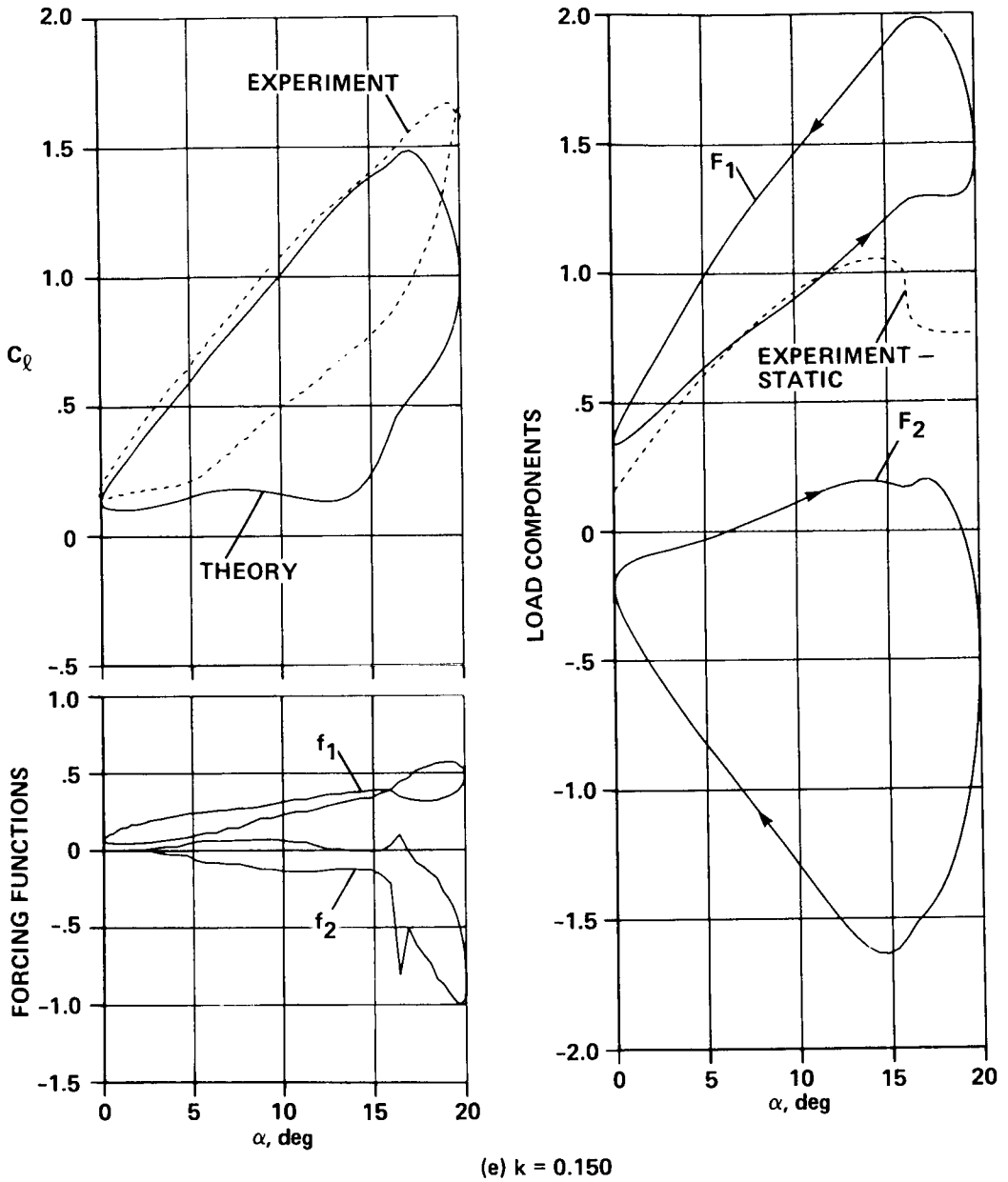

(e) k = 0.150

Figure 27.– Continued.

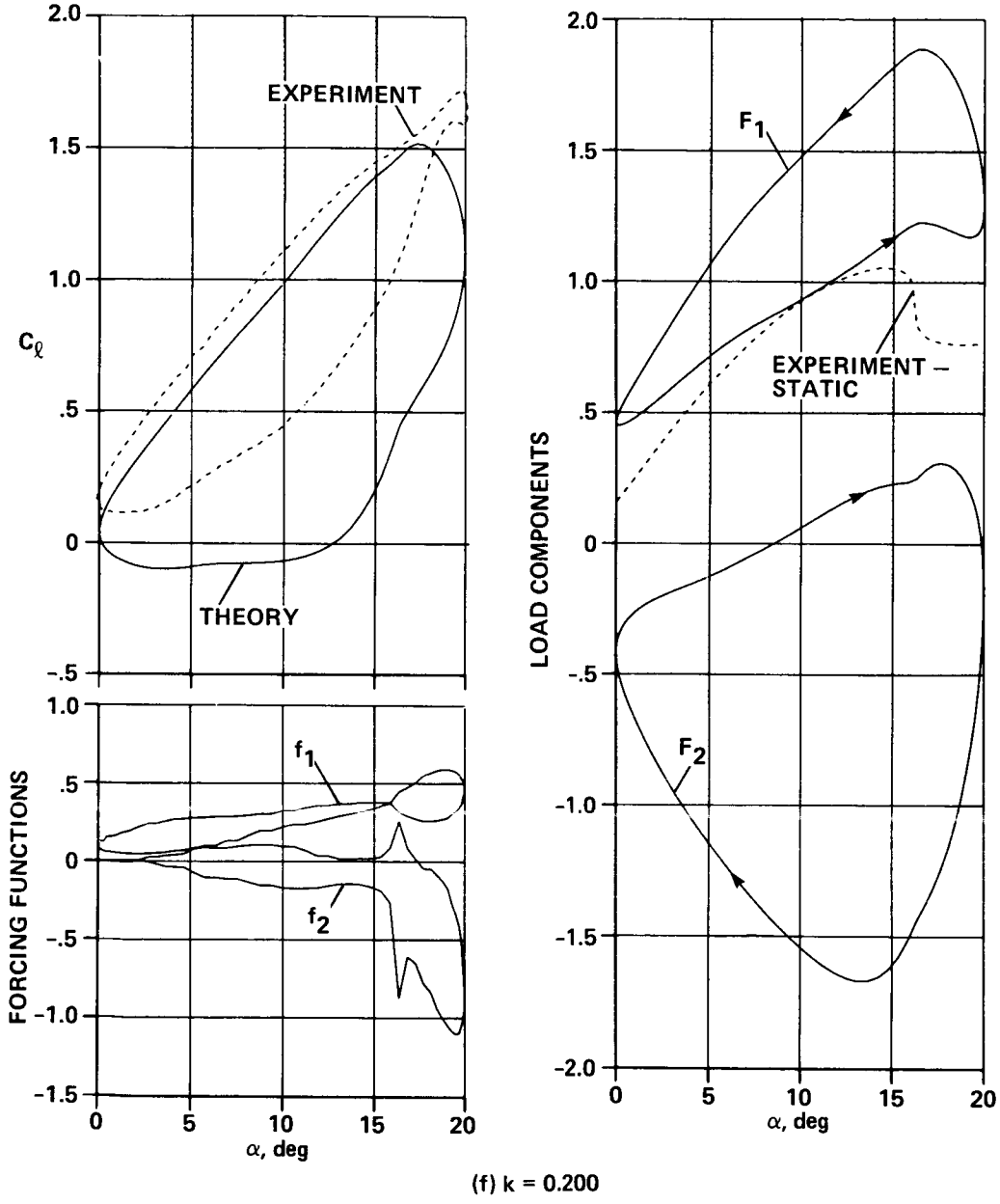

(f) k = 0.200

Figure 27.– Continued.

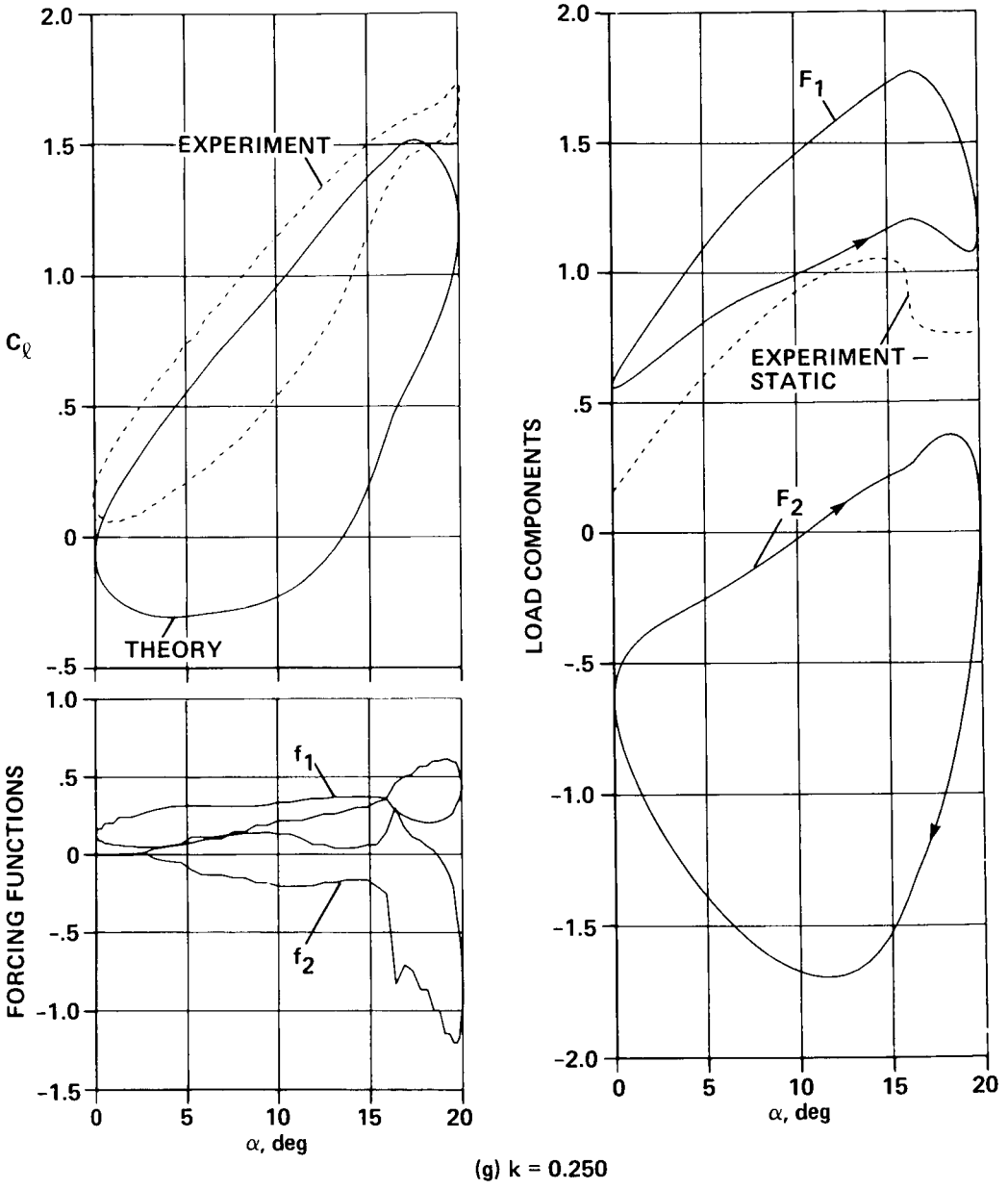

(g) k = 0.250

Figure 27.– Concluded.

1. Report No. NASA TP-2399 AVSCOM TR 84-A-3	2. Government Accession No.	3. Recipient's Catalog No.
4. Title and Subtitle APPLICATION OF THE ONERA MODEL OF DYNAMIC STALL		5. Report Date November 1984 6. Performing Organization Code
7. Author(s) K. W. McAlister, O. Lambert, and D. Petot		8. Performing Organization Report No. A-9824 10. Work Unit No. K-1585
9. Performing Organization Name and Address Aeromechanics Laboratory, U.S. Army Research and Technology Laboratories, AVSCOM, Ames Research Center, Moffett Field, CA 94035		11. Contract or Grant No. 13. Type of Report and Period Covered Technical Report
12. Sponsoring Agency Name and Address National Aeronautics and Space Administration, Washington, DC 20546, and U.S. Army Aviation Systems Command, St. Louis MO 63120		14. Sponsoring Agency Code 992-21-01-90-01

15. Supplementary Notes

K. W. McAlister: Aeromechanics Laboratory, USAAVSCOM Research and Technology Laboratories, Ames Research Center, Moffett Field, California.
O. Lambert: Ingenieur de l'Armement, Service Technique des Programmes Aeronautiques, Paris Armees, France.
D. Petot: Resistance des Structures, Office National D'Etudes et de Recherches Aerospatiales, Châtillon, France.
Point of Contact: Ken McAlister, Ames Research Center, MS 215-1, Moffett Field, CA 94035, (415)965-5892 or FTS 448-5892.

16. Abstract

A semiempirical model, developed at the Office National D'Etudes et de Recherches Aerospatiales (ONERA), to predict the unsteady loads on an airfoil that is experiencing dynamic stall, is investigated. This study describes the math model from an engineering point of view, demonstrates the procedure for obtaining various empirical parameters, and compares the loads predicted by the model with those obtained in the experiment. The procedure is found to be straightforward, and the final calculations are observed to be in qualitative agreement with the experimental results. Comparisons between calculations and measurements also indicate that a decrease in accuracy results when the values of both the reduced frequency and the amplitude of oscillation are large. Potential quantitative improvements in the accuracy of the calculations are discussed in terms of accounting for both the hysteresis in the static data and the effects of stall delay in the governing equations.

17. Key Words (Suggested by Author(s))	18. Distribution Statement		
VR-7 airfoil Airfoil stall Dynamic stall	Unclassified - unlimited Subject Category – 02		
19. Security Classif. (of this report) Unclassified	20. Security Classif. (of this page) Unclassified	21. No. of Pages 65	22. Price* A04

*For sale by the National Technical Information Service, Springfield, Virginia 22161

NASA-Langley, 1984